

Impact of τ decay vertices on the kinematic reconstruction of τ leptons and the determination of the higgs boson mass in $H \rightarrow \tau\tau$ decays in ATLAS

Kevin Bass

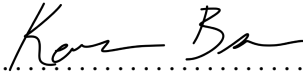
Masterarbeit in Physik
angefertigt im Physikalischen Institut

vorgelegt der
Mathematisch-Naturwissenschaftlichen Fakultät
der
Rheinischen Friedrich-Wilhelms-Universität
Bonn

JAN 2021

I hereby declare that this thesis was formulated by myself and that no sources or tools other than those cited were used.

Bonn, January 8, 2021
.....
Date


.....
Signature

1. Gutachter: Prof. Dr. Klaus Desch
2. Gutachter: Prof. Dr. Ian Brock

Acknowledgements

This thesis could not have been completed without the support and guidance from several people. I would like to extend thanks to Prof. Klaus Desch for the opportunity to write this thesis in his group. I would like to thank Peter Wagner for his guidance at the start of these studies. I would also like to thank Philip Bechtle and Michael Hübner for their insights, discussions, and support during the entire timeline of this thesis. Especially for technical support I would like to thank Christian Grefe and Michael Hübner. I would also like to extend thanks to the many other scientists and students in the group with whom I was able to share ideas and gain greater understanding in the field of Physics. Finally, I would like to thank the friends, family and especially Simon who encouraged and supported me during my education.

Contents

1	Introduction	1
2	Standard Model	3
2.1	Particles and Forces	3
2.1.1	Quantum Electrodynamics	4
2.1.2	The Electroweak force	6
2.1.3	Quantum Chromo Dynamics QCD	7
2.2	The Higgs Boson	9
2.2.1	The Higgs Mechanism	9
2.2.2	Production	11
2.2.3	$H \rightarrow \tau\tau$ decays	11
2.3	The τ Lepton	13
2.3.1	Hadronic τ Decays	13
2.4	New Physics	14
2.4.1	Baryon and Lepton Number Violations	14
2.4.2	CP Violation	15
3	Probing the Standard Model	17
3.1	The Large Hadron Collider	17
3.2	ATLAS	19
3.2.1	Coordinate System	19
3.2.2	Tracking System	20
3.2.3	Calorimeter System	21
3.2.4	Muon System	22
3.2.5	Trigger System	22
3.3	Event Reconstruction	23
3.3.1	Electrons and Photons	23
3.3.2	Muons	24
3.3.3	Jets	24
3.3.4	Taus	25
3.3.5	Vertex and Track Association	27
3.3.6	Missing Transverse Energy E_T^{miss}	29
3.4	Data and Simulations	29

4	Higgs Boson Mass from τ Decay	31
4.1	Monte-Carlo Methods	31
4.1.1	Markov Chain Monte-Carlo (MCMC)	31
4.1.2	Metropolis Hastings (MH) Algorithm	32
4.2	Missing Mass Calculator (MMC)	33
4.2.1	$\tau\tau$ Event Kinematics Reconstruction	33
4.2.2	Weighting Reconstruction Solutions	34
5	Introduction of Vertex Information	37
5.1	Vertex Reconstruction	37
5.1.1	Primary Vertex	37
5.1.2	Secondary Vertex	39
5.2	Kinematics of the $\tau \rightarrow \nu_\tau 3\pi^\pm$ Decay	40
5.2.1	Kinematics from Vertex Information	40
5.2.2	Propagation of Errors	42
5.2.3	Ambiguity in the P_τ Solution	46
5.2.4	Event-by-Event PDFs	46
5.3	Solving the NAN Value Problem	48
5.3.1	Random Walk	49
5.3.2	Metropolis Hastings Algorithm	49
5.3.3	Uncorrelated χ^2 Driven MH	50
5.3.4	Seeding the MH	51
5.4	Future Possibilities	52
6	Optimization and Parametrisation of τ Solutions	55
6.1	Event by Event PDF Generation	55
6.1.1	Choice of Distribution Variables	56
6.2	Solving the Kinematic Ambiguity	59
6.3	Further Parametrisation of Solutions	62
6.4	Final Results	67
7	Conclusion	71
	Bibliography	73
A	Useful Information	81
A.1	Notation	81
A.2	Vertex based \mathbf{P}_τ solution	81
A.3	MH scan for optimization before solution parametrisation	82
A.4	Tables for solution parametrisation for each choice of MH variables	86
A.5	MH scan for optimization after solution parametrisation	86
	List of Figures	99
	List of Tables	101

Introduction

The discovery of the Higgs boson at the Large Hadron Collider by ATLAS and CMS experiments gave support to theoretical predictions of the Standard Model. The Standard Model Higgs boson and the associated Higgs field was theorised as a source of mass for other particles. It was the last Standard Model particle to be found and work continues to both verify its discovery and probe its characteristics. The found Higgs particle could have non-SM qualities, and a precise experimental verification of these qualities is important for the advancement of understanding the fundamental structure of particle physics. [1] [2]

The $H \rightarrow \tau\tau$ decay is of special importance when probing the properties of the Higgs. This decay can provide information on the Yukawa coupling which is predicted by the Standard Model [3], the CP properties of the Higgs [4], and is representative of sizeable and detectable portion from the complete Higgs decays. [5] It is therefore important to increase the efficiency with which these decays are reconstructed. This thesis discusses an avenue for possible further improvements to the reconstruction of mass from ditau events (where the final products are two τ s). These τ leptons are reconstructed from the visible tracks and calorimeter energy deposits which their decay products leave in the detector.

A promising ditau reconstruction method, the Missing Mass Calculator (MMC), is used as the backdrop of this study, and attempts at improving the accuracy of reconstruction are documented herein. The MMC's task of reconstruction is made difficult from the presence of rarely-interacting neutrinos which carry part of the momentum of the decay. Therefore, the MMC makes use of a Markov Chain Monte-Carlo method for improving the τ four momentum \mathbf{P}_τ and the associated neutrino 4 momentum \mathbf{P}_ν . When the kinematics from the full τ momentum \mathbf{P}_τ are improved, a more accurate mass can be determined of the particle from which they decayed. [6] [7] This will allow for both the precision of the Higgs mass to improve, and to separate the Higgs decays from other sources of ditau events.

Currently the MMC takes information from the reconstruction process present in ATLAS. There is, however, more information provided in this reconstruction than is currently being implemented within the MMC's algorithm. Namely, the vertex positions of the primary and secondary vertices of the τ decays are not explicitly used. This information can add an extra constraint on the total momentum with the flight distance and direction information. The content of this thesis details the viability of adding this information and its effect on the event kinematics reconstruction.

The thesis is structured as follows; first, a theoretical background is introduced in Chapter 2. Then, an overview of the LHC and ATLAS Detector is given. (Chaper 3) Both the physical structures and

the methods for interpreting the detection signals to reconstruct events are discussed. This is followed by a short introduction to the Missing Mass Calculator (Chapter 4) and an overview of the statistical processes contained within. The algorithms discussed there will be implemented in multiple areas of this thesis. Chapter 5 explains the process for deriving new kinematic solutions for \mathbf{P}_{τ} from decay vertices of the τ . This chapter details the algorithms, arising difficulties, and initial results of including the vertex information for ditau mass reconstruction. The following Chapter 6 discusses the methods for solving the ambiguity which arises in Chapter 5. The process can be applied to the ambiguities present in \mathbf{P}_{τ} reconstruction outside of the specific vertex-based case used in this thesis. Parametrising steps are given along with event-by-event PDF generation used to weight solutions in the MMC. This information is concluded in Chapter 7.

The studies performed in this thesis used exclusively Monte Carlo simulated data. The notation used mainly in Chapters 5 and 6 is found in Appendix A.1. Unless otherwise specified, all quantities are defined with natural units (i.e. $c = 1$).

Standard Model

The Standard Model is the theory describing the electromagnetic, strong and weak forces. It is largely accepted because of the accuracy with which it has predicted and described several physical processes which are currently probable. However, there are still several areas of physics left to explore and questions which are not answerable with the current Standard Model. In this chapter the Standard Model will be introduced in Section 2.1 along with two specific particles described in it, the Higgs Boson in Section 2.2 and the τ lepton in Section 2.3. At the end in Section 2.4, some of the questions left unanswered by the Standard Model are introduced. Much of the information in this chapter is taken from References [8] and [9].

2.1 Particles and Forces

The Standard Model consists of 17 elementary particles: 12 fermions, 4 force mediating gauge bosons, and the Higgs Boson. The 12 elementary particles called fermions have half integer spin $S = \frac{1}{2}$. These fermions constitute all matter which we interact with. The four gauge bosons have integer spins $S = 1$ and mediate all forces described by the Standard Model (strong, weak, and electromagnetic). The fermions may be split further into two categories. The Leptons which contain 3 particles of negative electric charge and their respective neutrinos with no charge. Neutrinos are affected only by the weak force which is mediated by the Z and W bosons and gravitational force (which is not described by the Standard Model). The 3 charged leptons - the tau τ , the muon μ , and the electron e - are affected by the weak force and the electromagnetic force which is mediated by another gauge boson: the photon. Finally, the quarks are affected by all three forces described in the Standard Model, including the strong force mediated by the gluon. The last particle, the Higgs Boson with spin $S = 0$, will be discussed in further detail later in this chapter. An overview of these particles can be seen in Figure 2.1.

The Leptons are divided into 3 generations which correspond to the energy range in question. The first generation, including the electron, electron neutrino, up and down quark make up the low energy universe. In fact, the atoms of the periodic table contain protons, neutrons, and electrons. Both protons and neutrons are composed of up and down quarks, so in terms of elementary particles, all the atoms in the periodic table are composed of the first generation of fermions. The second and third generations differ only in masses. One can think of the muon as a heavy electron and a tau as an even heavier electron. These higher generations can only be studied at high energies provided in experimental apparatuses like colliders. Each fermion has its own unique quantum number called

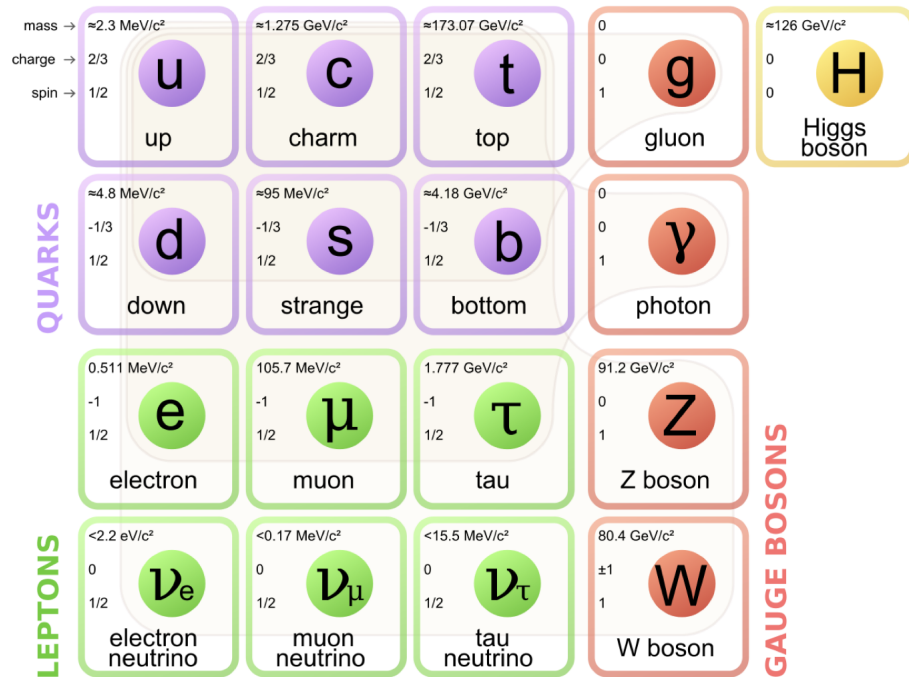


Figure 2.1: Graphical representation of the Standard Model. Taken from [10]

flavor that can be determined from a combination of several other quantum numbers and are conserved in two of the three interactions. For every particle, there exists an anti-particle, alike in mass, opposite in physical charges, i.e. electrical charge, color charge, and weak isospin, among others. For particles whose physical charges are all 0, the possibility of acting as their own anti-particle exists (i.e. the photon). The interaction of a particle with its anti-particle leads to annihilation and the formation of photons or gluons. This is a consequence of the conservation of quantum numbers which sum to zero in the case of particles and their anti-particles.

2.1.1 Quantum Electrodynamics

The Standard Model can be described through the tensor product of 3 gauge symmetries: [11]

$$SU(3)_C \otimes SU(2)_L \otimes U(1)_Y . \quad (2.1)$$

These represent the gauge symmetry of the field theories which describe electromagnetism, strong force, and weak force. The $SU(3)_C$ describes the strong interactions via 8 gluons g . $SU(2)_L \otimes U(1)$ is a special unification of the weak force interactions via 3 heavy bosons, the W^\pm and the Z^0 , and the electromagnetic interactions via one massless photon γ . These will be covered in reverse order here, starting with the electrodynamic interactions.

Quantum Electrodynamics is the quantum field theory to describe the interaction of electrically charged particles and photons. It connects special relativity to electrodynamics through $U(1)$ gauge

invariance. The characteristic Lagrangian:[11]

$$\mathcal{L}_{QED} = \bar{\Psi}(i\gamma^\mu \partial_\mu - m_e)\Psi + e\bar{\Psi}\gamma^\mu\Psi A_\mu - \frac{1}{4}F_{\mu\nu}F^{\mu\nu} \quad (2.2)$$

consists of three terms to describe all interactions. The first term $\bar{\Psi}(i\gamma^\mu \partial_\mu - m_e)\Psi$ is the Dirac Equation which describes the free propagation of the Dirac spinor Ψ (fermion). The third term $\frac{1}{4}F_{\mu\nu}F^{\mu\nu}$ describes the kinematics of the electromagnetic field A_μ (photon), where $F_{\mu\nu} = \partial_\mu A_\nu - \partial_\nu A_\mu$. Finally, the second term describes the interaction between the two. This formulation depends on the assumption that the electromagnetic field is mediated by a massless particle. In fact, if the photon had mass an extra term $\frac{1}{2}m_\gamma^2 A^\mu A_\mu$ would remain non-zero and break the needed gauge symmetry (the invariance under $U(1)$ transformation). Experimentally, the photon mass must be below 1×10^{-18} eV. [12]

The strength with which the photon couples to charged particles is described by the electromagnetic coupling constant α_{em} . This is in fact not a constant as the name suggests but scales as a function of the squared momentum transfer Q^2 . In these terms the electromagnetic coupling constant can be defined as:

$$\alpha(Q^2) = \frac{\alpha(Q_0^2)}{1 - \frac{\alpha(Q_0^2)}{3\pi} \ln\left(\frac{Q^2}{Q_0^2}\right)} \quad (2.3)$$

where $Q^2 \gg Q_0^2$ and many conventions use $Q_0^2 = 0$ and then $\alpha(0) = 1/137$, the fine structure constant. An illustration of this can be seen in Figure 2.2. [13] The scaling or "running" of the coupling

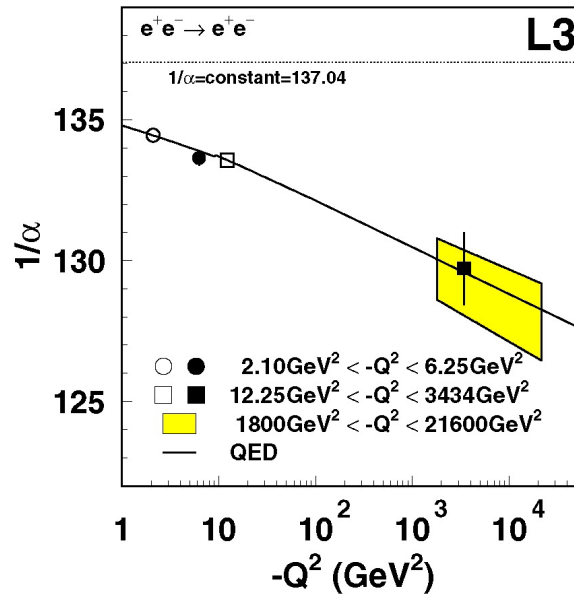


Figure 2.2: The effect of momentum transfer on the strength of the QED coupling factor. The solid line is from QED predictions, the open symbols show values of Q^2 where $\alpha(Q^2)$ was fixed so that the $\alpha(Q^2)$ of the solid lines could be inferred. Taken from [13].

constant with momentum transfer is a result of vacuum polarization, where the photon creates virtual electron-positron pairs which partially block the charge of a particle, often called screening. The closer

two particles are, the greater the momentum transfer, and the less virtual pairs are created. The effect from screening is then much lower. [14] [13] [11] An illustration of this effect is shown in Figure 2.3.

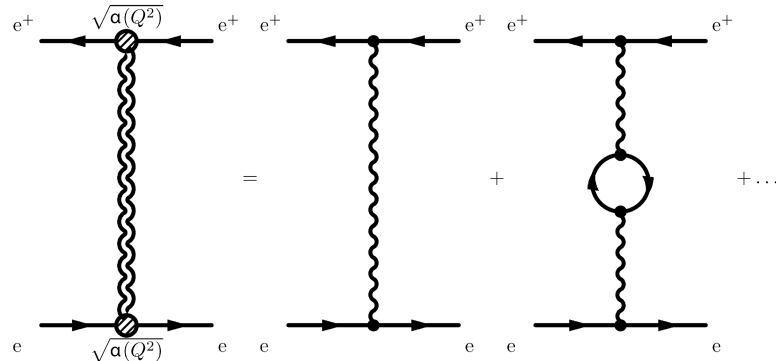


Figure 2.3: A Feynman Diagram showing the contribution of virtual pair creation to the coupling factor. Taken from [13].

2.1.2 The Electroweak force

Every force has an associated charge of interaction. The electromagnetic force described above has electric charge and the weak force which will be the topic of this section has weak isospin. The weak force is unique because every fermion has an associated weak isospin (neutrinos are the only fermions with neutral electric charge). It is also the only force which can change the flavor of a particle. This is an effect that arises from the heavy charged bosons W^\pm which along with the heavy neutral boson Z^0 mediate the weak force. The charged W^\pm is responsible for the flavor changing effects seen in the weak force. Because charge must be conserved, the weak interaction couples to pairs of fermions which differ from each other by 1 electric charge. For Leptons, the weak interaction couples each lepton to its corresponding neutrino. For quarks, every perturbation of pairing a charge $+\frac{2}{3}$ quark (u,c,t), written as q_u , and a charge $-\frac{1}{3}$ quark (d,s,b), written as q_d .

$$\begin{pmatrix} l \\ \nu_l \end{pmatrix} \begin{pmatrix} q_u \\ q_d \end{pmatrix} \tag{2.4}$$

This is specifically important in decays with changing flavors; a prominent example is beta decay which occurs when a neutron decays into a proton, electron and electron neutrino. However, the coupling strength of the weak force is the smallest of the 3 fundamental forces described in the Standard Model, hence the name. This is partly due to the large masses of the gauge bosons mediating the force which decay rapidly. The weak force also has another uniqueness in its weak isospin. This is that chirality plays a role in the determination of the weak isospin number, namely in that left-handed particles (which transform with the left-handed representation of the Poincare group) have weak isospin $I_z = \pm\frac{1}{2}$ and right-handed particles have weak isospin $I_z = 0$. Since a force only affects those particles which contain the characteristic charge, this means that the weak force only couples to left-handed particles (and conversely right-handed anti-particles). Under the gauge symmetry of the weak force $SU(2)$, there are 3 mediating bosons expected, the charged W^\pm bosons mentioned before and a third neutral W^0 boson, to account for scattering processes in which the weak isospin does not change. However there

is no physical W^0 boson. In the 1960s Electroweak Unification Theory from Glashow, Weinberg, and Salam proposed a separate charge for the electroweak force and a mediating boson. These were termed the weak hypercharge Y_w and the B -boson. The electrical charge was then defined as a combination of the weak isospin (representing $SU(2)$) symmetry and the weak hypercharge (representing $U(1)$).

$$Q = I_z + \frac{Y_w}{2} \quad (2.5)$$

This theory showed a mechanism for the mixture of the hypothetical W^0 and B mesons to produce the physical Z^0 and photon γ . This occurs as a consequence of symmetry-breaking required to have mass in the mediating bosons. [8] [9] The symmetry breaking mechanism and the involvement of the Higgs is further discussed in Section 2.2.1 and in more detail in Reference [8].

2.1.3 Quantum Chromo Dynamics QCD

The remaining force in the Standard Model is the strong force, mediated by massless gluons and acting on particles of non-zero color charge. Because of the higher dimensions of $SU(3)$, the gauge theory becomes non-abelian as opposed to the QED $U(1)$. This leads to a term for gluons to interact with other gluons. Therefore the gluons, unlike photons, carry the charge which they also mediate. Some interesting phenomena can be a result of this trait, including the hypothesis of color confinement. This hypothesis postulates that only color neutral objects may exist freely in nature. As in QED, fermionic loops are created as gluons propagate between particles. However, unlike in QED, the interaction of gluons with themselves leads to the added formation of bosonic loops. These latter loops contribute to the scaling coupling factor

$$\alpha_s(Q^2) = \frac{\alpha_s(\mu^2)}{1 + B\alpha_s(\mu^2)\ln(\frac{Q^2}{\mu^2})} \quad (2.6)$$

in such a way that the strength is actually weaker as Q^2 increases creating something like an anti-screening effect. This can be seen in Figure 2.4. In the above equation, $B = \frac{11N_c - 2N_f}{12\pi}$ is dependent on the number of quark flavors N_f and colors N_c which are available at the given Q^2 . From this one can imagine that two color-charged particles very close together feel very little force between them. As the particles start to drift apart, the force felt by each particle becomes stronger, pulling for the particles to come closer together. When considering the field lines of two electrically charged particles, as two particles drift apart the density of lines decreases. However, the attractive force that one gluon presents to another gluon (absent in the case of photons) constrains these to a smaller area (and thus higher density within this area) as particles get farther apart. This creates a tube of linearly increasing pressure, so that infinitely separating two color-charged particles would require an infinite amount of energy. If color-charged particles existed unbound, the force between them would be enormous. Before any color-charged particles would achieve such a distance between them, the energy required to keep them apart would exceed the energy required to create new color-charged particles. This creation would lower the distance between the color-charged objects and therefore less energy would be required to maintain the separation distance. This effectively cuts the tube into smaller strings so that the distance between one color-charged particle and the next closest color-charged particle is kept small. In high energy collisions, high energy quark and anti-quark pairs can be created traveling in opposite directions. Instead of seeing these color charged particles, one sees a string of color

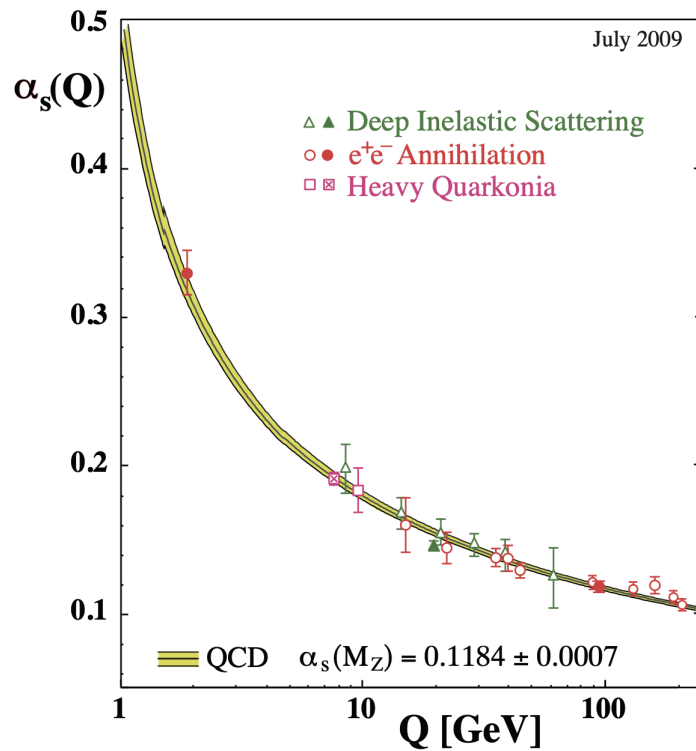


Figure 2.4: The evolution of the QCD coupling factor over time. Taken from [15].

neutral particles created in the same manner as described above (Figure 2.5). This process is called Hadronisation. The number of new quark pairs created in this process scales with the energy of the initially created quark pair. The process continues until all quark pairs have sufficiently low energy that they cannot separate beyond the distance where a new quark pair could be produced. [8] [9]

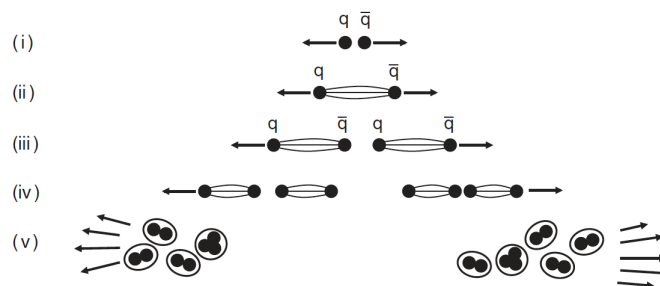


Figure 2.5: An illustration of Hadronisation. Quark pairs at high energy separate until the force between them is high enough for the creation of new quark pairs. This repeats until the energy of each quark pair is low enough that further separation is not possible, leaving a group of hadrons. Taken from [8].

2.2 The Higgs Boson

The Higgs Boson is the SM particle which is credited with mass contributions to massive particles. As mentioned in Section 2.1.3, the masses of the heavy gauge bosons, must be the result of spontaneous symmetry breaking. The Higgs mechanism is the Nobel Prize winning achievement of Peter Higgs and Francois Englert which offers an explanation. [16] The basis of which will be covered in this section and the references [8] [17] contain more detail.

For this thesis, all sample data containing the Higgs are simulated from gluon-gluon-fusion which is discussed briefly in 2.2.2. Section 2.2.3 will focus on the connection between the Higgs and τ leading into Section 2.3.

2.2.1 The Higgs Mechanism

Since the introduction of masses breaks the gauge invariance of the electroweak theory, some method of spontaneous symmetry breaking without explicit breaking must occur. In order to use the Higgs Mechanism with the constraints of the Electroweak Unification, the Higgs Field can be written as one neutral ϕ^0 and one charged ϕ^+ (which should conjugate as $(\phi^+)^* = \phi^-$). [8]

$$\phi = \begin{pmatrix} \phi^+ \\ \phi^- \end{pmatrix} = \frac{1}{\sqrt{2}} \begin{pmatrix} \phi_1 + i\phi_2 \\ \phi_3 + i\phi_4 \end{pmatrix} \quad (2.7)$$

The Lagrangian has the form

$$\mathcal{L} = (D_\mu \phi)^\dagger (D^\mu \phi) - V(\phi) \quad (2.8)$$

where $D^\mu = \partial_\mu + igT_\mu^\alpha + ig'YB_\mu$, with T^α representing the $SU(2)$ generators and $Y = \frac{1}{2}$ is the hypercharge. Here, the Higgs potential

$$V(\phi) = \mu^2 \phi^\dagger \phi - \gamma (\phi^\dagger \phi)^2 \quad (2.9)$$

has a shape defined by the sign of μ^2 while holding $\gamma > 0$. In the case where $\mu^2 > 0$, the minimum is the point where both scalar fields are at 0. In the case where $\mu^2 < 0$ there are an infinite set of degenerate minima defined by

$$\phi^\dagger \phi = \frac{1}{2}(\phi_1^2 + \phi_2^2 + \phi_3^2 + \phi_4^2) = \frac{-\mu^2}{2\gamma} = \frac{-v^2}{2}. \quad (2.10)$$

An illustration of the field in the infinite minima case can be seen in 2.6. The choice of a specific minimum in the infinite case, leads to the spontaneous symmetry breaking. In order for the photon to remain massless after symmetry breaking, there must be an associated non-zero vacuum expectation value with the minimum of the potential. However, this is required for only the neutral scalar field ϕ^0 (the minimum of the charged scalar field ϕ^+ is then 0). [8]

Now in the Unitary Representation of both $SU(2)$ and $U(1)$, the generators for spin $\frac{1}{2}$ are in the form of Pauli Matrices $T^\alpha = \frac{1}{2}\sigma^\alpha$. These correspond respectively to the 3 components of weak isospin and the hypercharge. [19] It can be seen that all generators $T^\alpha \begin{pmatrix} 0 \\ \frac{v}{2\sqrt{2}} \end{pmatrix}$ are non-zero and therefore broken. However, a linear combination of the third component of weak isospin and the hypercharge (see

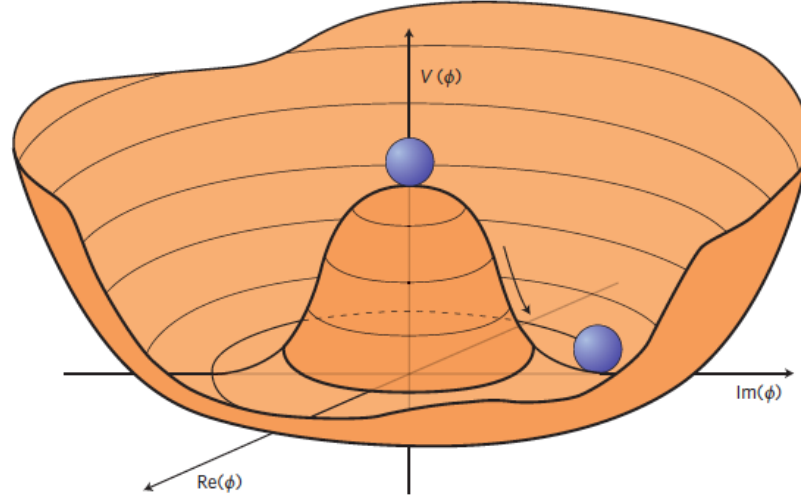


Figure 2.6: A potential with the form of Equation 2.9 with $\mu^2 < 0$. It can be seen that there is a circle of infinite minima around the bottom of the distribution. Taken from [18]

Equation 2.5) is unbroken. This unbroken $U(1)$ symmetry is the electric charge. The remaining 3 broken generators correspond to 3 Goldstone Bosons. For these, the mass can be determined by first expanding the Higgs Field around the chosen minimum and applying some gauge transformations to obtain [20]

$$\phi(\chi) = \frac{1}{\sqrt{2}} \begin{pmatrix} 0 \\ v + h(\chi) \end{pmatrix}. \quad (2.11)$$

Substituting into Equation 2.8,

$$\mathcal{L} = \frac{1}{2} \partial_\mu h \partial^\mu h + \frac{1}{8} [(-gA_\mu^3 + g'B_\mu)^2 + g^2(A_\mu^1 A^{1\mu} + A_\mu^2 A^{2\mu})](h + v)^2 \quad (2.12)$$

it can be seen that the terms A^1 and A^2 have acquired mass. This comes out to be

$$M_W = M_{A^1} = M_{A^2} = \frac{1}{2} g v \quad (2.13)$$

with further calculation the term $(-gA_\mu^3 + g'B_\mu)^2$ can be parsed to determine the masses

$$M_\gamma = 0, \quad M_Z = \frac{1}{2} v \sqrt{g^2 + g'^2}. \quad (2.14)$$

After radiative corrections from renormalization, the physical masses are theoretically determined as $M_W = 79.8 \pm 0.8$ GeV and $M_Z = 90.8 \pm 0.6$ GeV. [20] (with the vacuum expectation value for the Higgs $v = 246$ GeV [8]) These correspond with the experimental values $M_W = 80.379 \pm 0.012$ GeV and $M_Z = 91.1876 \pm 0.0021$ GeV. [12]

The only free parameter left is γ from Equation 2.10 and can be determined by measurements on the Higgs Boson mass. Fermions also acquire mass through coupling with the Higgs field. This

coupling is called the Yukawa coupling and is always proportional to the mass of the fermion.

$$g_f = \sqrt{2} \frac{m_f}{v} \quad (2.15)$$

2.2.2 Production

The proton-proton collisions at the LHC are not with the proton in its entirety. The proton itself is not pointlike, but instead is made up of several partons. Each parton carries a fraction of the momentum. The interaction of a parton from each proton starts the hadronisation process. This makes the production cross sections more difficult to determine, since the momentum of each parton is not exactly known. Instead, parton distribution functions like the one in Figure 2.7, give probabilities of the momentum fractions each parton may hold. From this figure, it can be seen that the gluon has a

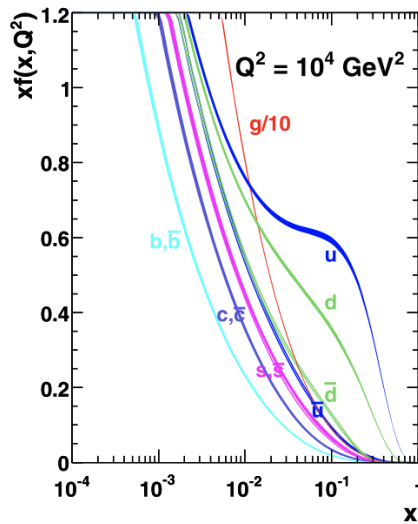


Figure 2.7: Parton distribution functions at $Q^2 = 1 \times 10^4 \text{ GeV}^2$. Taken from [21]

very steep rise as the momentum fraction decreases. Therefore the gluon often has the higher energy and as a result of this the highest Higgs production channel is through the gluon-gluon-fusion (Figure 2.8). It is of further interest to point out that the Higgs Boson couples with massive particles and not directly to the massless gluons. Therefore, it is produced only through loops of massive particles in gluon-gluon-fusion.

2.2.3 $H \rightarrow \tau\tau$ decays

The Higgs Boson gives mass to those particles which couple directly to it. In order to understand fully the mass generation of both fermions and bosons, it is important to establish their coupling to the Higgs Boson. Measuring the coupling of the τ fermion to the Higgs, gives further evidence to the Higgs contribution to fermion mass. In Figure 2.9 the branching ratios of the Higgs Boson for the mass $m_H = 126 \text{ GeV}$ corresponding to the mass of the discovered Higgs Boson. The ditau decay is the second most prominent fermionic decay from the Higgs Boson as expected since the coupling should scale with mass. Because the mass of the top quark is much larger than that of the observed

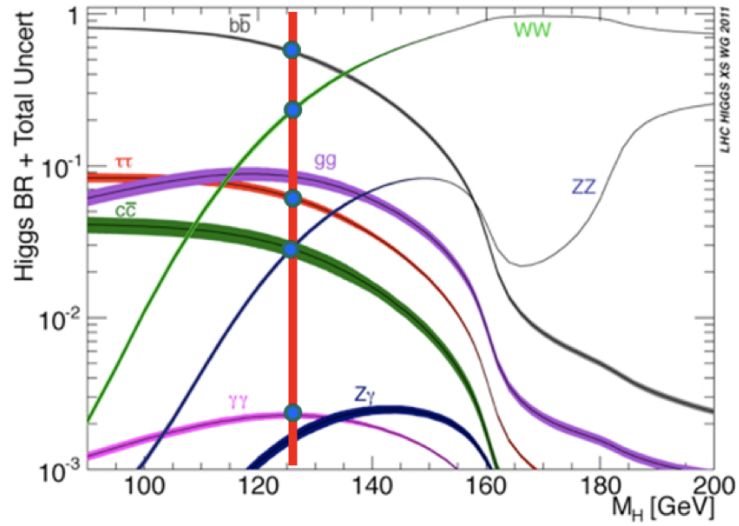


Figure 2.8: Production channels of the Higgs boson at the LHC. Taken from [18]

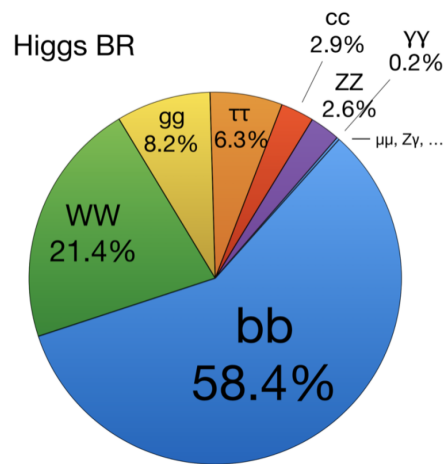


Figure 2.9: Branching Ratios of the Higgs Boson at mass 126 GeV. Taken from [22]

Higgs Boson, it is heavily suppressed. The properties of the τ jet discussed in the next chapter, allow for a better separation from other jet backgrounds as opposed to the b jets. The $H \rightarrow \tau\tau$ decay is therefore a priority for in-depth analysis in ATLAS. It will allow for a more accurate measurement of the coupling of the Higgs to fermions. Moreover, it contains possible measurements of CP violation. [23] [24]

2.3 The τ Lepton

The τ lepton is the main focus of this thesis. Identification and accurate measurements of the τ lepton is important for several interactions which can be studied as probes of the Standard Model and further. This includes exotic particle decays, SUSY [25], and specifically discussed in this thesis, the $H \rightarrow \tau\tau$ decay. As the heaviest lepton at 1776.82 ± 0.16 MeV, the τ lepton has several channels available for decay. It can decay into all lighter leptons as one would expect, but it also can decay into light mesons. This sets it apart from the leptons and introduces a new avenue of detection and identification which is unavailable with the other leptons. The lifetime of the τ , $\tau_\tau = 290 \times 10^{-15}$ s, is short enough that most τ s are not directly measured by the calorimeters in the ATLAS experiment (see Chapter 3 for more information on particle detection and the ATLAS detector). However with the high energy boost from the proton-proton collision, the τ lives long enough for the production and decay to generally be well separated. [26] This means that identification of a τ is based on the decay products which interact with the detectors. In the case of a leptonically decaying tau, the muon or electron produced is used as a means of identifying the tau. Since neutrinos are not detected, it is not possible to determine whether a lighter lepton originates from a tau decay. In the case of hadronically decaying taus however, τ jets are created as the light mesons from the decay traverse the calorimeters. This type of jet energy deposition is similar to that of several other process including a QCD jet background.

2.3.1 Hadronic τ Decays

This thesis is concerned with the hadronically decaying taus, τ_{had} . The main avenues of tau decay are shown in table 2.10. Excluding decays into kaons, the hadronic decays can be categorized by the number of charged and neutral pions. The convention $ApXn$ will be used where A gives the number of charged pions p and X gives the number of neutral pions n . For instance, the decay $\tau \rightarrow \pi^0 \pi^\pm$ is represented as $1p1n$. For the decay into a single pion, the tau decays directly via the W boson. [28] For decays into two and three pions, the usual decay is through the W boson which then decays to intermediate resonances ρ and α_1 and finally these decay into π s.

The main parts of tau reconstruction will be discussed in Section 3.3.4; the concepts are briefly addressed here. Charged pions are reconstructed by the tracks they form in the tracking system of ATLAS. Neutral pions can be reconstructed from the energy deposits in the calorimeter. The tau neutrino is not explicitly constructed, and instead is found within the Missing Transverse Energy (MET) (also further discussed in Section 3.3.6). All of these pieces are needed to reconstruct the kinematics of the tau decay (discussed in Section 5.2). The key characteristics which separate this event from other jet producing events are the highly collimated tracks at high momentum and the number of charged tracks (1, 3, or rarely 5). When compared to QCD jets, for example, the multiplicity of tau decays is lower and the tracks diverge less.

$\tau \rightarrow e\nu_e \nu_\tau,$ $\tau \rightarrow \mu\nu_\mu \nu_\tau$	17.8 % 17.4 %
$\tau \rightarrow \pi^\pm \nu_\tau$	11.1 %
$\tau \rightarrow \pi^0 \pi^\pm \nu_\tau$	25.4 %
$\tau \rightarrow \pi^0 \pi^0 \pi^\pm \nu_\tau$	9.19 %
$\tau \rightarrow \pi^0 \pi^0 \pi^0 \pi^\pm \nu_\tau$	1.08 %
$\tau \rightarrow \pi^\pm \pi^\pm \pi^\pm \nu_\tau$	8.98 %
$\tau \rightarrow \pi^0 \pi^\pm \pi^\pm \pi^\pm \nu_\tau$	4.30 %
$\tau \rightarrow \pi^0 \pi^0 \pi^\pm \pi^\pm \pi^\pm \nu_\tau$	0.50 %
$\tau \rightarrow \pi^0 \pi^0 \pi^0 \pi^\pm \pi^\pm \pi^\pm \nu_\tau$	0.11 %
$\tau \rightarrow K^\pm X \nu_\tau$	3.74 %
$\tau \rightarrow (\pi^0) \pi^\pm \pi^\pm \pi^\pm \pi^\pm \pi^\pm \nu_\tau$	0.10 %
others	0.03 %

Figure 2.10: A chart of the main decays of the tau lepton. Taken from [27]

2.4 New Physics

In the universe there is a large imbalance in matter and anti-matter. It is still unknown exactly where this imbalance comes from, but several theories exist to account for this asymmetry. Several of these theories predict a combination of the strong, electromagnetic and weak forces into a single force. These Grand Unified Theories (GUTs) have avenues for Baryon number, Lepton number, and CP violations which were believed to be conserved quantities. Even before these theories were invented, Andrei Sakharov proposed in 1965 that the matter and anti-matter asymmetry arose from the Baryon number not being conserved. He determined three conditions a theory on particle interactions must satisfy to explain the asymmetry:[29]

- Baryon Number Violation
- C and CP violation
- Deviation from thermal equilibrium

2.4.1 Baryon and Lepton Number Violations

Baryon number is defined by [30]

$$B = \sum_q (N_q B_q + N_{\bar{q}} B_{\bar{q}}) = \sum_q (N_q - N_{\bar{q}}) \cdot \frac{1}{3} \quad (2.16)$$

where q represents quark flavors: $q = u, d, c, s, t, b$. B_q represents the baryon number for quarks $B_q(B_{\bar{q}}) = \frac{1}{3}(-\frac{1}{3})$, and $N_q(N_{\bar{q}})$ is the number of quarks (anti-quarks). The stability of matter is

attributed to the conservation of Baryon number. However when this is viewed as an approximately conserved value with the introduction of tiny violations, the universe becomes stable only on the time scale of the then inevitable decay of the proton ($\tau_p > 10^{31}$ years). This introduction of violation could explain the asymmetry of the universe.[31]

As an alternative to the baryon number violation (or in addition to), lepton number violation can be used to explain the asymmetry. Lepton number is defined by [30]

$$L = \sum_l L(l, \nu_l) = \sum_l (N_l L_l + N_{\nu_l} L_{\nu_l} + N_{\bar{l}} L_{\bar{l}} + N_{\bar{\nu}_l} L_{\bar{\nu}_l}) = \sum_l (N_l + N_{\nu_l} - N_{\bar{l}} - N_{\bar{\nu}_l}) \quad (2.17)$$

where l represents lepton flavors $l = e, \mu, \tau$. L_l and L_{ν_l} are the lepton number $L_l(L_{\bar{l}}) = L_{\nu_l}(L_{\bar{\nu}_l}) = 1(-1)$, and N_l, N_{ν_l} represent the number of leptons and associated neutrinos. The Standard Model has an inherent lepton number conservation which leads to massless neutrinos. The Nobel Prize winning discovery by Takaaki Kajita and Arthur B. McDonald of neutrino oscillations, requiring neutrinos to have mass, gave experimental evidence of the shortcomings of the Standard Model as a complete theory. [32] This also opened up the lepton number conservation rule to more scrutiny. The search for neutrinoless double beta decays and specific proton decays which would support Lepton number violation are underway. [33] [34]

The concept of a conserved quantity determined from a combination of lepton number and baryon number is also emerging in many GUTs. The most common one is the $B - L$ conservation. This would open avenues for the existence of both lepton and baryon number violation. These violations are still being searched for, and the occurrences of these processes are predicted to be very small. [33] [34]

2.4.2 CP Violation

Besides these number violations, CP violation can be used to account for the asymmetry. This is a violation we can observe in the decay of the τ . Charge Conjugation (C) is an operation of changing a particle to its anti-particle.

$$C |p\rangle = |\bar{p}\rangle. \quad (2.18)$$

It arises from the fact that electrodynamics is invariant under a change in sign of all electric charges. C is conserved in both electromagnetic and strong forces. However it is not conserved in the weak force. This is most clearly seen in the interaction with leptons since the charge conjugation operator applied to a normal left-handed neutrino will create a left-handed anti-neutrino which does not exist. Parity (P) is an operation of inversion (creating an upside down and backwards image of the original).

- Scalar: $P |s\rangle = |s\rangle$
- Pseudoscalar: $P |p\rangle = |-p\rangle$
- Vector: $p |v\rangle = |-v\rangle$
- Pseudovector: $p |a\rangle = |a\rangle$

The idea is the inversion of any process follows the same rules as the original process. In electromagnetic and strong interactions, this is once again conserved. In the weak interactions this is strongly violated. This can be seen in several ways, but most notably in the handedness of the neutrinos and anti-neutrinos. These are always left-handed and right-handed respectively. The application of parity to a neutrino

would create a right-handed neutrino, but this is not experimentally seen and therefore cannot be considered conserved, as it is in the electromagnetic force. One reaction to the observed violations in C and P , created the combined CP operators as a conserved quantity. In fact, the combined symmetries are not violated when applied to the above neutrinos. A left-handed neutrino under CP becomes a right-handed anti-neutrino as is observed. Looking at the decays of Kaons K , however, CP violation was observed. Originally the K^0, \bar{K}^0 system was thought to decay according to two eigenstates of CP , K_1 and K_2 which decayed into 2π and 3π respectively and had lifetimes of 0.895×10^{-10} s and 5.11×10^{-8} s respectively.

$$|K_1\rangle = \frac{1}{\sqrt{2}}(|K^0\rangle - |\bar{K}^0\rangle) \quad (2.19)$$

$$|K_0\rangle = \frac{1}{\sqrt{2}}(|K^0\rangle + |\bar{K}^0\rangle) \quad (2.20)$$

It was determined later that the K_2 eigenstate decayed into 2π which meant it was not a pure eigenstate and therefore CP was violated. Further K decays were studied and more evidence of CP violation was found. This was a direct link to the matter and anti-matter asymmetry since there was a clear preference in decays to one over the other. [9] All the observed cases of CP violation do not account for the full amount required by the Sakharov condition. Therefore the search continues for more avenues of this violation, and the Higgs Boson could contain such avenues. The current constraints on the Higgs boson interactions, still allow for large coupling deviations. Further the $H \rightarrow \tau\tau$ decays, especially for τ_{had} s, there is a possibility to measure the CP even/odd states of the Higgs. These are further discussed in [4][35].

Probing the Standard Model

Many of the unanswered questions, and untested aspects of the Standard Model, lie in energy ranges which are not naturally accessible. In order to probe the theory and look for evidence of expansion and new physics, particle accelerators and colliders have been built which seek to create a high energy environment. In the following chapter, an introduction into the largest particle collider will be given (Section 3.1). The detector which is used as the basis of data collection for this thesis is covered (Section 3.2). Finally, the methods used for interpreting that data is discussed (Section 3.3). Within the last section, special emphasis is placed on the Tau Jet Reconstruction. For this, much of the information was taken from Reference [26] and [28].

3.1 The Large Hadron Collider

The Large Hadron Collider (LHC) is explicitly named. It is a circular particle accelerator 27km in circumference (Large) which accelerates protons and heavy ions (Hadron) in opposite directions in order to collide them (Collider) at 4 different points. Its prime motivation upon concept was to probe the nature of the electroweak symmetry breaking discussed in Section 2.1.2. This was believed to be carried out by the Higgs Field. The direct evidence of this along with the accompanying theory led to Peter Higgs and Francois Englert receiving the Nobel Prize in Physics [16]. The LHC is the most powerful accelerator in existence. It resides 100 meters underground on the border between France and Switzerland at The European Organization for Nuclear Research (CERN). [36] The LHC was created to facilitate collisions with a center-of-mass energy up to $\sqrt{s} = 14$ TeV, and deliver a luminosity \mathcal{L} up to $10^{34} \text{ cm}^{-2} \text{ s}^{-1}$ [37].

There are four experiments set up at the LHC. The positions can be seen in Figure 3.1. At point 2, the ALICE experiment is set up. ALICE (A Large Ion Collider Experiment) is a heavy-ion detector focusing on the strong interaction sector of the Standard Model. It seeks to discern information about physics at the energy levels of the early universe. [40] At point 5 stands the Compact Muon Solenoid (CMS) detector. It was designed to study a broad range of high energy phenomenon and namely to study Higgs related processes. [37] The LHCb detector resides at point 8. The primary aim of this detector is to search for CP violation and rare beauty and charm particle decays. [41] The fourth and final detector is the ATLAS detector at point 1. It is the main focus of the next section and like the CMS detector, its main goal was the detection of the Higgs Boson.

The production of physics processes which are of the highest interest are largely dominated over

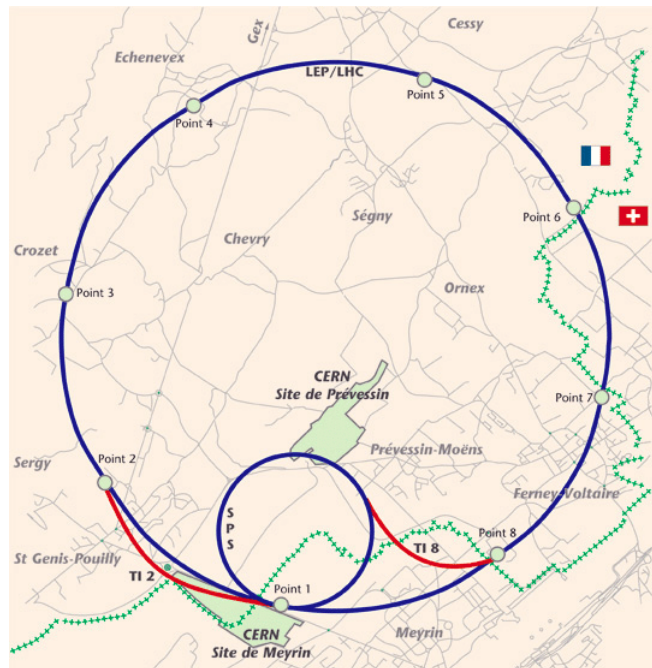


Figure 3.1: The location of the LHC. Taken from [38].

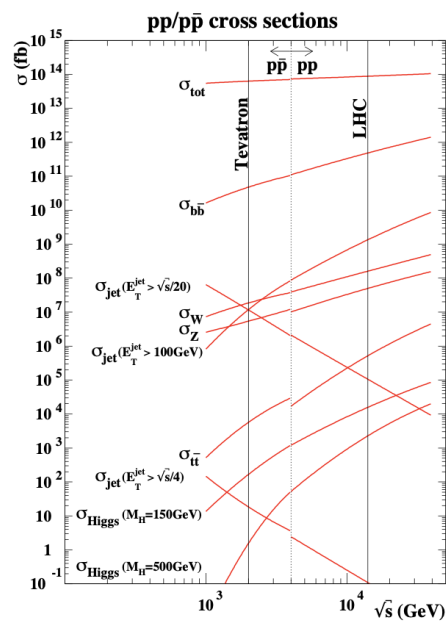


Figure 3.2: Production cross sections at different center-of-mass energies. Taken from [39].

by the cross section of background events. This comes from the fact that these processes either contain massive particles or are characterized by electroweak cross sections. While this problem is not resolved at higher energies, it is lessened specifically for the Higgs production. Figure 3.2 shows the cross sections over a range of center-of-mass energies. It can be seen that the major Z background rises significantly less than the production cross section of H . However, both the QCD Jet production and Z production cross sections are magnitudes higher than the target H . This emphasises the importance of accurate background and event separation techniques. [39]

3.2 ATLAS

After the discovery of the Higgs Boson, there still remain several questions about the exact properties it holds. The ATLAS detector is also set up to provide information in several other areas of high energy physics. The ATLAS detector is continually undergoing design improvements as new technology becomes available. Simultaneously, the methods for analyzing the data of previous runs, and the framework to analyze future runs is constantly being revised. The limits of physical detection resolution and accurate analysis of the signatures left in the detector are being pushed. In the following sections, the various aspects of the ATLAS detector will be discussed. The system as a whole can be seen in Figure 3.3 and more in-depth information can be found in Reference [42], from which much of the information in these sections is taken.

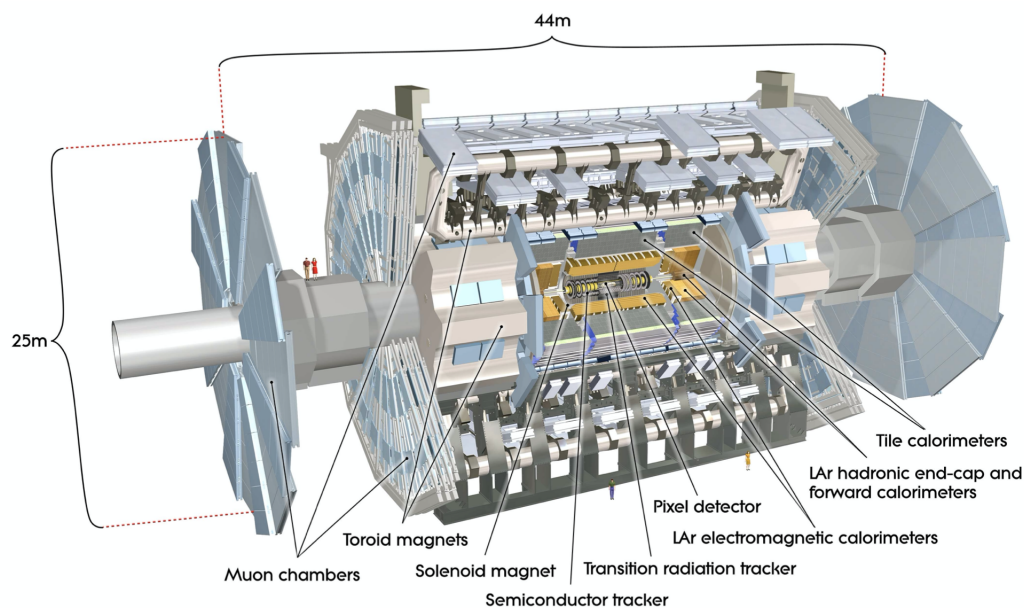


Figure 3.3: Overview of the ATLAS Detector. Taken from [42].

3.2.1 Coordinate System

The coordinate system used to describe the events which take place in a collision is optimized for the experimental setup. The origin is placed at the nominal interaction point in the center of the detector.

The coordinate system is right handed with the z -axis oriented along the beam line and the y -axis pointing upwards. The collision of two protons is really a collision of the partons which are contained in the proton as discussed in Section 2.2.2. To this effect, it is not possible to determine the exact momentum which went into the collision. Additionally, particles resulting from the collision have a boost in the z direction from the mismatched energies of the colliding partons. Therefore rapidity is introduced which relates the frame of the boosted objects to a frame which is perpendicular to the beamline. [8]

$$y = \frac{1}{2} \ln \left(\frac{E + p_z}{E - p_z} \right) \quad (3.1)$$

This is further simplified to pseudorapidity when it is assumed that the mass of the particle is much less than the energy. [8]

$$\eta = -\ln \left(\tan \frac{\theta}{2} \right) \quad (3.2)$$

The pseudorapidity is minimal when perpendicular to the z -axis and maximal when parallel. There are two main advantages to this parameter. First, the differences in η are Lorentz invariant. Second, the number of emerging particles is roughly equal in each $\Delta\eta$ interval. Since the initial energy in the beamline direction is unknown, the transverse momentum is used instead, where one can take advantage of momentum conservation. [8]

$$p_T = \sqrt{p_x^2 + p_y^2} \quad (3.3)$$

Finally, the separation of two particles is measured in terms of ΔR which combines the above pseudorapidity η with the azimuthal angle θ .

$$\Delta R = \sqrt{(\Delta\theta)^2 + (\Delta\eta)^2} \quad (3.4)$$

3.2.2 Tracking System

The tracking system is the first line of detection for particles resulting from the proton-proton collision. There is a high density of such particles, approximately 1000 every 25 ns within $|\eta| < 2.5$. The entire Inner Detector is subject to a 2 T magnetic field which bends the charged tracks, giving a means of momentum calculation based on the curvature. The Inner Detector (ID) pictured in Figure 3.4 must have very fine detector granularity. In fact, the ID was designed to be at the limit of technological ability. The Inner Detector is composed of three independent, complimentary sub-detector systems, the pixel detectors, the silicon microstrip (SCT) detectors, and the Transition Radiation Tracker (TRT) detectors. The pixel detectors reside closest to the beam, along with the SCT detectors. There are three original pixel layers which are each segmented in $R - \phi$ and z and a fourth inner layer which is added in the upgrade of the ATLAS detector for Run 2. [43]

The SCT detector consists of 8 strip layers which should be crossed by each tracks. In the barrel region, these are situated along with the pixel detectors in concentric cylinders around the beam axis. At the end-cap regions, both SCT and pixel detectors are situated on disks perpendicular to the beam. Together the two detector subsystems cover a range of $|\eta| < 1.7$ for two permanent barrel layers, $|\eta| < 2.5$ for one removable barrel layer, and $1.7 < \eta < 2.5$ in the endcaps on each side. [44]

Lastly a gaseous detector, the TRT provides additional $R - \phi$ information at a larger radius than the

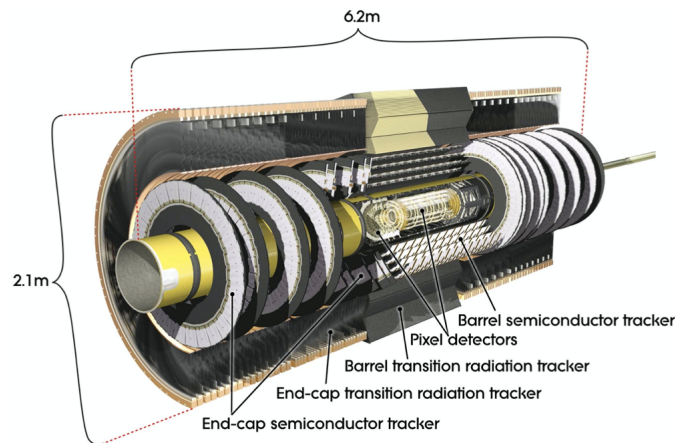


Figure 3.4: View of the Inner Detector. Taken from [42].

previous detectors. The TRT contains a large number of 4 mm straw tubes which record a high number of hits per track. The TRT supports track following up to $|\eta| = 2.0$. It also aids in the identification of electrons as transition-radiation photons are detected within it. Altogether, the three detector parts provide tracking information to match the range covered by the calorimeters. They also aid in vertex reconstruction for heavy particles, and τ -tagging. [42]

3.2.3 Calorimeter System

The Calorimeter system encircles the Inner Detector. The main goal of the calorimeters is to have incoming particles deposit the entirety of their energy. There are two systems of calorimeters, the electromagnetic calorimeter (eCAL) and the hadronic calorimeter (hCAL), the entire setup is shown in Figure 3.5.

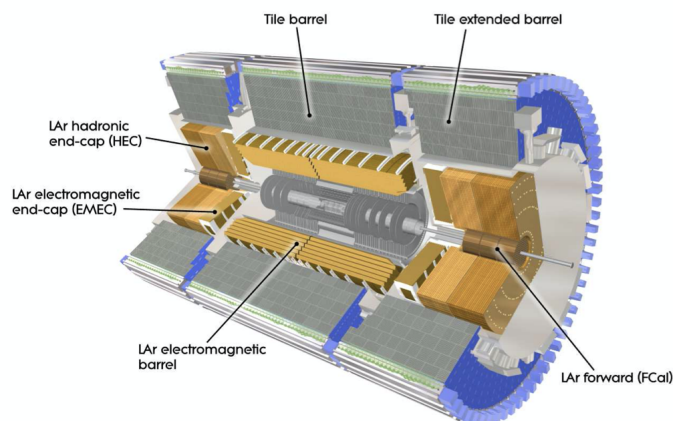


Figure 3.5: View of the Calorimeters. Taken from [42].

Particles which interact via electromagnetism (electrically charged particles and photons), will

interact with the eCAL. The calorimeter is an alternating layer, lead-LAr detector. The lead layer acts as a passive absorber material which interacts with passing charged particles and photons, creating narrow electromagnetic showers. Some neutral particles will also leave signatures here. These are particles, like the neutral π^0 , which can decay to charged particles. The neutral π^0 for example will decay to photons which then also may undergo pair production. The Liquid Argon (LAr) layer is ionized from the showers created in the lead layer, resulting in a signal proportional to the energy of the passing particle. Ideally, this would completely stop all particles which interact mainly through electromagnetic force. To accomplish this, a thickness of more than 22 radiation lengths X_0 is designed for the barrel, and more than 24 X_0 in the endcaps. The radiation length is the thickness of a material required for a passing electron to reduce its energy by a factor of $\frac{1}{e}$. [45] The barrel portion covers a range of $|\eta| < 1.475$ while the endcap covers $1.375 < |\eta| < 3.2$. For the region which is complemented by the Inner Detector, $|\eta| < 2.5$, the eCAL has 3 sections and for the additional range, there are 2 sections.

Particles which are not stopped completely in the eCAL, will then pass through the Hadronic Calorimeter (hCAL). It is similar to the eCAL in its active and passive absorption design. There are three setups for the hCAL. The first, the tile calorimeter, is placed directly outside the EM calorimeter and consists of a barrel and extended barrel component. The passive material is steel and the signal material is scintillating tiles. The total thickness covers 9.7 interaction lengths λ . The interaction length is the mean free path a particle travels before scattering inelastically. [45] The second hCAL component is the LAr end-cap calorimeter. The detector contains layers of copper and LAr and extends through $1.5 < |\eta| < 3.2$. Thus, it overlaps at with the ends of the other two hCAL components. Lastly, the third component is the LAr forward calorimeter. This extends the coverage of the calorimeter to $3.1 < |\eta| < 4.9$. The layers of this detector start with copper and then move to tungsten as the passive absorption material. Again, the LAr acts as the active component. [42] The combined density of the calorimeters, causes the likelihood for a particle to punch-through the system to be significantly low. The exceptions include muons and neutrinos. The latter is not detectable in the ATLAS set-up and the former is detected in the muon detection system.

3.2.4 Muon System

The muon system is the last system of the ATLAS apparatus and can be seen in Figure 3.6. The muons entering the muon detection chambers are deflected by a magnetic field set up so that the field lines are perpendicular to the beam pipe. In the barrel region, there are three layers of chambers in cylinders around the other detectors. The end-cap and transition regions have three layers of planes which are aligned perpendicular to the beam. The curvature of the muon tracks which are detected in these chambers, allow for the measurement of muon momentum. Additionally, the time resolution in this system allows for an effective fast-trigger decision in the trigger system.

3.2.5 Trigger System

The collisions in the LHC have a bunch spacing of 25 ns, a center-of-mass energy of 13 TeV, a peak luminosity of $1 - 2 \times 10^{34} \text{ cm}^{-2} \text{ s}^{-1}$ and a peak number of collisions per bunch at 25-50. [46] For these parameters, it would be impossible to store and analyze every event. Therefore, it is important to focus on the events which are of special interest. This is done through a trigger system which looks for key signatures of interesting events and stores the data only for these events. A detailed overview of

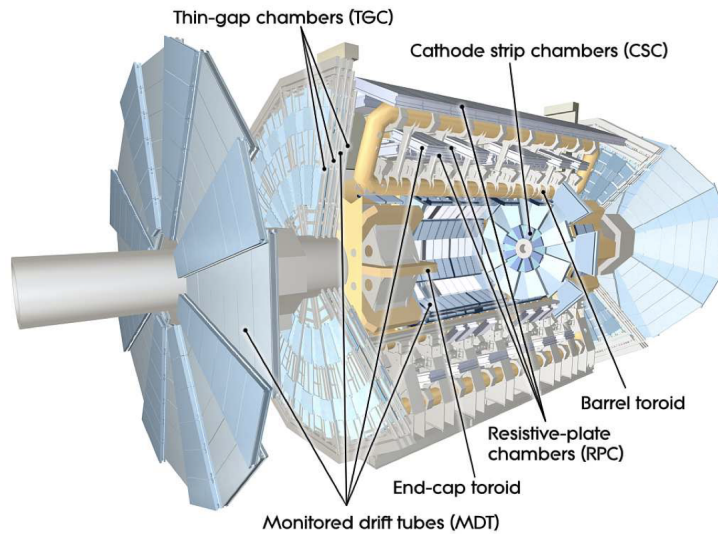


Figure 3.6: View of the Muon Detector system. Taken from [42].

the requirements of the trigger system is found in Reference [47] and the upgraded requirements for the aforementioned parameters can be found in Reference [46]. The event rate for run 2 of the LHC would mean a recording rate of 40 MHz, however with the combination of a hardware level-1 and software-based high-level trigger, the actual storing of information is brought down to 100 kHz and then further to approximately 1 kHz. These triggers work together using criteria such as p_T , E_T^{miss} , angular separation, and invariant mass, among others. The event triggers are specific for tagging and recording, depending on which physical processes are deemed of interest.

3.3 Event Reconstruction

Every particle which interacts with the ATLAS detector leaves a signature. The difficult task is to interpret these signatures and work backwards to determine which particles they originate from. An overview of the processes currently used to identify particles by their signals is given in this section.

3.3.1 Electrons and Photons

Photons are classified into two categories, unconverted photons and converted photons. The latter are photons which have created electron-positron pairs. The photons themselves are expected to leave signatures which contain little to no deposits in the hCAL. They leave rectangular shaped clusters in the eCAL, and pairs of oppositely charged tracks for converted photons, or no tracks for unconverted photons. Three criteria are used to separate prompt photons from other signals, $E_T^{iso} < 0.065 \cdot E_T$, $p_T^{iso} < 0.05 \cdot E_T$, and $\Delta R < 0.2$. E_T^{iso} is the sum of energies in the clusters of the calorimeters minus the photon candidate energy. p_T^{iso} is similarly calculated using tracks which pass specific qualifications instead of cluster energy information. Lastly, a constraint on the η region is imposed to ensure that the entire photon shower is contained within the detector. [48] More detailed information of photon reconstruction can be found in Reference [49].

Electrons have the tendency to lose energy via bremsstrahlung radiation. The radiated photons can also be converted or unconverted, creating electron-positron pairs which also leave energy deposits in the detector. These interactions can occur anywhere along the path of the primary electron, leaving a spread of signals in the respective detection system. The resulting spread is generally very collimated. The tracks and eCAL clusters are examined together, they must fulfill spatial requirements $|\eta_{cluster} - \eta_{track}| < 0.05$ and $-0.1 < \Delta\phi < 0.05$. More information on this process can be found in Reference [50].

3.3.2 Muons

Muon detection is a combination of the Inner Detector tracks, the calorimeter deposits for a minimally ionizing particle, and Muon Spectrometer tracks. The emphasis is placed on the Inner Detector (ID) and Muon Spectrometer (MS). Four types of muons are reconstructed in the detector: [51]

- Combined muons which use a combination of ID tracks complementing MS tracks.
- Standalone muons which have reconstructed MS tracks which are detected outside the range of the ID ($|\eta| > 2.5$)
- Segmented-Tagged muons which have low transverse energy and thus do not permeate the entire MS, but are matched to an ID track.
- Calorimeter-Tagged muons which cover a difficult region for the MS reconstruction $|\eta| < 0.1$ and uses ID track information with calorimeter energy deposits.

The default muon reconstruction includes a combination of combined and standalone muons. Several optimisation criteria for each of the muon types and situations are defined further in References [52] and [51].

3.3.3 Jets

Jets are clusters of hadrons which leave energy deposits in the ATLAS detectors and originate from the same particle. [53][26] They are expected to occur from the Hadronization process (discussed in Section 2.1.3). These hadronization jets retain the name Jet while Jets formed from other events are named by the event (i.e. a hadronically decaying tau creates a jet which is named tau jet to differentiate it). The specific requirements for finding each type of jet for different situations varies. The basic structure of two of these procedures will be summarized here.

A fixed cone algorithm is used with the energy deposits collected by the calorimeters as input. These inputs are arranged by transverse momentum in descending order. A seed minimum energy threshold is determined as well as a fixed cone radius. The first input is compared to the threshold, and when it is of higher energy, it is used as a seed. A cone with the fixed cone radius chosen earlier is put around the seed. All inputs within the cone are combined and this creates a new seed which shifts the cone. The process is repeated until the cone no longer shifts and the resulting inputs which make up the seed are considered a jet. Then the next input from the list of ordered inputs is used as a seed. The process continues until all inputs which pass the minimum energy threshold have been used to create jets. The inputs, which have been used to construct one jet, may in turn be used to construct another creating an overlap between jets. A further step to correctly cluster the jets is to introduce a

merging and splitting iteration. This looks at the shared constituents and the percent of energy of the smaller jet that it accounts for. When the shared energy makes up a large portion of the smaller jet, the jets are combined. Conversely when it is a low energy, the jets are split.

A second algorithm is a sequential recombination algorithm, specifically the k_T algorithm for ATLAS. Every reconstructed detector object with an associated 4 momentum is put into a list. The objects are evaluated as pairs and individually by their relative transverse momentum squared p_T^2 . The minimum p_T^2 from all possible pair combinations and single objects is determined. When the minimum is a pair, the pair is combined into one object and the process repeats. When the minimum is a single object, that object is labeled a jet and removed from the listing. In this process, a term is added to the p_T^2 which is related to a distance of separation between two objects.

$$\Delta R = \sqrt{(\Delta\eta)^2 + (\Delta\phi)^2} \quad (3.5)$$

In the ATLAS experiment, $\Delta R < 0.4$ for the k_T algorithm. This allows some control over the size of a jet. [26] More information over the k_T algorithm can be found in Reference [54].

3.3.4 Taus

As introduced in Section 3.2, the tau lepton is recognized by its lifetime and hadronic decay channels. It can be seen in Figure 2.10 that the tau decays leptonically in 35% of events and hadronically in the other 65%. The leptonic decays of taus are reconstructed similarly to the electron and muon reconstruction methods. These are specifically difficult because of the undetected tau neutrinos, making the tau decay to lighter muons, and the direct creation of lighter muons hard to distinguish. The focus here will be on the hadronically decaying taus. Here the jet objects from the k_T algorithm (discussed in the previous section) are used as seeds themselves to a reconstruction of tau decay. Each jet object which exceeds a certain transverse momentum is considered as a possible tau jet. [55][28]

Tau Jets

There are some unique properties to the hadronic tau decays which help to separate it from other events. First, the decay products of the tau will be boosted in the same direction as the tau flight. The energy related to this boost has an effect on the degree of collimation of the decay products in the lab frame. This will cause some difficulty in vertexing which is also discussed in Section 5.1. However, this also means the jet objects from the previous section can be further parsed by narrowing $\Delta R < 0.2$. This can be seen in Figure 3.7. Once the jet objects encompass a smaller separation allowance, several other options are available to differentiate the tau jets from other jets. A Jet discrimination process is followed using cut based selection, projective likelihood identification, and identification with boosted decision trees. More detail on this process can be found in Reference [55]. The unique hadronic decays of the tau leave 1 track in the tracking system for 1pXn decays, 3 for 3pXn decays and 5 for the rarer 5pXn decays. With this information, criteria can be set on the number of tracks a jet contains. It is also useful to check that the reconstructed tracks originate from the same place. Tracks in close proximity can be erroneously contributed to the same jet. One method to account for this is to take the leading track in the jet (the track with highest p_T) and compare its impact parameter to the other tracks. When the difference between impact parameters is low, the tracks are said to originate from the same event. Finally, the tau jet mass can be reconstructed from the visible decay elements. This is

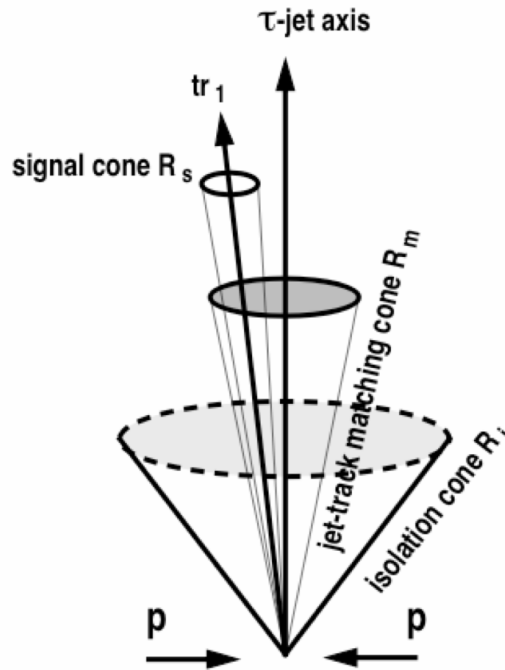


Figure 3.7: Collimation feature of tau jets. Taken from [56].

expected to be shifted slightly from the mass of the tau to account for the momentum carried by the neutrino. The method ATLAS uses for this mass reconstruction is the tau particle flow. This method is largely based on 4-momentum reconstruction from the visible tracks made by the decay products and the calorimeter deposits. [56][28]

Expected Pion Signatures in the ATLAS Detector

There are certain signatures expected from the decays of taus. The charged pions typically interact directly with the detector before decaying. They are tracked by the tracking system and interact with the calorimeter. For the relevant range, $15 \text{ GeV} < p_T < 100 \text{ GeV}$, the tracking system has the better performance. However the depositions in the calorimeter help to identify charged pions because of the shape of the shower created there. From these tracks, the momentum, charge, and direction can be determined. A pion mass is associated with the tracks for the reconstruction. 2% of tau jets will have the wrong number of tracks associated with them. [28] The neutral pions will decay to a pair of photons with a branching ratio of about 98%. [12] Half of these photons interact with the beam pipe and inner-detector material to create e^+ and e^- pairs which leave tracks in the ID and deposits in the eCAL. This leads to wider jet signatures and decreases the efficiency of separation from the background. The photons which do not create these pairs also leave eCAL deposits but no tracking information in the ID. The shower they produce there can be separated from the charged pion deposits by the shape. The majority of the energy from the neutral pion is deposited in the first EM detector, while the charged pion leaves a regular staggered energy deposit in each of the sequential EM calorimeters. This also comes with challenges since the boosted particles will often leave overlapping

energy deposits. In the case of five charged pion decays, the branching ratio is very low, and the jet becomes less collimated making it also difficult to distinguish from background. For this reason, only decays with 1 or 3 charged hadrons are considered for tau reconstruction. The efficiency matrix for decay mode reconstruction can be seen in Figure 3.8. More information on the reconstruction can be

Reconstructed decay mode	ATLAS Simulation Tau Particle Flow (π^0 reconstruction) $Z/\gamma^* \rightarrow \tau\tau$				
	h^\pm	$h^\pm \pi^0$	$h^\pm \geq 2\pi^0$	$3h^\pm$	$3h^\pm \geq 1\pi^0$
$3h^\pm \geq 1\pi^0$	0.2	2.5	3.5	11.0	55.3
$3h^\pm$	0.2	0.6	0.4	86.8	41.5
$h^\pm \geq 2\pi^0$	1.2	12.4	39.6	0.2	0.7
$h^\pm \pi^0$	9.7	67.5	50.9	0.7	2.1
h^\pm	88.6	16.9	5.6	1.4	0.5

Diagonal fraction: 70.9%

Figure 3.8: Decay mode efficiency matrix showing the probability of a reconstructed decay mode given a certain generated decay mode. Taken from [28].

found in References [28], and [55].

3.3.5 Vertex and Track Association

The proton-proton collisions at the LHC are used to generate hard scattering interactions. However, these are not the only interactions which can occur, and in fact several other soft processes occur which create a background noise in the detector. Such processes are termed pile-up and can affect the collision of creation as well as the preceding and subsequent collisions. [57] Typically, the primary vertex (which is from the hard scattering) has the most associated tracks. However, as the number of pileup interactions increases, the likelihood of incorrectly identifying the primary vertex also increases (Figure 3.9). The Tau Jet Vertex Association (TJVA) is an algorithm for determining the true primary vertex amidst the increased pileup. For each vertex candidate, a Jet Vertex Fraction F_{JVF} is determined by taking the sum of momentum of each τ jet track associated to the vertex and dividing by the sum of momentum from all τ jet tracks

$$f_{JVF}(\text{jet}|\text{vtx}) = \frac{\sum p_T^{\text{trk}|\text{vtx}}}{\sum p_T^{\text{trk}}}. \quad (3.6)$$

An illustration of the algorithm is shown in Figure 3.10. The tracks which are used with each τ jet before using the algorithm are: [58]

1. $p_T > 1$ GeV,
2. Number of ID pixel hits ≥ 2 ,

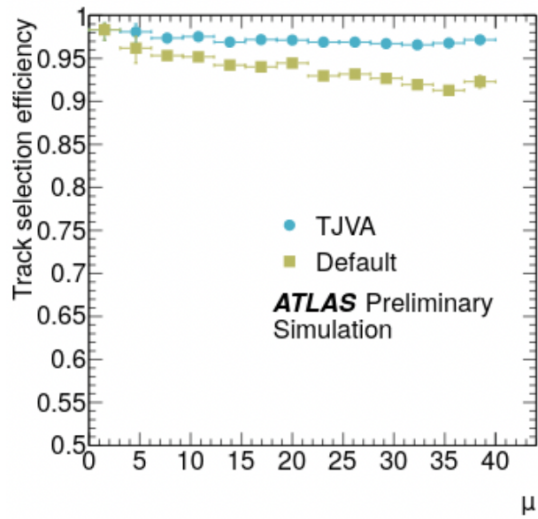


Figure 3.9: τ track selection efficiency for hadronically decaying τ s at different mean values of pile up events. Taken from [58].

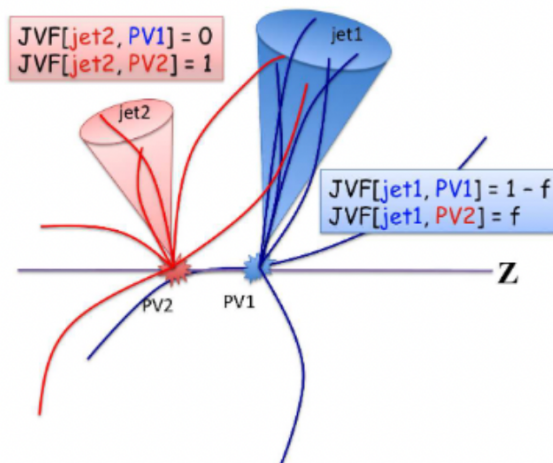


Figure 3.10: A simple example of the algorithm used in the TjVA. Taken from [58].

3. Number of ID pixel and SCT hits ≥ 7 .

After the f_{JVF} is assigned, further criteria are added:

1. $|d_0| < 1.0$ mm,
2. $|z_0 \sin \theta| < 1.5$ mm,

d_0 and z_0 represent the distance of closest approach. Assigning these after vertex selection decreases the likelihood that a τ track is rejected due to an erroneous first primary vertex assignment. [58]

3.3.6 Missing Transverse Energy E_T^{miss}

E_T^{miss} should include the energy which was not measured by the detector. This includes the energy which is carried by rarely-interacting particles like neutrinos. The E_T^{miss} is calculated based on the reconstruction of each of objects occurring in an event. Because the transverse energy of the colliding partons is zero, the sum of all transverse energies of resulting objects should also add to zero. The z -component of the energy is not known exactly and so momentum conservation cannot be exploited to the same degree as the transverse directions. The energy of those particles which did not interact with the detector can then be determined as the deviation from zero in the following equation [59]

$$E_{x,y}^{miss} = - \left(\sum p_{x,y}^e + \sum p_{x,y}^\gamma + \sum p_{x,y}^{\tau had} + \sum p_{x,y}^\mu + \sum p_{x,y}^{jet} + p_{x,y}^{soft} \right). \quad (3.7)$$

The soft term in Equation 3.7 comes from the tracks which were not used in the reconstruction of any objects but were associated to the event vertex. The used observables for the missing energy can be determined using Equation 3.7 [59]

$$E_T^{miss} = \sqrt{(E_x^{miss})^2 + (E_y^{miss})^2} \quad (3.8)$$

$$\phi^{miss} = \tan^{-1} \left(\frac{E_y^{miss}}{E_x^{miss}} \right) \quad (3.9)$$

This gives a final magnitude and direction of the combined E_T^{miss} for the event. Further information on this process can be found in References [59] and [60].

3.4 Data and Simulations

Modeling High energy collisions of composite particles (like the proton) can prove challenging. Several physical processes which occur within the collisions are non-perturbative and cannot yet be calculated. Other perturbative processes which can be calculated are still computationally difficult and become even more so as calculations of higher order interactions are performed. The range of momentums involved with each run (GeV to TeV), as well as the number of particles ($O(100) - O(1000)$), requires a robust calculation to recreate the event. [61] In order to do this, Monte-Carlo methods are used (a short introduction to Monte-Carlo methods is given in Section 4.1.1) to provide simulations of the collision event and the particles produced. [62]

The initial simulation of events producing particles is referred to as true or truth information. After the simulation of the event, the detector must also be simulated along with what signatures the simulated event would leave there. The reconstruction techniques mentioned earlier are applied to these simulated signatures, and the resulting information is called reconstructed information. For example, with the full simulation data for a single $H \rightarrow \tau\tau$ event, a true τ object which has the truth information from the event simulation will exist alongside a reconstructed τ object which is reconstructed using the methods from Section 5.1 applied to the simulated detector response.

For all events in this thesis, the same simulated sample of events were used for $H \rightarrow \tau\tau$ processes, mc16_13TeV.345123.PowhegPy8EG_NNLOPSn_nlo_30_ggH125_tautauh30h20.recon.-AOD.e5814_s3126_r10201. Three separate samples for $Z \rightarrow \tau\tau$ were used, mc16_13TeV.361108.-PowhegPythia8EvtGen_AZNLOCTEQ6L1_Ztautau.recon.AOD.e3601_s3126_r9364, mc16_13TeV.-361108.PowhegPythia8EvtGen_AZNLOCTEQ6L1_Ztautau.deriv.DAOD_HIGG4D3.e3601_s3126_r10239, mc16_13TeV.361108.PowhegPythia8EvtGen_AZNLOCTEQ6L1_Ztautau.recon.AOD.e3601_s3126_r10724. These samples were generated using POWHEG along with PYTHIA8. More about the specific generators can be found in References [63], [64], [65], and [66].

Higgs Boson Mass from τ Decay

4.1 Monte-Carlo Methods

Monte Carlo methods are a class of computational algorithms which use repeated random sampling to approximate distributions and solutions. These random samples are taken from a given probability distribution so that as the number of samples increase, the accuracy of the approximation also increases. This way, the characteristics of a distribution can be determined directly from the sampled objects, which can be faster and easier to do than analytical integration. [67]

4.1.1 Markov Chain Monte-Carlo (MCMC)

The MCMC is a special class of Monte-Carlo algorithms. It is set apart by the sequential nature of the random sampling process. For the target distribution which would be sampled, a set of states exist which are possible. Each of these states has a probability of being accepted after being randomly selected. This probability is related directly to the current state but not to any previous states. An example may run as follows:

1. Start with a probability density and randomly generate one sample from within it. This sample has a probability associated to the probability density from which it was sampled.
2. Now randomly sample from the distribution again. This new sample also has a probability associated with it.
3. Compare the probabilities of each sample from 1 and 2.
 - If the probability from 2 is higher than 1, then the sample from 2 is accepted and becomes the current state.
 - If the probability from 1 is higher than 2, then randomly decide if 2 is accepted and becomes the current state, using an acceptance value which is proportional to the difference in probabilities.
4. Using the current state as in 1, repeat the process starting at 2.

When performing this type of algorithm, it is important to pick a good starting point. When the starting point is in the tail of the distribution, or outside the distribution altogether, the resulting sampling

will not accurately represent the distribution. It is also possible to overcome this by not including the initial steps in the final collection of samples. The amount of steps to ignore is proportional to the relative distance from the center of the target distribution. An example of distribution modeling at different starting points can be seen in Figure 4.1. More information on MCMC algorithms can be found in Reference [68], which is where much of the information in this section was taken.

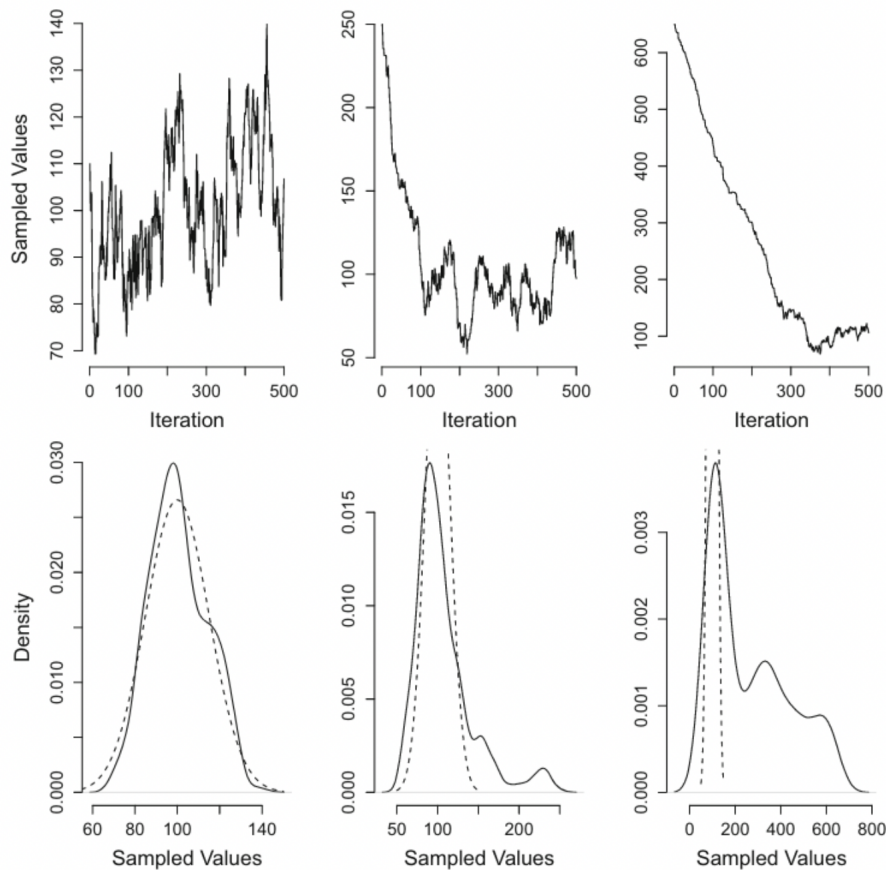


Figure 4.1: From left to right the distributions on top show the accepted sampling values from MCMC at each iteration while the bottom shows the dashed PDF of a gaussian centered at 100 with the solid line of total samples accepted from the MCMC process with starting points farther away from the center of the target distribution. Taken from [68].

4.1.2 Metropolis Hastings (MH) Algorithm

This section is an overview of the MH algorithm (gathered mostly from Reference [69]) which is implemented in both the MMC (Section 4) and in the additional vertex studies (Section 5.3.2). The MH algorithm is advantageous for its versatility and relative simplicity in the MCMC category. Using this algorithm, the entire distribution is modeled by sampling locally until a global picture is uncovered. The MH requires two distributions, the target distribution π , and the conditional density q , also called the proposal kernel. The general process of the algorithm is:

1. Start with the value x at the current position t within the Markov Chain $X^{(t)} = x$.
2. Generate a new random value y from the domain of π .
3. Determine the probability with which Y becomes the next value in the MCMC $X^{(t+1)}$.
 - $\frac{\pi(y) q(x|y)}{\pi(x) q(y|x)}$
4. Accept $X^{(t+1)} = y$ or reject $X^{(t+1)} = x$ with the probability from 3.
5. Repeat from 2.

This method is sensitive to the conditional density q . When 4 is too restrictive, the algorithm is unable to step to all areas within a distribution. This results in a highly weighted representation of the local distribution, with little to no samples from other areas. Generally, ensuring that q is positive in the entire domain of π allows for a representative sampling. Even with this condition, the amount of iterations required to accurately represent the distribution is dependent on q . In fact, the versatility of this algorithm allows for almost any choice of proposal kernel q . The choice however has a direct impact on the convergence of the algorithm. It is therefore important to select a good choice of q so that the required iterations remain relatively low. This process is used to probe the parameter space for neutrino solutions (Section 4.2.2) and to find useable solutions to the vertex based \mathbf{P}_τ reconstruction (Section 5.3.2).

4.2 Missing Mass Calculator (MMC)

The goal of the MMC is to reconstruct the event kinematics of decays to two τ s. Since the information provided by the detector is incomplete (neutrinos are rarely reacting and the energy they carry is therefore unknown), the reconstruction cannot be exactly determined. However, the resolution of such solutions can be improved and in this section the methodology for such improvement is introduced. Most of the information in this chapter is taken from References [70] and [7], and more information on the MMC can be found there.

4.2.1 $\tau\tau$ Event Kinematics Reconstruction

The MMC makes two assumptions when reconstructing the event kinematics. First, that the τ is highly boosted, $m_{H/Z} \gg m_\tau$. Second, neglecting detector resolutions and other detection limitations, the only objects not accounted for in the detector reconstruction are the neutrinos. Each neutrino will then have three unknown parameters corresponding to the three-dimensional momentum vector. In the case that the τ s decay leptonically, there is an additional unknown in the invariant mass of the associated neutrino system. Therefore every reconstruction includes at least six and at most eight unknown parameters. The Equations which describe the kinematics are [7]

$$E_x^{miss} = p_\nu^l \sin \theta_\nu^l \cos \phi_\nu^l + p_\nu^s \sin \theta_\nu^s \cos \phi_\nu^s \quad (4.1)$$

$$E_y^{miss} = p_\nu^l \sin \theta_\nu^l \sin \phi_\nu^l + p_\nu^s \sin \theta_\nu^s \sin \phi_\nu^s \quad (4.2)$$

$$(M_\tau^l)^2 = (m_\nu^l)^2 + (m_{vis}^l)^2 + 2\sqrt{(p_{vis}^l)^2 + (m_{vis}^l)^2} \sqrt{(p_\nu^l)^2 + (p_{miss}^l)^2} \quad (4.3)$$

$$(M_{\tau}^s)^2 = (m_{\nu}^s)^2 + (m_{\nu_{vis}}^s)^2 + 2\sqrt{(p_{\nu_{vis}}^s)^2 + (m_{\nu_{vis}}^s)^2}\sqrt{(p_{\nu}^s)^2 + (p_{miss}^s)^2}. \quad (4.4)$$

m_{ν} is the invariant mass term associated with a leptonically decaying τ systems. The superscript l and s stand for leading and subleading. These describe an identification characteristic for the separate τ s in ditau events. The leading τ is the one with higher p_T . The work in this thesis uses only the hadronically decaying τ s and therefore this term is always zero. The higher number of unknowns than equations prevents exact solutions. However, it is possible to weight solutions based on the likelihood of occurrence. For example, the angle between $\mathbf{p}_{\nu_{vis}}$ and \mathbf{p}_{ν} can be extrapolated from the τ decay kinematics.

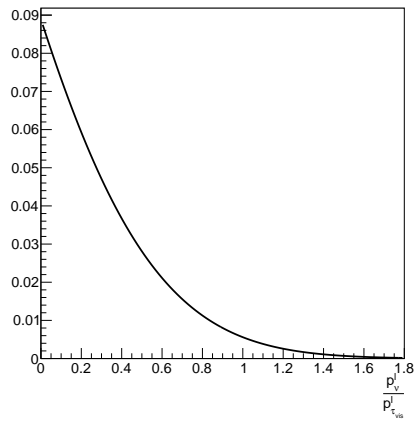
4.2.2 Weighting Reconstruction Solutions

A Markov Chain Monte Carlo Method, the Metropolis Hastings Algorithm (see Section 4.1.2) is used to scan the parameter space. This parameter space is filled by the x and y components of the neutrino momentums, which combined make up the E_T^{miss} variable. The best solution is determined using a likelihood approach. The total weight of each proposed solution is a sum of sub-weights determined from distributions based on an ensemble of simulated events [71]

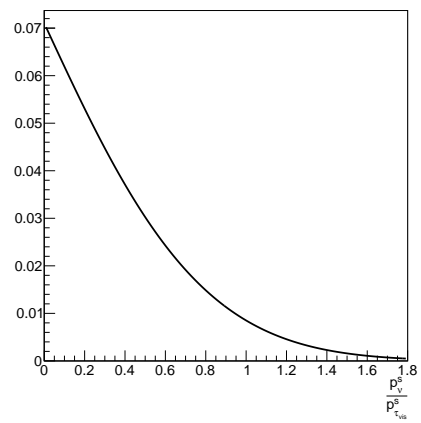
$$\text{weight} = P(\Delta\theta^l) \cdot P(\Delta\theta^s) \cdot P(\Delta E_{T,x}^{miss}) \cdot P(\Delta E_{T,y}^{miss}) \cdot P(R^l) \cdot P(R^s). \quad (4.5)$$

$\Delta\theta$ for leading and subleading τ s corresponds to the angle between \mathbf{p}_{ν} and $\mathbf{p}_{\nu_{vis}}$. $P(R)$ is the ratio $\frac{p_{\nu}}{p_{\nu_{vis}}}$ and $\Delta E_{T,(x,y)}^{miss}$ is the difference between the original values of $E_{T,(x,y)}^{miss}$ with the values from the scan. The probability distributions differ depending on the type of decay which occurs, two leptonically decaying τ s, one leptonically and one hadronically decaying τ , or two hadronically decaying τ s. The hadronically decaying τ s also have separate distributions for decays containing one or three charged π^{\pm} . For every event, a scan is performed by making an initial seed to an MH algorithm corresponding to the reconstructed neutrinos. Every iteration of the MH calculates the weight of the next proposed solution and follows the general process described in Section 4.1.2. Additional restrictions to these solutions are used in order to reduce execution time since unreal solutions may be iterated through in the MH without them.

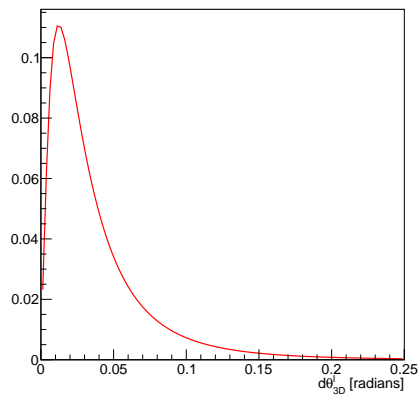
The PDFs in the MMC are parametrised by p_T and dependent on the decay type (leptonic or hadronic) and decay mode for hadronic decays. To illustrate some example PDFs, a specific event has been chosen from the $3p0n$ decay mode and the p_T of the τ s (47639 for the leading τ and 42810 for the subleading τ) from this event were used to generate the PDFs. (Figures 4.2(a), 4.2(b), 4.2(c), and 4.2(d)) The event used will be revisited in Chapters 6 as the example to show the effects of this study.



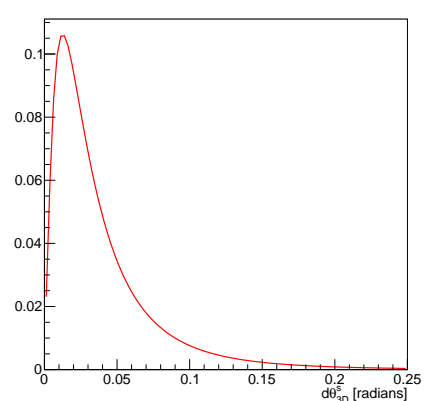
(a) $\frac{p_v^l}{p_{\tau_{vis}}^l}$ PDF in the MMC.



(b) $\frac{p_v^s}{p_{\tau_{vis}}^s}$ PDF in the MMC.



(c) $d\theta_{3D}^l$ PDF in the MMC.



(d) $d\theta_{3D}^s$ PDF in the MMC.

Introduction of Vertex Information

The reconstruction of the τ jet objects (see Section 3.3.4) includes information on both the primary (production) and secondary (decay) vertices of the tau. This information is not yet used inside the MMC (see Chapter 4) and the aim of the next two chapters is to include this information in an attempt to increase the accuracy of the MMC output. This starts with an analysis of the available vertex reconstruction in Section 5.1. Then a vertex-based kinematic solution is introduced in Section 5.2. From this solution new PDFs similar to those present in the MMC will be created. When the width of these PDFs is comparable or less than those in the MMC, it is expected that the MMC should improve. With this motivation, a single event PDF which is related to the event uncertainties themselves is thought to improve at least a portion of the events. Some of the difficulties which arise in this method are discussed as well as an approach to fix them (Section 5.3).

5.1 Vertex Reconstruction

The vertex information was determined in the event reconstruction algorithm in ATLAS. It is important to see the resolutions of these vertices as the accuracy of any value derived from vertex information will be heavily influenced by this resolution. It can be seen from Figure 2.10 that the percentage of taus which decay via $3p0n$ is around 9%. However, the events of highest interest have 2 taus decaying through this mode. A plot showing the percentage of events which pass this selection is shown in Figure 5.1. An investigation into the Vertex information for the specific $H \rightarrow \tau\tau \rightarrow 6\pi^\pm 2\nu_\tau$ is assessed in the following sections. Using the notation defined in Section 2.3, the categories 0-4 in Figure 5.1 represent $1p0n$, $1p1n$, $1pXn$, $3p0n$, and $3pXn$ respectively. The x -axis is the leading τ and the y -axis is the subleading τ . It can be seen that the target $3p0n$ decay represented by category 3 for both the leading and subleading τ represent approximately 2% of all $H \rightarrow \tau\tau$ events. While this is a low percentage, it represents the case with the potential for the best reconstruction (no other neutral particles besides neutrinos, and multiple tracks for secondary vertex reconstruction). Therefore, this is the starting case, with room in the future to expand the process to include other decay modes.

5.1.1 Primary Vertex

The primary vertex of the Tau is the vertex where the Higgs Boson decays into two τ leptons. Because the Higgs decays so fast, it is not possible to separate the production vertex of the Higgs with the decay

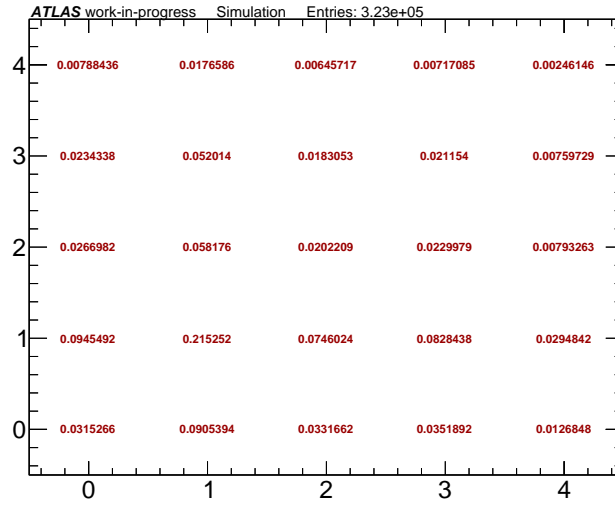


Figure 5.1: Fraction of τ decays in $H \rightarrow \tau\tau$ events.

vertex of the Higgs. This means that the production vertex of the tau is the same as the production vertex of the Higgs. This vertex contains numerous tracks as seen in Figure 5.2, aiding in the resolution of the vertex position. However, there are still some difficulties in reconstructing this vertex. As

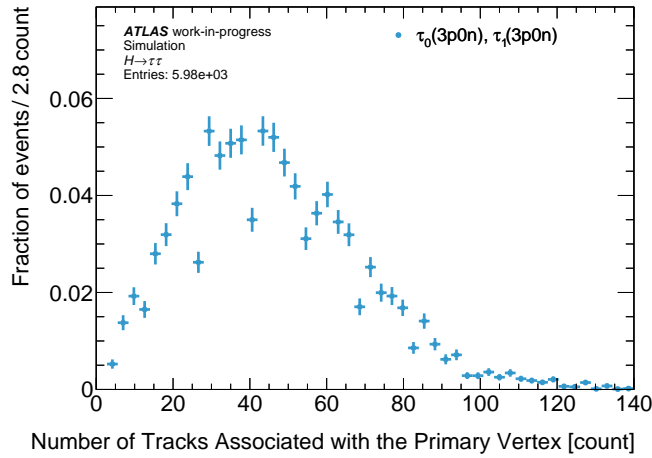
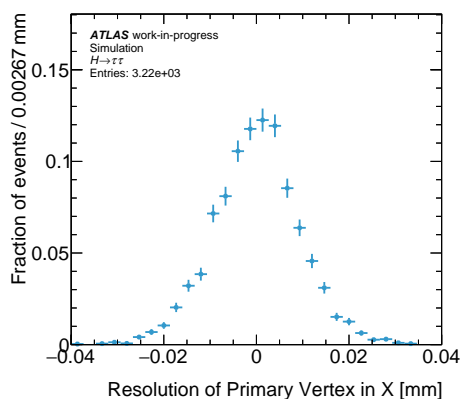
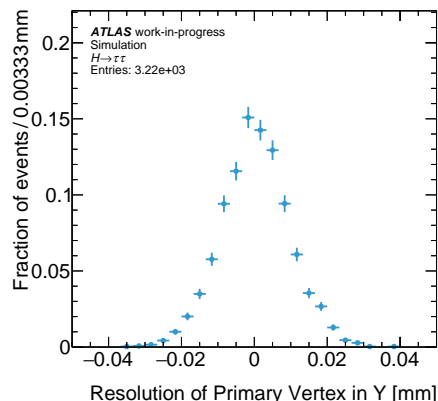
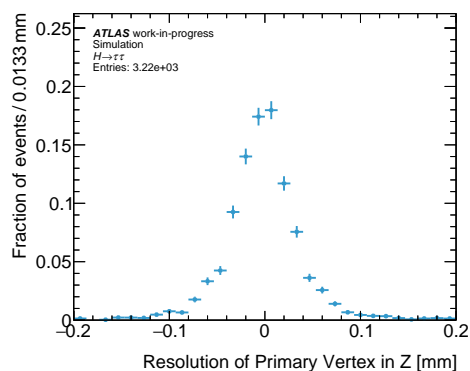


Figure 5.2: Number of reconstructed tracks associated with the primary vertex of ditau events with both τ s in decay mode $3p0n$.

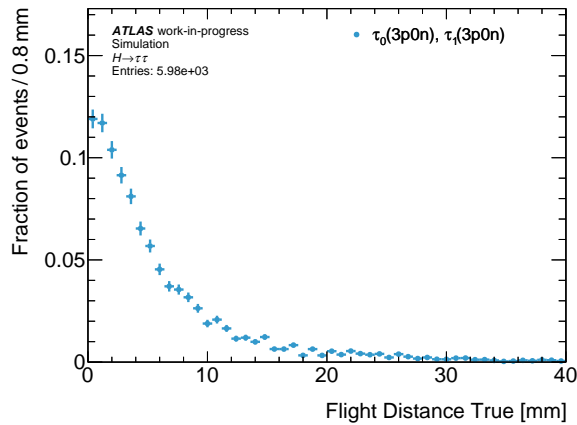
mentioned in Section 2.2.2 and 3.2.1 the partons of the colliding particles do not generally carry the same energy. This results in a boost along the beamline in the z -axis. The degree of separation between tracks in this direction is then smaller, and the tracks are harder to separate the closer they are analyzed to the nominal production point. Due to this, the uncertainty along the z -axis is greater in the plane perpendicular to the beam. In Figures 5.3(a) and 5.3(b) the resolution in the x and y -axes can be seen, while Figure 5.3(c) shows the z -axis resolution. The resolutions are determined as follows. First, a simulation of possible events which could occur in the proton-proton collision is created (for

(a) Primary vertex resolution on the x -axis.(b) Primary vertex resolution on the y -axis.(c) Primary vertex resolution on the z -axis

this thesis, only those events which contained $H \rightarrow \tau\tau$ decays were used). This is known as the truth information. Then a simulation of the ATLAS detector will give detection signatures which would be expected in such simulated events. These signatures are run through reconstruction algorithms, creating particle objects. This is known as the reconstructed information. The difference between the reconstructed information and the truth information, can then be analysed to determine a resolution, or spread in error. The distributions of the vertex errors were roughly gaussian (as seen in Figures 5.3(a), 5.3(b), and 5.3(c)), and so a gaussian fit was administered to determine a one σ width for the primary vertex, $\sigma_x \approx \sigma_y \approx 9 \mu\text{m}$ and $\sigma_z \approx 30 \mu\text{m}$.

5.1.2 Secondary Vertex

The relatively large mass of the τ lepton is reflected in its short lifetime as several more avenues of decay are available than the lower generation leptons. Even when boosted from the Higgs decay, the τ will not generally reach the Inner Detector (The first inner detector pixel resides 33.25 mm from the beamline. [72]) However, most τ s will produce a large enough decay distance in the lab frame for the primary and secondary vertices to be distinguished. Figure 5.4 shows the spread of the decay distances in the lab frame. These are defined as the distance between the primary and secondary τ vertices. Since the τ decays before the start of the tracking system, the decay vertex must be reconstructed

Figure 5.4: Decay distance for the τ in the lab frame.

solely from the tracks of the decaying particles. The reconstruction of the secondary vertex is more difficult than the primary. A major reason is the lack of tracks associated to the vertex. Here, there should only be three as opposed to the large number of tracks typically associated with the primary vertex. The secondary vertex is boosted in the direction of τ flight. As with the primary vertex, this makes the position in the direction of the boost harder to determine. Since the tau is boosted along the z -axis, the largest component of the boost to its decay products lie in the z -axis. Therefore, it is possible to see a similar effect to the resolutions as was seen for the primary vertex, but scaled to higher errors. The x and y -axes resolutions can be seen in Figures 5.5(a) and 5.5(b) respectively, and the z -axis resolution can be seen in Figure 5.5(c). The resolutions were calculated similarly to the primary vertex resolutions and the resulting uncertainties are $\sigma_x \approx \sigma_y \approx 100 \mu\text{m}$ and $\sigma_z \approx 1000 \mu\text{m}$.

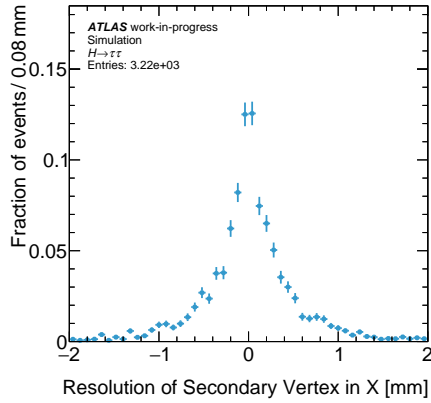
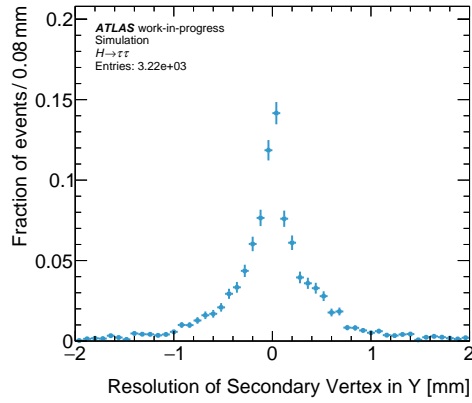
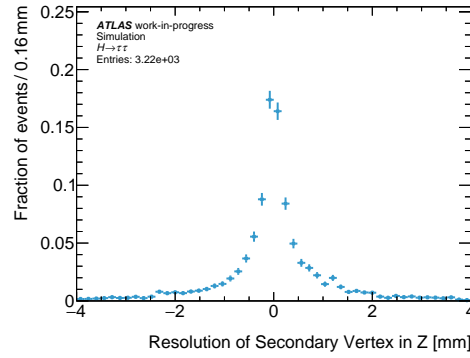
5.2 Kinematics of the $\tau \rightarrow \nu_\tau 3\pi^\pm$ Decay

The Kinematic reconstruction derived from the visible decay tracks is already implemented in the MMC. In this section P_τ and P_ν will be derived from both the visible tracks, and the vertex information. These newly derived solutions should complement the ones already in the MMC, and for some events give tighter constraints for more accurate reconstruction. First, the physical and mathematical concept of the reconstruction is realised in Section 5.2.1. Then, the handling of the errors arising from the vertex information is discussed (Section 5.2.2). An ambiguity which arises from this is briefly considered in Section 5.2.3 and in more detail in Section 6.2. Finally the 5 PDFs which will be added to the MMC are discussed in Section 5.2.4.

5.2.1 Kinematics from Vertex Information

The $\tau \rightarrow 3\pi^\pm \nu_\tau$ decay can be probed using the energy-momentum relation:

$$E_\tau^2 = m_\tau^2 + p_\tau^2. \quad (5.1)$$


 (a) Secondary vertex resolution on the x -axis.

 (b) Secondary vertex resolution on the y -axis.

 (c) Secondary vertex resolution on the z -axis.

In terms of the τ four momentum P_{τ_i} with $i \in E, p_x, p_y, p_z$ the equation becomes

$$P_{\tau_0}^2 = M_\tau^2 + p_{\tau_1}^2 + p_{\tau_2}^2 + p_{\tau_3}^2. \quad (5.2)$$

Here, the components of P_{τ_i} cannot fully be realised since the neutrino component is not measured. Now, it is possible to add the information provided by the vertices. A τ flight direction can be determined by taking the shortest distance between the two vertices. This does not account for any curvature in the τ track. It is assumed that the distance in the laboratory frame is sufficiently small and the momentum of the τ is sufficiently large for this assumption to be accurate enough. The vector of tau flight is then given as $\mathbf{R} = \hat{r}_1, \hat{r}_2, \hat{r}_3$ with $(1, 2, 3) = (x, y, z)$. Using the substitution

$$\frac{p_{\tau_1}}{p_{\tau_2}} = \frac{\hat{r}_1}{\hat{r}_2}, \quad \frac{p_{\tau_1}}{p_{\tau_3}} = \frac{\hat{r}_1}{\hat{r}_3} \quad (5.3)$$

Equation 5.2 becomes

$$p_{\tau_0}^2 = m_\tau^2 + p_{\tau_1}^2 + \left(\frac{\hat{r}_2 p_{\tau_1}}{\hat{r}_1} \right)^2 + \left(\frac{\hat{r}_3 p_{\tau_1}}{\hat{r}_1} \right)^2. \quad (5.4)$$

Equation 5.4 now has only 2 unknown variables, the energy of the τ P_{τ_0} and the x component of the τ momentum, P_{τ_1} .

Similarly, the unknown ν_τ four momentum can be described as

$$P_{\nu_0}^2 = m_\nu^2 + p_{\nu_1}^2 + p_{\nu_2}^2 + p_{\nu_3}^2 \quad (5.5)$$

where $m_\nu^2 = 0$ in the used calculation. From momentum conservation, \mathbf{P}_τ can be written in terms of \mathbf{P}_ν and \mathbf{P}_{vis}

$$\begin{pmatrix} E_\tau \\ P_{\tau_x} \\ P_{\tau_y} \\ P_{\tau_z} \end{pmatrix} = \begin{pmatrix} E_{vis} \\ P_{vis_x} \\ P_{vis_y} \\ P_{vis_z} \end{pmatrix} + \begin{pmatrix} E_\nu \\ P_{\nu_x} \\ P_{\nu_y} \\ P_{\nu_z} \end{pmatrix}. \quad (5.6)$$

\mathbf{P}_ν can be substituted using Equation 5.6.

$$(p_{\tau_0} - p_{vis_0})^2 = (p_{\tau_1} - p_{vis_1})^2 + \left(\frac{\hat{r}_2 p_{\tau_1}}{\hat{r}_1} - p_{vis_2}\right)^2 + \left(\frac{\hat{r}_3 p_{\tau_1}}{\hat{r}_1} - p_{vis_3}\right)^2. \quad (5.7)$$

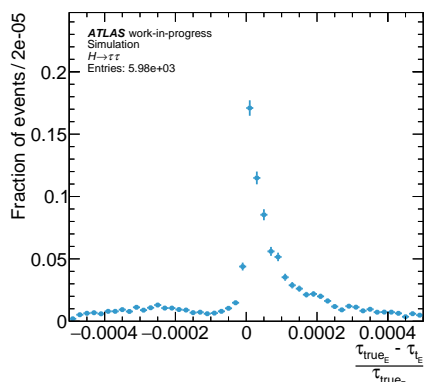
Now there are two equations (Equation 5.2 and Equation 5.7) with two unknown variables, P_{τ_0} and P_{τ_1} . Although these equations may seem straightforward to solve, the solution is mathematically labored. The solution can be found in Appendix A.2. It was initially tested with random variables unrelated to expected \mathbf{P}_τ values. It was found to be accurate within $\approx 10^{-13}$. Then a test with the values from the simulations was conducted. The truth information was used to determine \mathbf{P}_{vis} and vertex positions for the τ . These were then used to solve the equations shown in Appendix A.2. The true \mathbf{P}_τ was compared to the \mathbf{P}_τ which was calculated using the true \mathbf{P}_{vis} and vertex positions. Figures 5.6(a), 5.6(b), 5.6(c), and 5.6(d) show the results. The final solutions show a slight shift to values lower than the true value. However, the errors are mostly less than 0.02%. Although this is not as accurate as the dummy data, it is still sufficient to believe that the solution can accurately be determined. The differences in error could come from the differences in the degree to which information was stored inside the respective four momentum objects.

5.2.2 Propagation of Errors

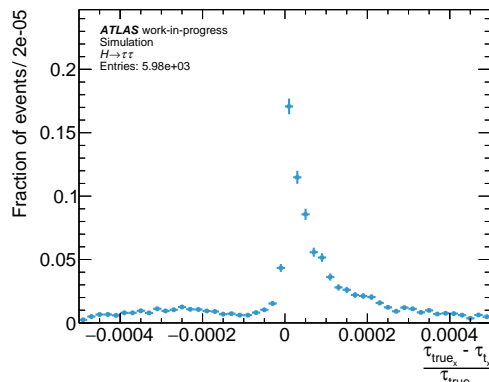
Once the validity of the Kinematic solution is determined using the truth information, it is important to ascertain the accuracy of the solution which comes from reconstructed information. The simulated detector response to the events is used to determine the values of \mathbf{P}_τ . Again, \mathbf{P}_{vis} is determined from the tracks which are created in the detector and the vertex information is determined also from the track information. The large secondary vertex errors which were seen in Section 5.1.2 will contribute to the error in the total \mathbf{P}_τ determination. This is made very evident when only a portion of the total events ($\approx 40\%$) produce real numbers for the P_τ solution seen in Figure 5.7. The percentage by which the real-solution reconstructed values differ from the true solutions can be seen in Figures 5.8(a), 5.8(b), 5.8(c), and 5.8(d). The errors are increased here significantly. When fitting the core peaks to a gaussian, the mean was found to be shifted by $\approx 8\%$ while the width was $\approx 17\%$. These graphs did not include the $\approx 60\%$ of events which returned unreal solutions. The specifics of this observed effect are covered in more detail in Section 5.3.

The initial approach to the large portion of unusable solutions, was to introduce two new selection

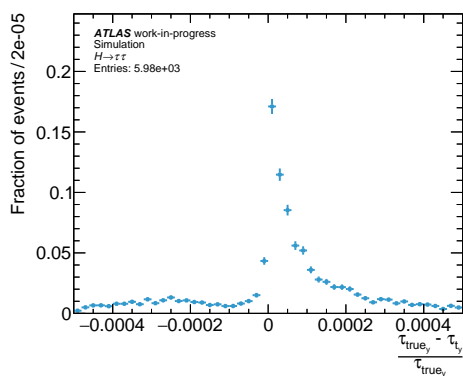
5.2 Kinematics of the $\tau \rightarrow \nu_\tau 3\pi^\pm$ Decay



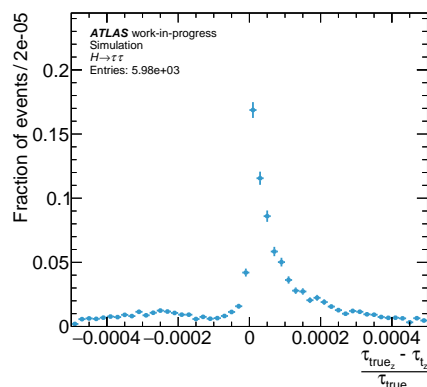
(a) Difference in true and reconstructed P_{τ_0} as a percentage of the true value.



(b) Difference in true and reconstructed P_{τ_1} as a percentage of the true value.



(c) Difference in true and reconstructed P_{τ_2} as a percentage of the true value.



(d) Difference in true and reconstructed P_{τ_3} as a percentage of the true value.

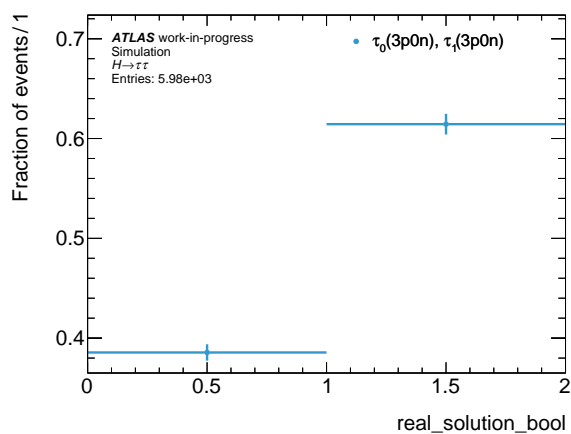
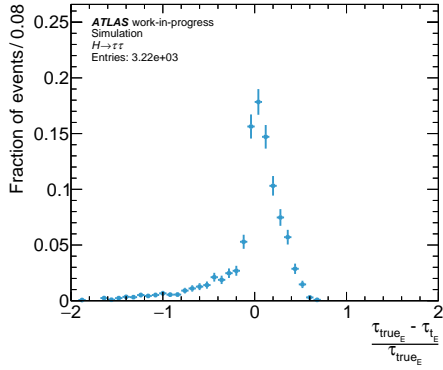
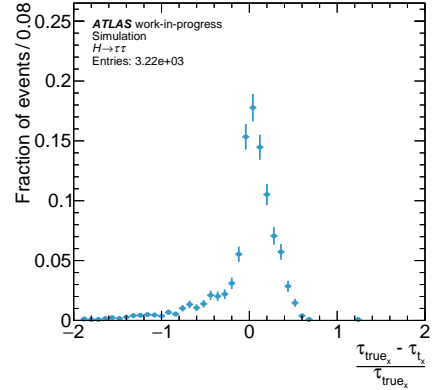


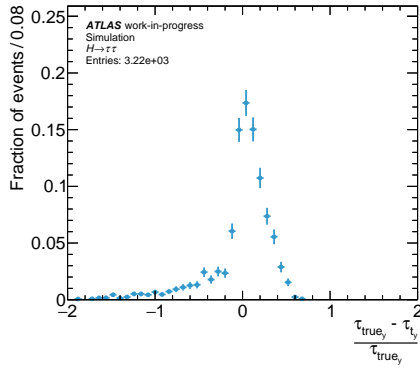
Figure 5.7: Boolean for useable solutions. 0 on the x -axis corresponds to a real solution. 1 corresponds to an unreal solution.



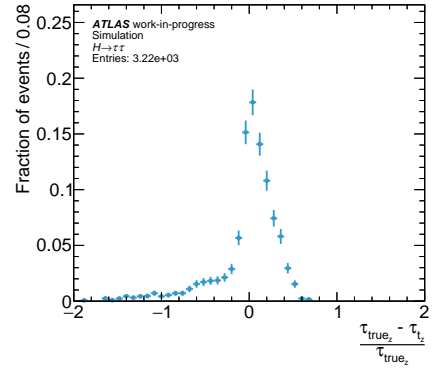
(a) Difference in true and reconstructed P_{τ_0} as a percentage of the true value.



(b) Difference in true and reconstructed P_{τ_1} as a percentage of the true value.



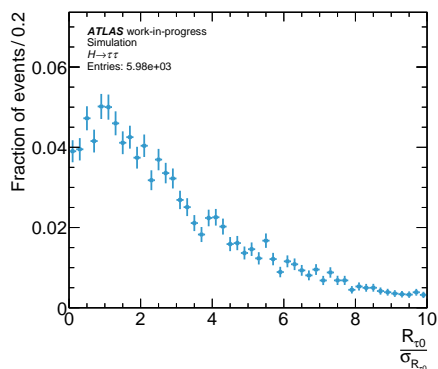
(c) Difference in true and reconstructed P_{τ_2} as a percentage of the true value.



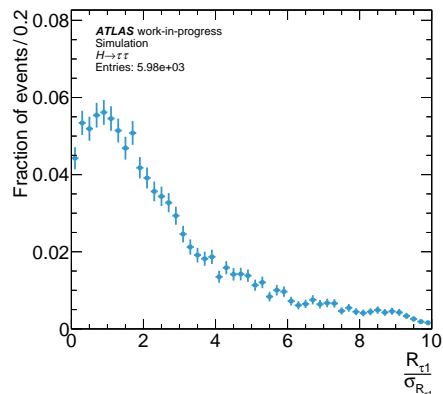
(d) Difference in true and reconstructed P_{τ_3} as a percentage of the true value.

cuts. The first cut is on the τ flight distance error σ_R as a proportion to the τ flight distance R . R is the magnitude of the flight path of the τ determined directly from the two vertex positions. σ_R is determined by error propagation from the six vertex position variables and their associated errors. All $\frac{R}{\sigma_R}$ values which were less than one were cut. These values corresponded to the events where the error of the flight distance was larger than the flight distance itself. In Figures 5.9(a) and 5.9(b), the distribution of $\frac{R}{\sigma_R}$ is shown.

Further a second selection criterion was added. This criterion was not based on the vertex error but on the correct identification of visible tracks. For a selection of events, the reconstructed momentum of the decay tracks differs significantly from the actual momentum of the particles which created the tracks. This can happen as an effect of the collimation of the particles, where some momentum left by one track is attributed to a different track. Therefore the momentum of the reconstructed tracks was matched to that of the true decay particles. When the difference exceeded 10% of the true decay particle's momentum, the event was cut from the used data. Figure 5.10 shows the distribution of momentum matched tracks for both leading and subleading τ s. This occurs after both the $3p0n$ cut and the $\frac{R}{\sigma_R} > 1$ cut are applied. This reduces the percentage of unusable events slightly as seen in Figure 5.11. Although several events still return unusable solutions, instead of placing more restrictive cuts, a method for obtaining useable solutions from those events was researched. An in-depth look at



(a) Leading τ flight distance divided by its error.



(b) Subleading τ flight distance divided by its error.

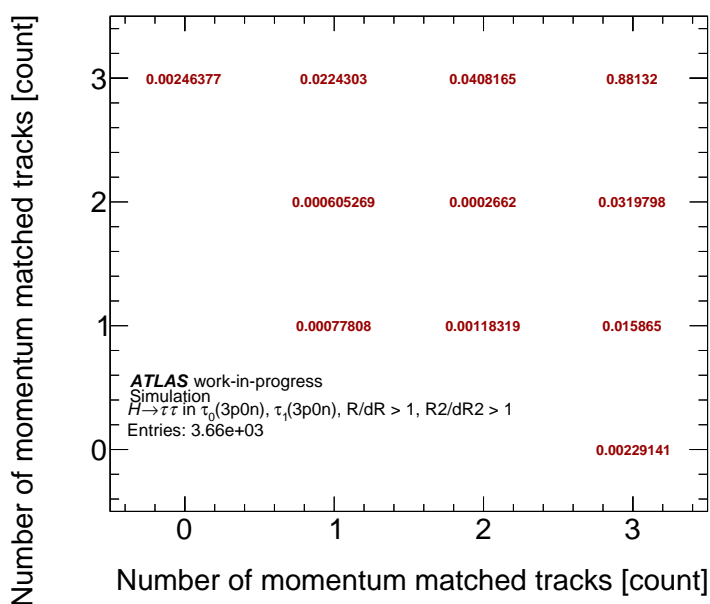


Figure 5.10: The fraction of momentum matched tracks for leading and subleading τ s. The x -axis contains the number of tracks which were within 10% of the corresponding truth information for $3p0n$ decays of the leading τ . They y -axis contains the same for the subleading τ .

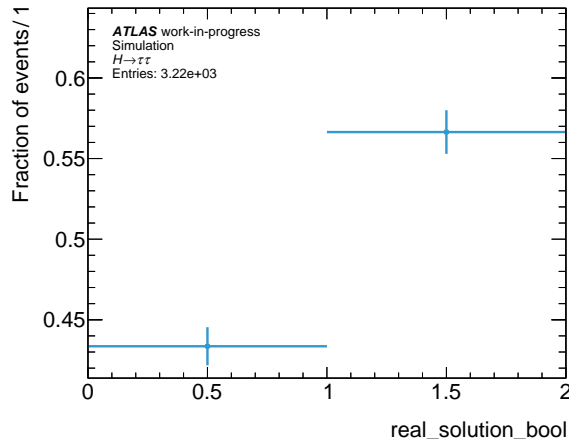


Figure 5.11: Boolean for useable solutions after the addition of new cuts. 0 on the x -axis corresponds to a real solution. 1 corresponds to an unreal solution.

the process of recovering the events with unusable solutions is seen in Section 5.3

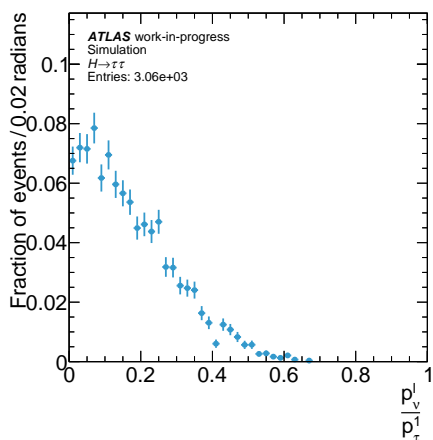
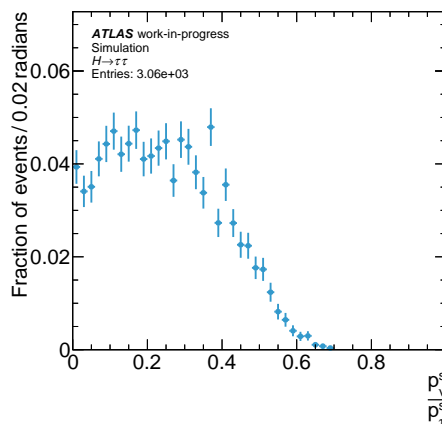
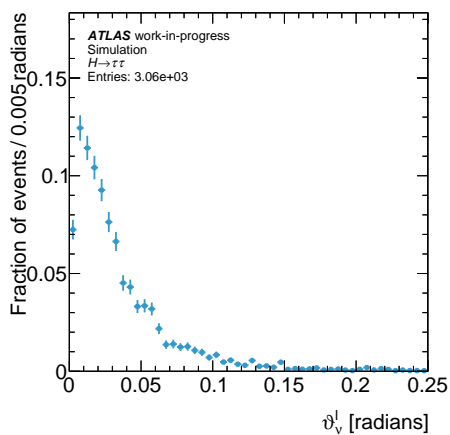
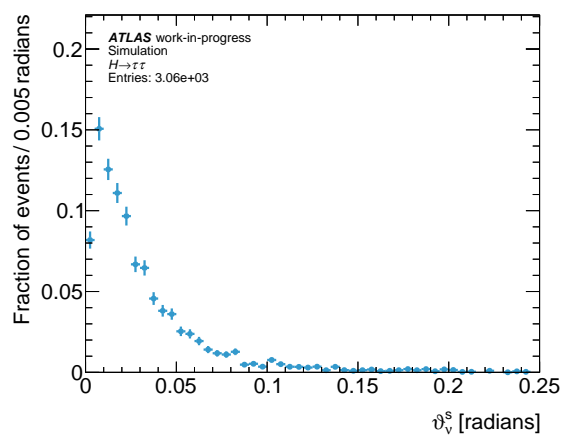
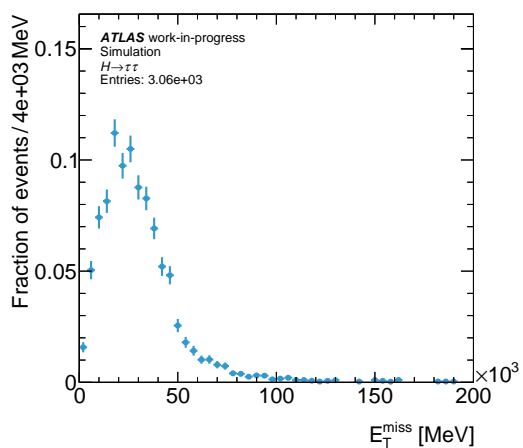
An initial goal of this study was to use the error of each individual event to constrain the PDFs introduced in Section 5.2.4. However, the solution seen in Appendix A.2 proved more complicated than originally expected and an adequate method for propagating the errors from vertex positions to \mathbf{P}_τ solutions was ultimately not found. This remains an avenue of further improvement in the future and the alternative method which was instead used is detailed in Section 5.2.4.

5.2.3 Ambiguity in the P_τ Solution

From Equation 5.2, it can be seen that every term is squared. This leads to a mathematical ambiguity in the solutions which arise. A more detailed look into this ambiguity, along with a physical explanation, can be found in Section 6.2. Initially, to perform the checks and tests in this chapter, the correct solution was chosen as the solution closest to the true solution. While this is quite effective for simulated data where the true solution is known, it is not a viable long-term solution. Therefore a method to either guess the correct solution or to consider both separately is required.

5.2.4 Event-by-Event PDFs

The solution to P_τ which has been determined using the methods discussed in the earlier sections of this chapter, must now be introduced to the MMC. Analogous to the already present PDFs, 5 variables calculated from the \mathbf{P}_τ are chosen. These are defined as missing transverse energy, E_T^{miss} , the angle between the neutrino and visible tracks for each τ , ϑ_ν^l and ϑ_ν^s , and the ratio of neutrino momentum to tau momentum for each τ , $\frac{p_\nu^l}{p_\tau^l}$ and $\frac{p_\nu^s}{p_\tau^s}$. These are discussed in more detail in Section 6.1. It is important to note that these PDFs are the additions to the MMC and the way in which the vertex-based calculations influence the final mass reconstruction of ditau events. However, this chapter focuses mainly on the accuracy of the P_τ determination from which these values are calculated. Figures 5.12(e), 5.12(a), 5.12(b), 5.12(c), and 5.12(d) show the distributions of these values determined from the true values from simulation. These are the goal distributions for which the vertex-based solutions


 (a) $\frac{p_v^l}{p_\tau^l}$ distribution from true simulation data.

 (b) $\frac{p_v^s}{p_\tau^s}$ distribution from true simulation data.

 (c) ϑ_v^l distribution from true simulation data.

 (d) ϑ_v^s distribution from true simulation data.

 (e) E_T^{miss} distribution from true simulation data.

are aiming.

5.3 Solving the NAN Value Problem

As mentioned in Section 5.2.2, a large portion of events have unusable values. This arises from a term underneath a square root in the solution. For every true event this term is positive. However for the reconstructed events, this term can become negative, due to the uncertainties in vertex determination. This term henceforth will be called the NAN term as it causes NAN return values when negative. There exists two such NAN terms for every $H \rightarrow \tau\tau$ event, one for each associated τ . It only takes one of the two NAN terms to be negative, for the solution to be unusable. This section will discuss the process used to find a useable solution for these events. The sections follow in order with increasing complexity the evolution of the process. The complete steps for this are summarized in Figure 5.13 and this figure is referred to in each of the following sections.

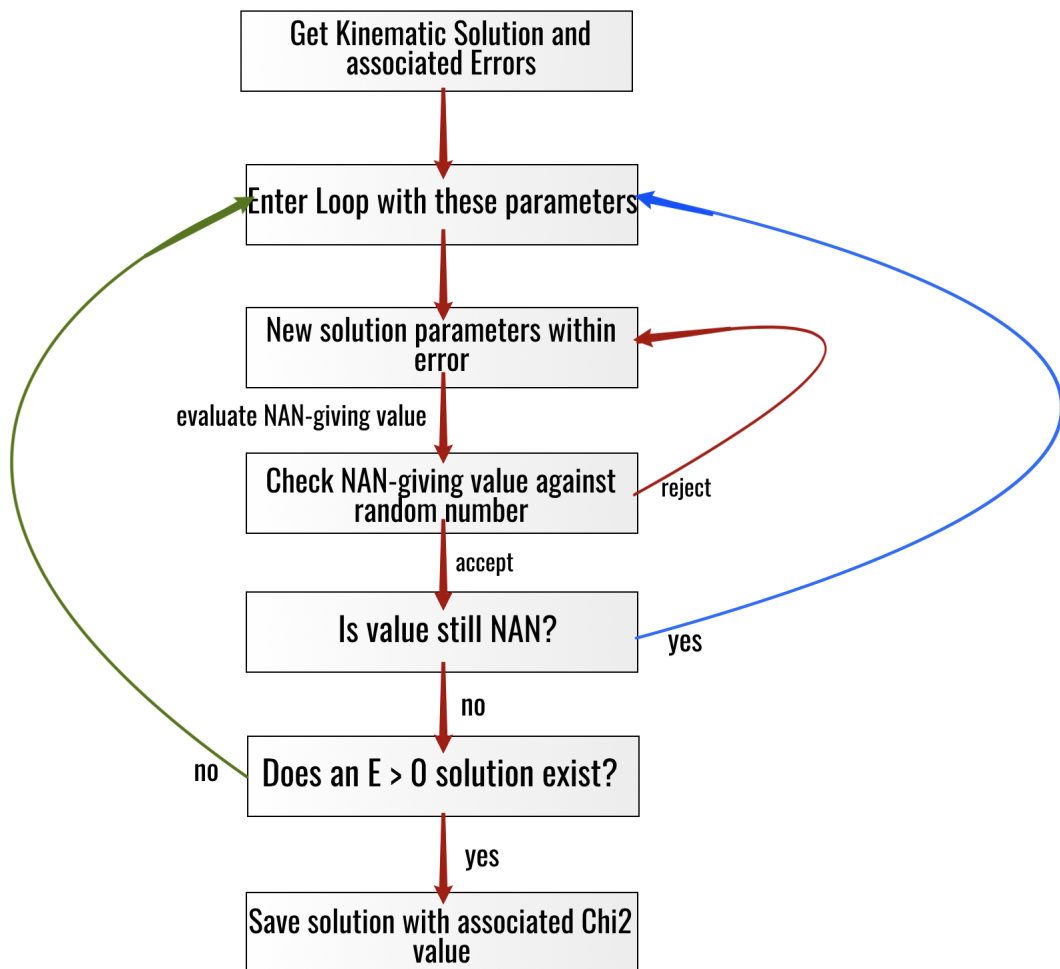


Figure 5.13: A brief summary of the Steps used to find a useable P_τ solution.

5.3.1 Random Walk

Section 5.1 shows the error on each of the vertices used in this study. From these it can be seen how close the real position likely is, given a reconstructed vertex position. When taking the reconstructed vertex solution and moving it around inside a boundary defined by these error distributions, eventually either the true solution or a useable solution can be found. Thus a 9-dimensional random walk was created to do exactly this. First, a boundary is set for each dimension using:

$$\pm B_{x_i} = x_i \pm 2(\sigma_{x_i}) \quad (5.8)$$

and a step size is set using:

$$s_{x_i} = 0.1(\sigma_{x_i}). \quad (5.9)$$

$\pm B_{x_i}$ represents the upper and lower boundaries, for each of the 9 vertex positions, x_i and s_{x_i} is the associated step size. The walk is allowed to iterate within the boundary, updating each position separately by the defined step size randomly forward or backward. This process is represented in the first 3 steps of Figure 5.13. What was determined from this, is that a large range of solutions will return a negative NAN term for several events. The problem of NAN values was reduced but with a large number of iterations of the random walk. The useable solutions which were found through the random walk were also often farther from the real solution than the initial trial. This resulted in the MMC failing to reconstruct a reasonable Higgs Boson mass. Therefore a further development was needed.

5.3.2 Metropolis Hastings Algorithm

As discussed in Section 4.1.2, the Metropolis Hastings (MH) Algorithm is used to randomly sample items from a distribution. The MH steps used here are summarized in steps four and five in Figure 5.13. The current iteration process to correct for the negative NAN term is the random walk, and although the borders and step sizes are defined using the errors from vertexing, the sampling is not representative of the spread of errors. There is also no method in place to keep the walk from producing solutions which are worse than the initial solution. Therefore the introduction of an MH algorithm is used to help with these problems. The driving term of this algorithm is the NAN term. The initial stepping is similar to the random walk; the original solution is moved around within the same boundaries, $\pm B_{x_i}$ and using the same step size, s_{x_i} . This time however, every step is evaluated based on the recalculation of the NAN term. An acceptance term is determined:

$$\exp\{NAN_{new} - NAN_{old}\} > U[0, 1] \quad (5.10)$$

where NAN_{new} is the lower of the two NAN terms and NAN_{old} is the lowest NAN term from the initial solution (or from the last accepted solution in the loop), and $U[0, 1]$ is a random number between 0 and 1. Since a negative NAN term is what creates the unusable solutions, a new position which creates a less negative NAN term is automatically accepted. However, when a new NAN term is more negative, the probability of accepting the new position is scaled with the difference between the values.

To summarize the algorithm so far, the solution from the kinematic reconstruction is used as a starting point. When that solution is unusable because of a negative NAN term, then every vertex position x_i is moved within the boundaries $\pm B_{x_i}$ by a step size of s_{x_i} . The NAN terms for each τ is calculated and the lowest one is chosen to compare against the original NAN term in Equation

5.10. When the new position is rejected, the initial starting point is used again to step randomly and get new vertex positions. This repeats until a new position is accepted. This new accepted position is then evaluated. When the NAN term is still negative, the accepted position becomes the starting position. The boundaries are updated, and a step is taken for each vertex position. This continues until a position is accepted which has positive NAN terms.

With these steps applied, there were no longer any events which created NAN values. One avenue of worsening solutions which was present in the random walk is now alleviated. The solutions would not gradually get worse by creating lower and lower NAN terms, leading to still unusable solutions after several iterations. However, this alone is not complete. There are still several solutions which were far from the true solutions and the MMC was not able to create a viable Higgs mass with the addition of PDFs for these events.

5.3.3 Uncorrelated χ^2 Driven MH

As seen in Section 5.1, the uncertainties in the vertex positions roughly follow a gaussian distribution. Therefore when converting the NAN-giving solutions to real solutions by moving the vertex positions, it is import to give greater weight to the iterations which are closer to the initial positions. Therefore a χ^2 value is calculated for each proposed step in the MH algorithm

$$\chi^2(\alpha) = \sum_{i,j=1}^9 (x_i - \mu_i)(V^{-1})_{ij}(x_j - \mu_j). \quad (5.11)$$

Here, i moves through each of the 9 vertex position variables, x_i and x_j represent the new solution positions, μ_i and μ_j represent the initial positions from the kinematic solution, and V is the covariance matrix. V is a 9×9 matrix with three 3×3 matrices on the diagonal corresponding to the covariance matrix for each vertex. It was assumed that there was no correlation between the position measurements of different vertices. This χ^2 is a weighted measure of how far away the new position is from the old.

Subtracting the χ^2 term makes the new NAN term more negative. As discussed earlier, the lower a new NAN value is, the less likely it is to be accepted. Using this method, as the new parameters get farther away from the starting parameters, the χ^2 gets larger and the NAN term minus the χ^2 term lowers. The NAN term is a value typically on the order of $10^{20} - 10^{22}$ whereas the χ^2 term is typically on the order of $10^{-1} - 10^0$. Therefore, it is naturally too low to affect the NAN term. A small study of scaling was done to determine how large one should make the χ^2 term so that it has the desired effect. When it is scaled too high, it is very unlikely that any solution should pass. When it is too low, it has no effect on the acceptance. The values which were considered for subtracting from NAN_{new} were

$$-0.1(NAN_{old})(\chi^2), \quad (5.12)$$

$$-0.2(NAN_{old})(\chi^2), \quad (5.13)$$

$$-0.5(NAN_{old})(\chi^2), \quad (5.14)$$

$$-0.1(NAN_{new})(\chi^2). \quad (5.15)$$

The scaling parameters were evaluated based on how often a solution was found and how often the solution found was viable. Since the χ^2 value is on the order of $10^{-1} - 10^0$, using Equation 5.14 was too high and new parameters were rarely accepted, leading to still negative NAN values. After

comparing Equations 5.12 and 5.13, it was found that the former was slightly better. To see if a sliding parameter which adjusted to every set of new parameters tested would work better, Equation 5.15 was tested, but it was found that this had no effect on the outcome as opposed to using no scaling. Further studies may be done to optimize this parameter in the future.

The scaling parameter which is now implemented (Equation 5.12) is successful in constraining the solution. However, there was an increase in the number of events for which no viable solution was found. There could be a few reasons for this, one which was thought to be likely is the presence of a local maximum (in terms of the NAN term). In this case the MH algorithm could become stuck, without the possibility of moving to a better solution.

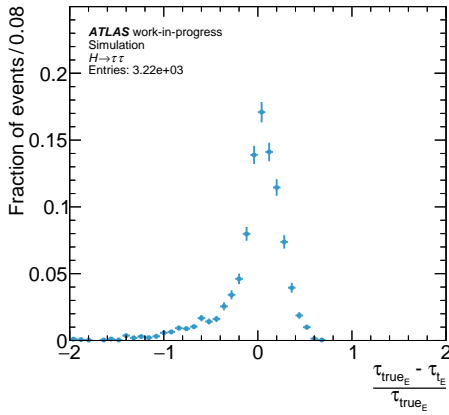
5.3.4 Seeding the MH

The last step which is added to the entire process will be added at the beginning. In order to get around the possibility of a local maximum, or another problem which could be related to the starting parameters, a small loop is created around the entire MH algorithm. This will allow the MH algorithm to run several times for different starting parameters. The initial vertex positions will be taken one step away according to the Random Walk Method described in Section 5.3.1. In this way, ditau event will seed the MH algorithm several times with slightly different perturbations.

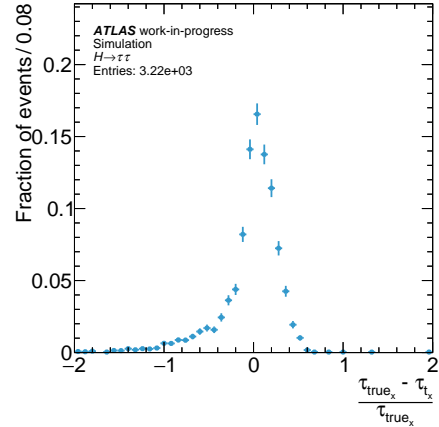
Now the complete process can be seen in its entirety. In Figure 5.13, step 1 remains the same. steps 2-6 are the MH algorithm with a few specific qualifications related to this task. These steps are repeated for a set number of iterations where each starting parameter is one step away from the original vertex position. For every successful run of the MH algorithm, step 7 occurs where the un-scaled χ^2 is saved with the associated new vertex positions. The successful MH run with the associated lowest χ^2 is then used as the solution for \mathbf{P}_τ . Using initially 75 loops where the initial starting parameters are changed (steps 2-7 repeated) and 10^7 iterations of the MH algorithm (steps 2-5), almost all events returned non-NAN values and the MMC was able to reconstruct a Higgs mass for these events.

After the addition of the MH algorithm, the resolutions of the P_τ components did not change much as seen in Figures 5.14(a), 5.14(b), 5.14(c), and 5.14(d) (compare to Figures 5.8(a), 5.8(b), 5.8(c), and 5.8(d)). The distributions were slightly more spread with a small shift towards the origin. The shift became $\approx 5\%$ (from $\approx 8\%$) and the spread $\approx 19\%$ (from $\approx 17\%$). This shows that there is still much improvement in order to take the solutions from reconstructed vertices closer to the accuracy of the solutions derived from the true vertices.

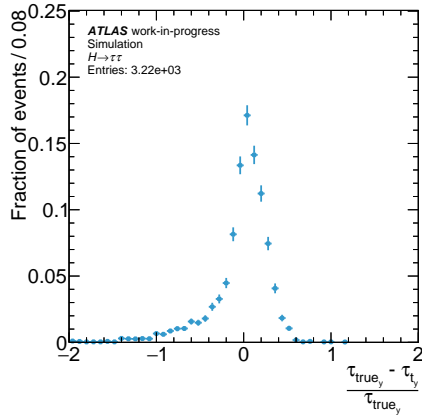
In addition to the above mentioned processes, a test of the total loops and MH iterations was conducted. The loops ranged from 50-100 while the MH iterations ranged from 10^6 - 10^8 . The intention was to see if larger iterations would produce more accurate results. However when very little change occurred, the result might indicate that the number of iterations is already sufficient to be representative of the solution space, or that the choice of conditional density is poor (see Section 4.1.2). Further studies into the parameters of the MH implemented here could be undertaken. The results of the scan as they affected the total Higgs Mass reconstruction can be seen in Appendix A.3. The best performing of the combinations was found to be 75 loops with 10^7 MH iterations. Figure 5.15 shows the ditau mass reconstruction before the application of weighting (discussed in Chapter 6). The scans given in Appendix A.3 have truth weighting applied and will be further discussed in the next chapter.



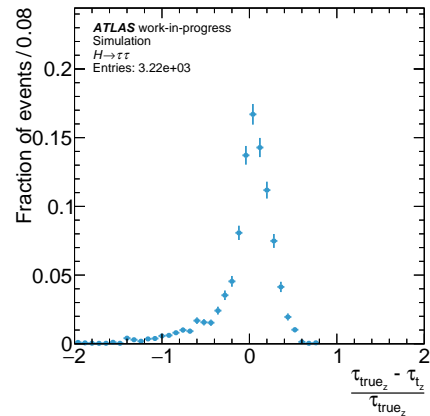
(a) Difference in true and reconstructed P_{τ_0} as a percentage of the true value.



(b) Difference in true and reconstructed P_{τ_1} as a percentage of the true value.



(c) Difference in true and reconstructed P_{τ_2} as a percentage of the true value.



(d) Difference in true and reconstructed P_{τ_3} as a percentage of the true value.

5.4 Future Possibilities

The methods described above complete an investigation into the addition of vertex information into the MMC. The unexpected complexity of the solution, made the intended event specific error propagation to the event PDFs unavailable. Future studies may be done on either adding error propagation methods which could show an improvement in the portion of events whose error correlates with a smaller resolution than the entire ensemble resolution. It was also found that the errors in vertex reconstruction led to several events which returned unreal solutions. The mathematical cause for this in the vertex-based reconstruction solution is determined, however future work to either improve the method for recovering these solutions, or to increase the precision of vertex reconstruction could lead to improvement of the ditau mass calculations. This is evidenced by the accuracy with which the derived equation for solving the kinematics reproduces the true simulated data when using truth information.

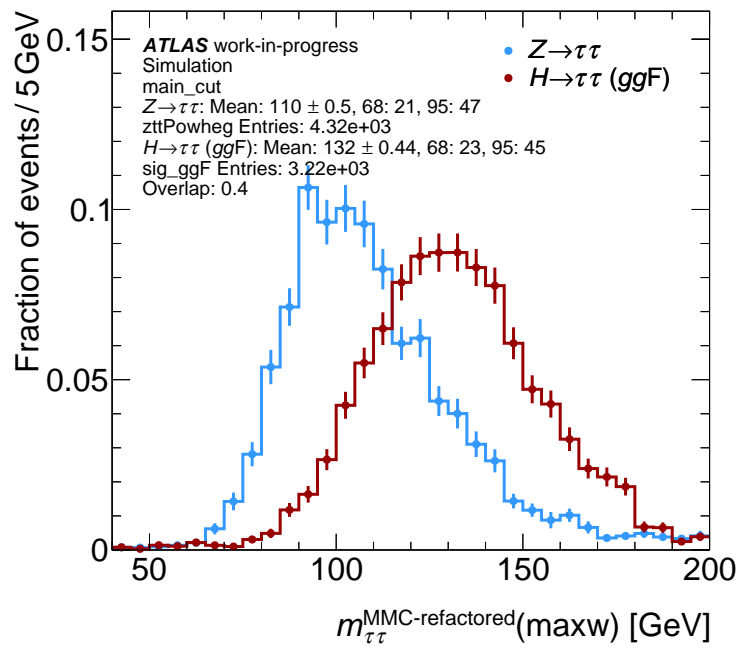


Figure 5.15: Higgs and Z boson mass estimates from the τ reconstruction of ditau $3p0n$ events after adding truth weighted PDFs.

Optimization and Parametrisation of τ Solutions

As mentioned in Section 5.2.3, the solution to \mathbf{P}_τ shown in Appendix A.2 has an ambiguity. Two separate solutions exist for each \mathbf{P}_τ . In order to accurately predict which solution is correct, a study was performed and the results are presented in this chapter. The ambiguity which is present is not unknown to other τ reconstruction methods. The MMC also has an ambiguity present and the methods within this chapter may be applied to any such ambiguity, although here it is applied to the one arising from the vertex-based reconstruction. With the completion of the methods mentioned in Chapter 5, the individual event PDFs will be examined closer (Section 6.1) and used as a basis for evaluating the performance of solution weighting. (Section 6.2) Further the predictive ability of the solution energies both directly and as relative proportions to predict the correct solution are examined in Section 6.3. The results of the methods in both Chapters 5 and 6 are summarized in the final section (Section 6.4).

6.1 Event by Event PDF Generation

In order to impact the Higgs mass reconstruction in the MMC, a series of new PDFs are calculated for each event based on 5 variables. Each of the 5 variables, E_T^{miss} , ϑ_ν^l , ϑ_ν^s , $\frac{p_\nu^l}{p_\tau^l}$, $\frac{p_\nu^s}{p_\tau^s}$, are determined directly from the \mathbf{P}_τ solutions calculated in Chapter 5. E_T^{miss} was determined for each τ separately and then added together for the total E_T^{miss}

$$E_T^{miss,j} = \sqrt{(p_{\nu_1}^j)^2 + (p_{\nu_2}^j)^2} \quad (6.1)$$

$$E_T^{miss} = \sum_{j=l,s} E_T^{miss,j}. \quad (6.2)$$

The angle between the ν and combined visible tracks was determined using:

$$\vartheta_\nu^j = \cos^{-1} \left(\frac{p_\nu^j \cdot p_{vis}^j}{\|p_\nu^j\| \|p_{vis}^j\|} \right). \quad (6.3)$$

Finally the ratio of momentums are calculated as:

$$\frac{p_v^j}{p_\tau^j} = \frac{\|\mathbf{p}_v^j\|}{\|\mathbf{p}_\tau^j\|}. \quad (6.4)$$

For every τ there are two solutions for \mathbf{P}_τ . Therefore each quantity associated with a single τ also has two solutions, and the one quantity, E_T^{miss} which is associated with both τ s in an $H \rightarrow \tau\tau$ event has 4 solutions.

6.1.1 Choice of Distribution Variables

The two solutions for each quantity above were used for the generation of a PDF. This was done by using the solution as the center of a gaussian distribution

$$P(x) = (1 - r) \left(N_1 \exp \left\{ \frac{-1}{2} \left(\frac{x - \mu_1}{\sigma_{\mu_1}} \right)^2 \right\} \right) + (r) \left(N_2 \exp \left\{ \frac{-1}{2} \left(\frac{x - \mu_2}{\sigma_{\mu_2}} \right)^2 \right\} \right). \quad (6.5)$$

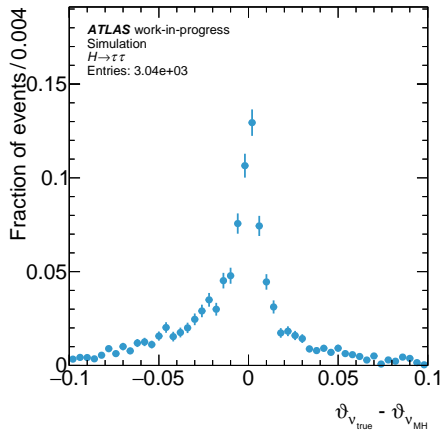
Here, r is called the skew parameter and initially set to 0.5. N_i is the normalization parameter, however the equation as a whole is normalized so it was set as:

$$N_i = \begin{cases} 1 & \text{for real solutions of } \mathbf{P}_\tau \\ 0 & \text{for unreal solutions of } \mathbf{P}_\tau \end{cases} \quad (6.6)$$

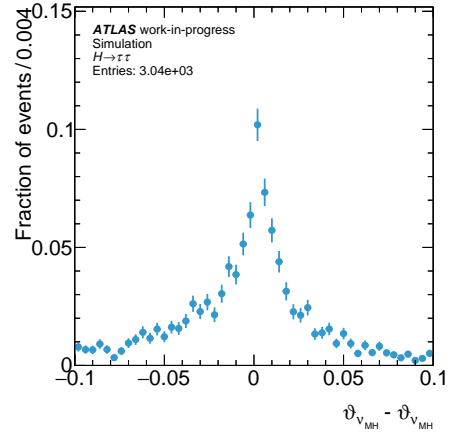
Where i corresponded to the two solutions for \mathbf{P}_τ and either solution or both solutions could be unreal by having a NAN value or $P_{\tau_0} < 0$. μ_1 and μ_2 are the two solutions for each variable with their associated error σ_μ . The PDF for E_T^{miss} was different due to the presence of 4 solutions from 2 τ s

$$P(x) = (1 - r_1)(1 - r_2) \left(N_1 \exp \left\{ \frac{-1}{2} \left(\frac{x - \mu_1}{\sigma_\mu} \right)^2 \right\} \right) + (1 - r_1)(r_2) \left(N_2 \exp \left\{ \frac{-1}{2} \left(\frac{x - \mu_2}{\sigma_\mu} \right)^2 \right\} \right) + \\ (r_1)(1 - r_2) \left(N_3 \exp \left\{ \frac{-1}{2} \left(\frac{x - \mu_3}{\sigma_\mu} \right)^2 \right\} \right) + (r_1)(r_2) \left(N_4 \exp \left\{ \frac{-1}{2} \left(\frac{x - \mu_4}{\sigma_\mu} \right)^2 \right\} \right). \quad (6.7)$$

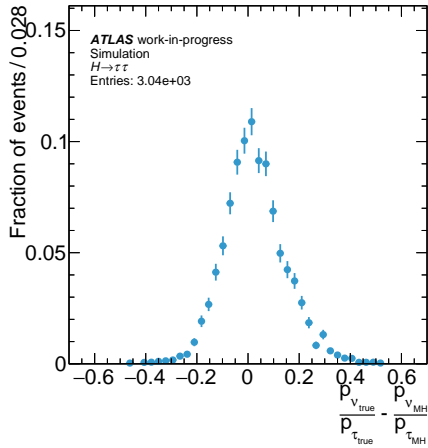
Since it was not possible to propagate the error directly for each event, an error defined by the entire ensemble of events was used. This was accomplished by determining the true value of each of the 5 quantities and subtracting the solutions obtained from the reconstructed information. To account for the double solution, the solution which was closest to the true solution was used in the error determination. The resulting distributions can be seen in Figures 6.1(a), 6.1(b), 6.1(c), 6.1(d), and 6.1(e). Each of these were fitted with a gaussian distribution and the widths were used as σ_μ values in Equation 6.5. The solutions which were used for the resolution are also seen in Figures 6.2(a), 6.2(b), 6.2(c), 6.2(d), and 6.2(e). These represent the best possible performance from the steps administered in Chapter 5. However future improvements to those methods would also improve the upper limit of performance. They can be visually compared to the true distributions shown in Section 5.2.4.



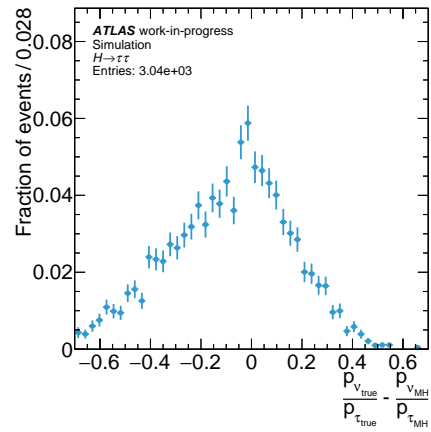
(a) Difference between the true and derived values for ϑ_V^l .



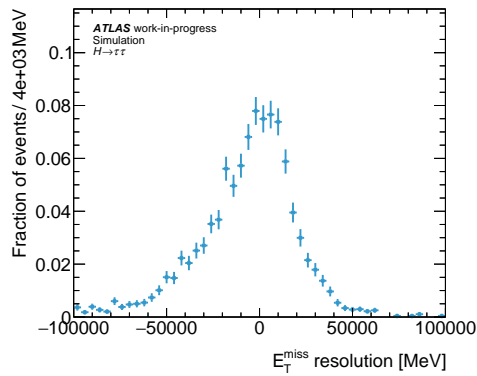
(b) Difference between the true and derived values for ϑ_V^s .



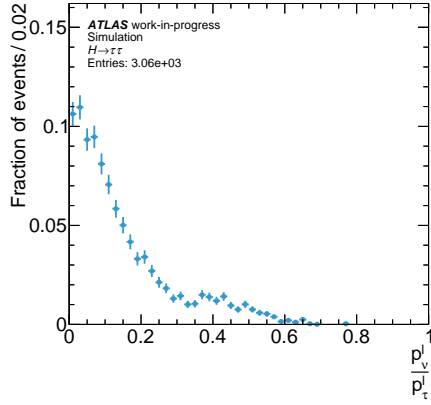
(c) Difference between the true and derived values for $\frac{p_V^l}{p_\tau^l}$.



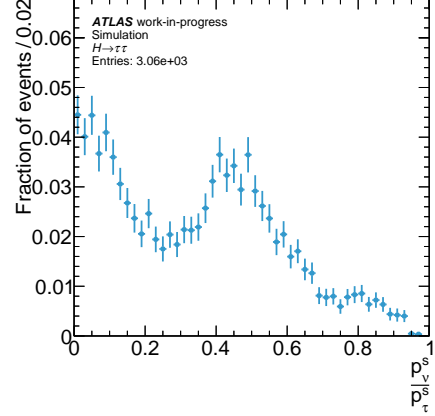
(d) Difference between the true and derived values for $\frac{p_V^s}{p_V^s}$.



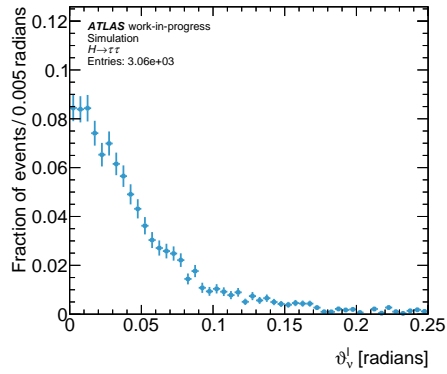
(e) Difference between the true and derived values for E_T^{miss} .



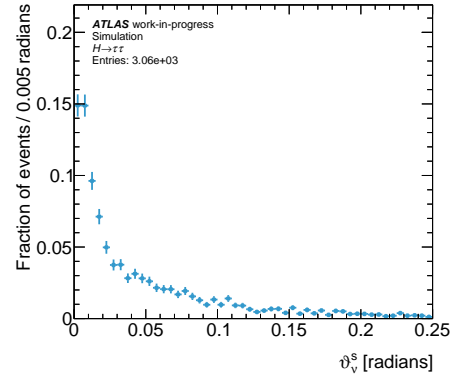
(a) $\frac{p_v^l}{p_\tau^l}$ distribution from upper limit on vertex-based solution.



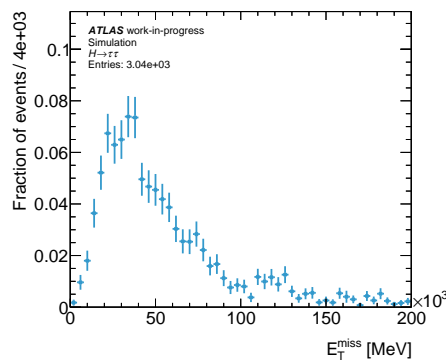
(b) $\frac{p_v^s}{p_\tau^s}$ distribution from upper limit on vertex-based solution



(c) ϑ_v^l distribution from upper limit on vertex-based solution



(d) ϑ_v^s distribution from upper limit on vertex-based solution

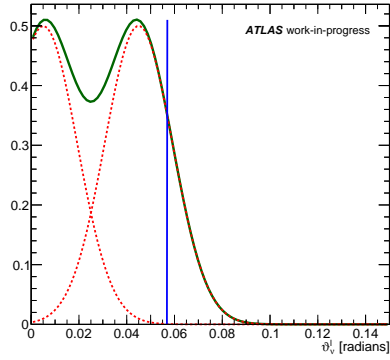


(e) E_T^{miss} distribution from upper limit on vertex-based solution.

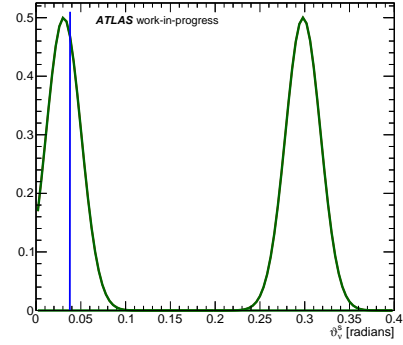
To show the effect of the work of this chapter, event number 1268363 from the simulated $H \rightarrow \tau\tau$ data was chosen. The PDFs with equally weighted solutions and widths corresponding to the aforementioned resolutions are shown in Figures 6.3(a), 6.3(b), 6.3(c), 6.3(d), and 6.3(e). In these event-by-event PDFs figures, the blue line is the true value, the green line is the combined PDF of the two solutions, and the dotted red line are the individual contributions from each solution. An ensemble spread of the distribution was also created. Here the two solutions from each problem were added with their associated weights (currently both are weighted equally). These can be seen in Figures 6.4(a), 6.4(b), 6.4(c), 6.4(d), and 6.4(e). A problem which arises from the solution ambiguity, is the large area of far away solutions which contain a similar probability. This can be seen in every generated PDF for event 1268363. ϑ_v^s shows a distribution where a wrong solution could be isolated far away from the true solution. Therefore the current PDFs with equally weighted solutions, does not have the capacity to improve the MMC and a search for more accurate weighting is needed.

6.2 Solving the Kinematic Ambiguity

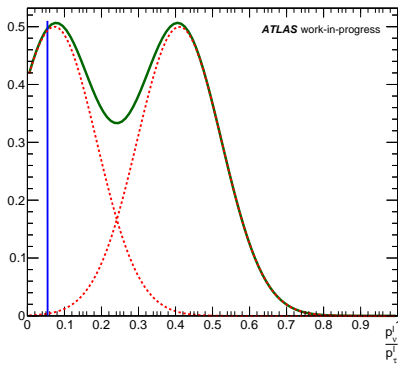
It is possible to consider both \mathbf{P}_τ solutions separately and see their individual results (This would result in 4 different MMC iterations for each $H \rightarrow \tau\tau$ event). It may also be possible to predict which solution is correct. The former idea has the disadvantage of long computation times, while the latter is limited to the accuracy of prediction. This chapter focuses on the latter. The difference in the solutions has a large range. This can be seen in Figures 6.5(a) and 6.5(b). For the leading τ most solutions have a difference which is over half the value of the low energy solution. The subleading τ has a higher number of solutions which are close together, but it also has a longer tail containing solutions far from each other. Because of this large difference, picking one solution over the other would influence the total ditau mass reconstruction. To look for variables which may be predictive of the correct solution (the solution which is closest to the true value), the truth information was again used in the same way as Section 5.2.1. It was determined that for $\approx 75\%$ of events, the lower energy leading τ solution is the correct solution (Figure 6.6(a)) and for $\approx 56\%$ of events, the lower energy subleading τ is the correct solution (Figure 6.6(b)). Using this information, each of the solutions will be given a weight after comparing their energies. Lower solutions will receive a weight of 75% (56% for subleading) and the higher solution will receive a weight of 25% (44% for subleading) through the skew variable, r in Equation 6.5. The result are 5 new PDF distributions for event 1268363 (Figures 6.7(a), 6.7(b), 6.7(c), 6.7(d), and 6.7(e)). This example event shows the advantage of the weighting. It can be seen that solutions close to the real solution have a higher probability than when previously weighted equally. However, it can also be seen that there is still a non-negligible probability for the wrong solutions. Furthermore, since the lower energy solution is usually the correct solution, it can be inferred that the final distribution would be skewed towards higher energies but possibly to a lesser degree after the weighting. The total distribution of solutions with this included weight is shown in Figures 6.8(a), 6.8(b), 6.8(c), 6.8(d), and 6.8(e). These can be compared with both the distributions containing only the closest solution (Section 6.1) and the actual distributions from the truth information (Section 5.2.4). The PDFs still are not optimal for inclusion in the MMC. When computing the complete ditau mass from the reconstructed τ s, both the Z and H are biased towards higher masses. This heavy shift towards higher masses is unexpected. When the PDF from the individual event has a wider spread than the PDFs present in the MMC, it would be expected that the MMC PDFs would dominate. However, it is possible that the influence of the second wrong solution which is included in the PDF



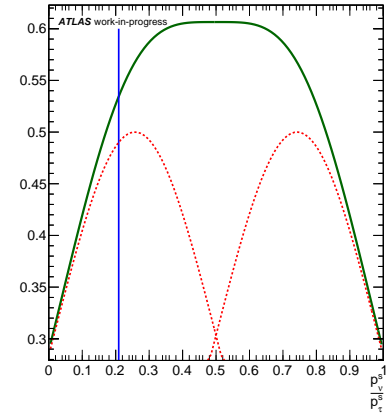
(a) ϑ_v^l PDF for event number 1268363.



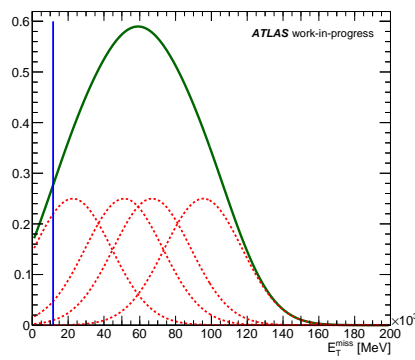
(b) ϑ_v^s PDF for event number 1268363.



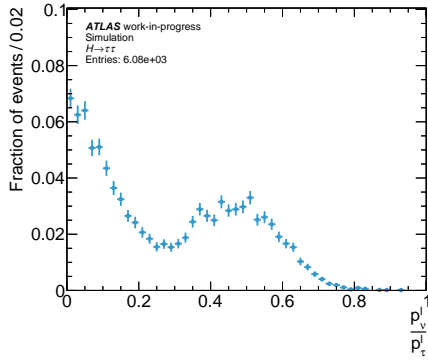
(c) $\frac{p_v^l}{p_\tau}$ PDF for event number 1268363.



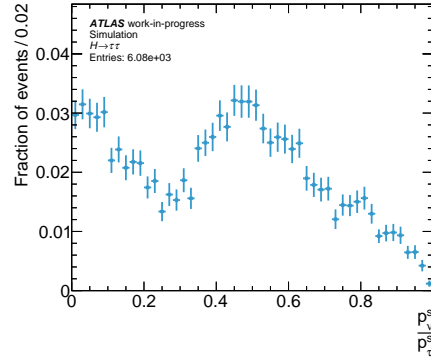
(d) $\frac{p_v^s}{p_\tau}$ for event number 1268363.



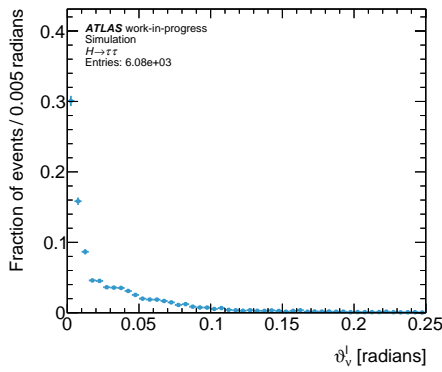
(e) E_T^{miss} PDF for event number 1268363.



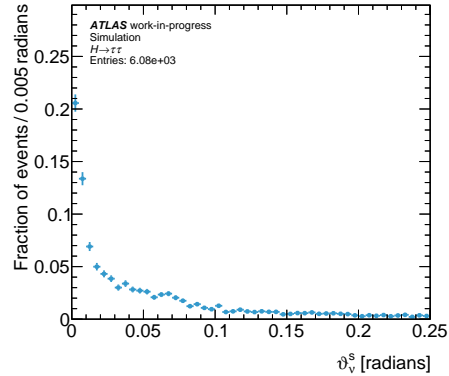
(a) $\frac{p_v^j}{p_\tau^j}$ distribution from equally weighted vertex-based solutions.



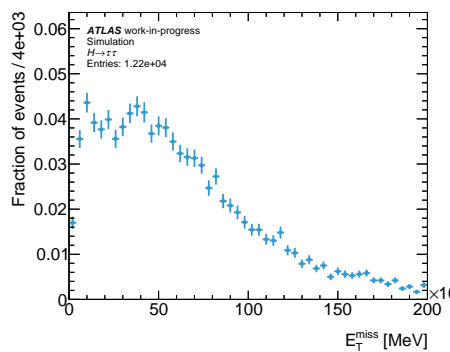
(b) $\frac{p_v^s}{p_\tau^s}$ distribution from equally weighted vertex-based solutions.



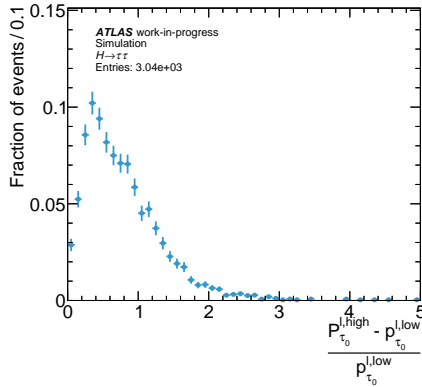
(c) ϑ_v^j distribution from equally weighted vertex-based solutions.



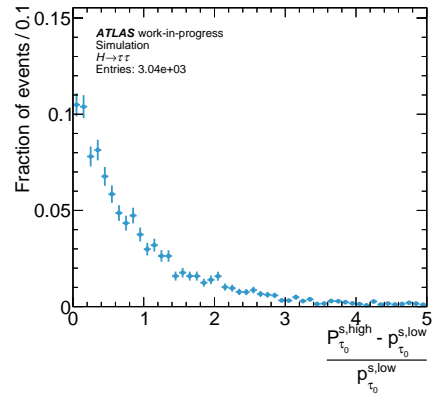
(d) ϑ_v^s distribution from equally weighted vertex-based solutions.



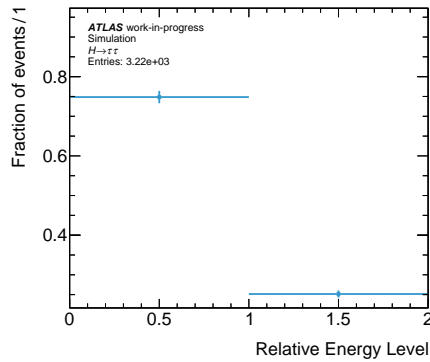
(e) E_T^{miss} distribution from equally weighted vertex-based solutions.



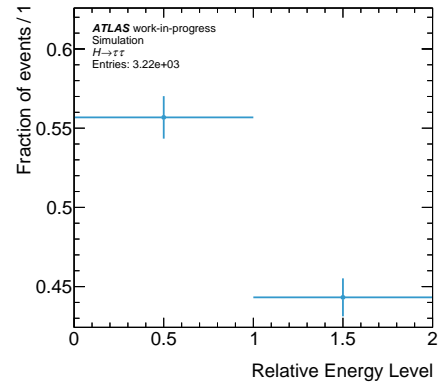
(a) The distribution of differences in $P_{\tau_0}^l$ as a portion of the lower $P_{\tau_0}^l$ value.



(b) The distribution of differences in $P_{\tau_0}^s$ as a portion of the lower $P_{\tau_0}^s$ value.



(a) Percentage of events where the low energy leading tau solution is correct.

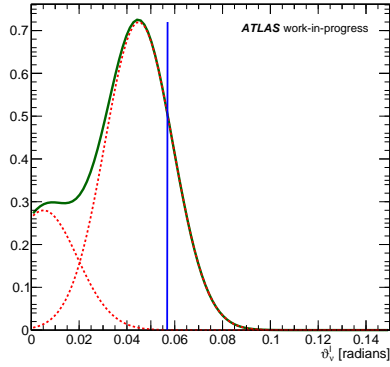


(b) Percentage of events where the low energy subleading tau solution is correct.

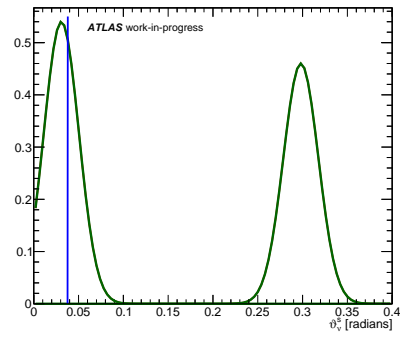
has a stronger pull on the outcome than expected. Therefore further studies to predict the correct solution follow in the next section.

6.3 Further Parametrisation of Solutions

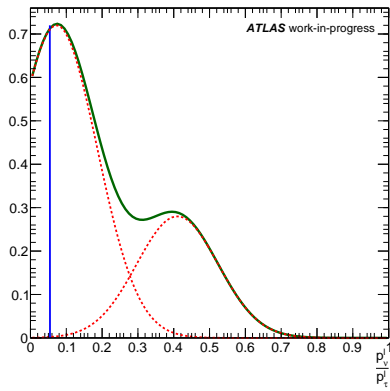
The initial selection for weighting the solutions came from the truth information. This shows that in the best scenario, the solutions can be predicted by their relative energy to $\approx 75\%$. However, when analyzing again using the reconstructed data instead of the truth data, the distribution changes. Figures 6.9(a) and 6.9(b) show how often the lower energy solution was closest to the truth value. Further, the distribution of solution differences, allows for a possible means of parametrisation. As two solutions get farther apart, the amount of high mass bias which can enter the solution increases. Therefore, it is important to also look at the predictive ability of relative energy at different energy differences. So a



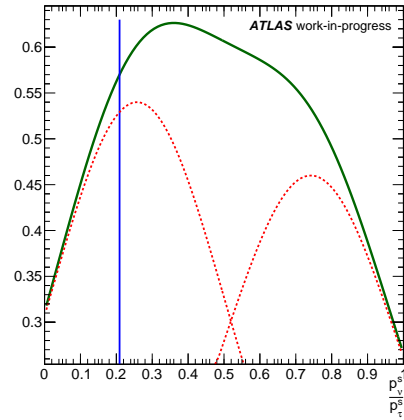
(a) ϑ_v^l PDF for event number 1268363



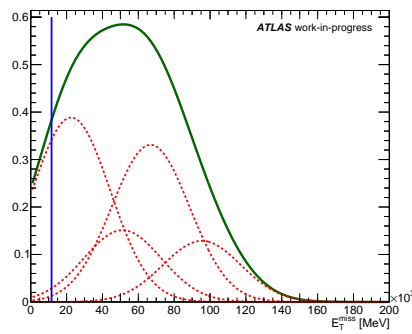
(b) ϑ_v^s PDF for event number 1268363



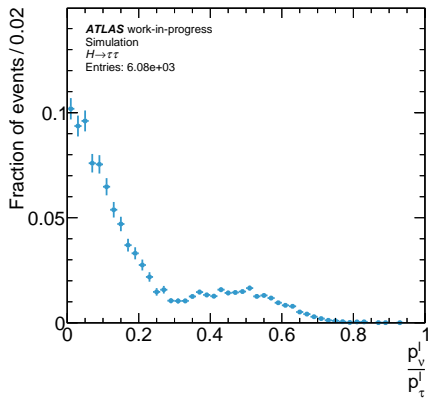
(c) $\frac{p_{\nu}^l}{p_{\tau}}$ PDF for event number 1268363.



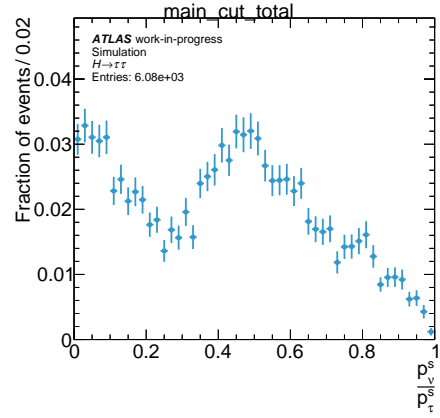
(d) $\frac{p_{\nu}^s}{p_{\tau}}$ for event number 1268363.



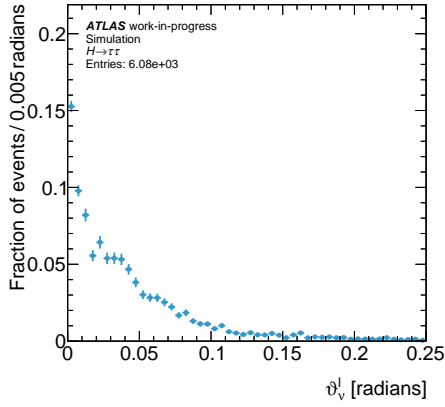
(e) E_T^{miss} PDF for event number 1268363.



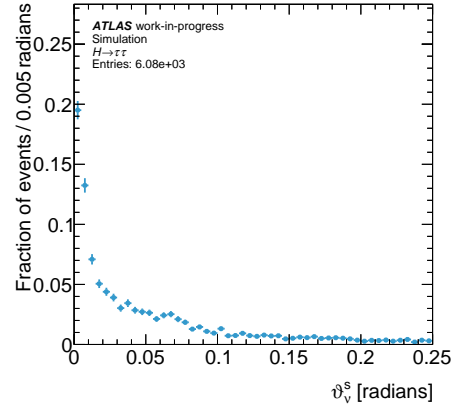
(a) $\frac{p_v^l}{p_\tau^l}$ distribution from globally-weighted vertex-based solutions.



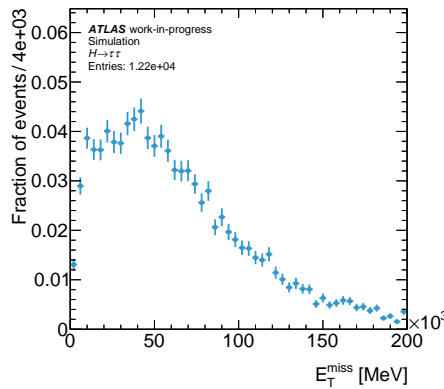
(b) $\frac{p_v^s}{p_\tau^s}$ distribution from globally-weighted vertex-based solutions.



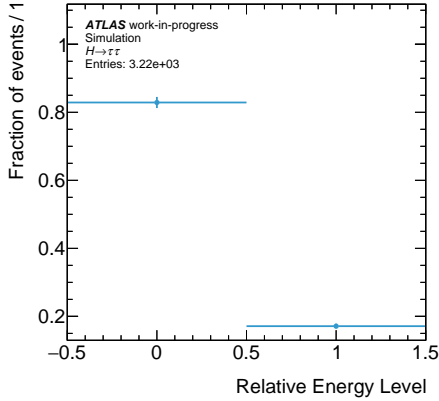
(c) ϑ_v^l distribution from globally-weighted vertex-based solutions.



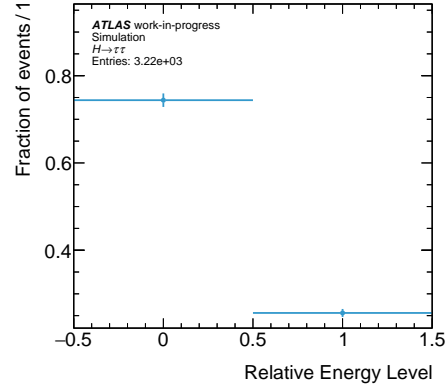
(d) ϑ_v^s distribution from globally-weighted vertex-based solutions.



(e) E_T^{miss} distribution from globally-weighted vertex-based solutions.



(a) Percentage of events where the low energy leading tau solution is correct for reconstructed events.



(b) Percentage of events where the low energy subleading tau solution is correct for reconstructed events.

Distribution of Low Energy Bias in quantiles of ν

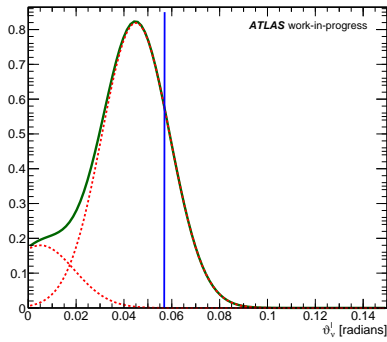
range of ν	Low Solution Bias	Number of Events
0.000 - 0.294	70%	508
0.294 - 0.469	78%	521
0.469 - 0.637	80%	460
0.637 - 0.812	84%	405
0.812 - 1.007	90%	378
1.007 - 1.239	90%	309
1.239 - 1.559	93%	256
1.559 - 2.088	95%	187
2.088 - 3.080	98%	61
3.080 - inf	100%	17

Table 6.1: Distribution of low energy solution bias in quantiles of ν for the leading τ .

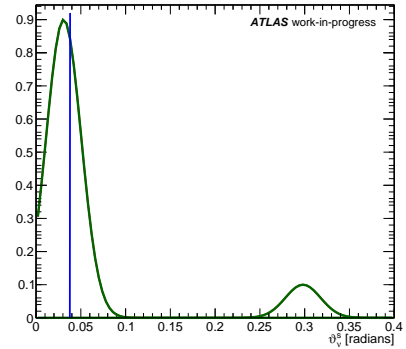
parametrising variable was defined

$$\nu = \frac{P_{\tau_0}^{high} - P_{\tau_0}^{low}}{P_{\tau_0}^{low}}. \quad (6.8)$$

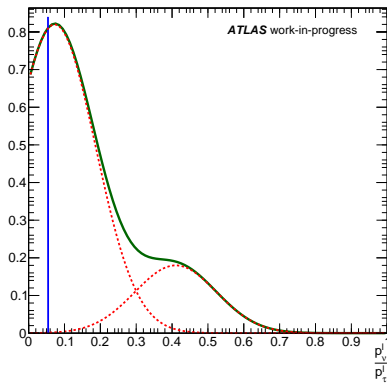
The solutions were grouped in quantiles based on this parameter and evaluated on how often a lower energy solution was closest to the true solution. Tables A.10(a), A.10(b) show the distribution of low energy solutions being correct in ranges of the variable ν defined above with the respective number of events in each range. It can now be seen that as the solutions get further apart, it is easier to predict the solution which is closest to the real solution. For the leading τ , the bias is steadily increasing. For the subleading τ , the bias follows the increasing pattern at a value of $\nu > 0.4$. Using this, each event is parameterised and the skew variables are changed to fit the difference in energies. This makes the PDFs for event number 1268363 change to Figures 6.10(a), 6.10(b), 6.10(c), 6.10(d), and 6.10(e). Here it can be seen that the PDFs are further improved to have higher probabilities closer to the true solution. The overall distributions (Figures 6.11(a), 6.11(b), 6.11(c), 6.11(d), and 6.11(e)) are also



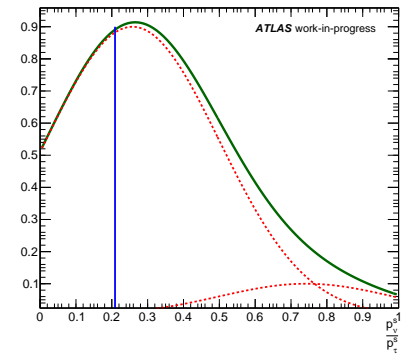
(a) ϑ_v^l PDF for event number 1268363.



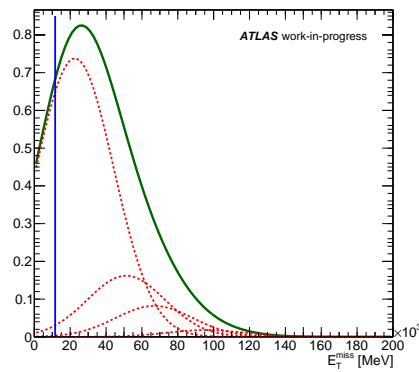
(b) ϑ_v^s PDF for event number 1268363.



(c) $\frac{p_v^l}{p_\tau}$ PDF for event number 1268363.



(d) $\frac{p_v^s}{p_\tau}$ PDF for event number 1268363.



(e) E_T^{miss} PDF for event number 1268363.

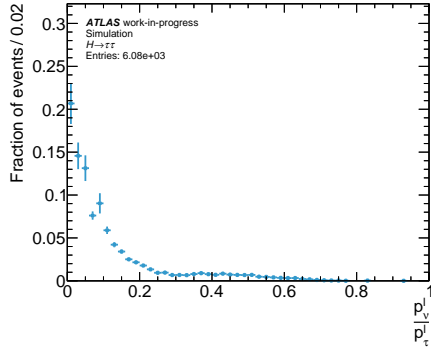
Distribution of Low Energy Bias in quantiles of ν		
range of ν	Low Solution Bias	Number of Events
0.000 - 0.031	71%	135
0.031 - 0.063	61%	90
0.063 - 0.095	47%	108
0.095 - 0.225	59%	383
0.225 - 0.404	63%	450
0.404 - 0.628	70%	411
0.628 - 0.927	75%	410
0.927 - 1.390	77%	395
1.390 - 2.250	90%	378
2.250 - inf	94%	280

Table 6.2: Distribution of low energy solution bias in quantiles of ν for the subleading τ .

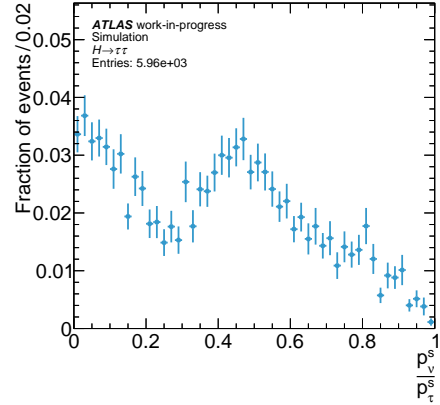
again shifted in the direction of the true distribution. However it can be seen that this distribution has still not reached the upper limit (Figures 6.2(a), 6.2(b), 6.2(c), 6.2(d), 6.2(e)).

6.4 Final Results

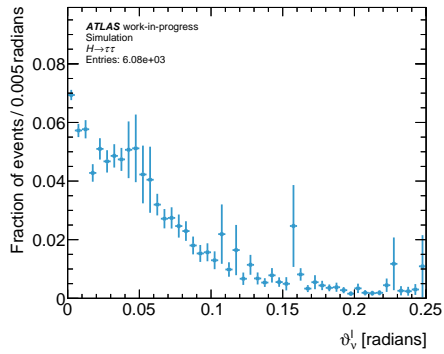
Since changing the amount of loops and MH iterations changes also the distribution of \mathbf{P}_τ solutions, the process of comparing different combinations of these were repeated (see Section 5.3.4). Using the parametrisation method described in the previous section, each combination was given its unique parametrisation and the final solutions were compared. The differences between these again were minimal, but the reconstruction of the Higgs mass was slightly better. The resulting plots can be seen in Appendix A.5. Also the associated tables for the parametrisations used can be found in Appendix A.4. There it can be seen that the same trend of increasing predictability with increasing relative difference in energies is continued. The mass reconstruction for the parent H or Z particle from the daughter τ s within the cuts implemented in this thesis can be seen in Figure 6.12. This figure represents the MMC before the addition of the event-by-event PDFs described in this thesis. Before the NAN problem was solved in Chapter 5, the amount of events which passed was quite small, and therefore a mass reconstruction was not attempted until the solutions were recovered. Once the solutions were recovered, the initial weighting determined from the truth was added to the PDFs and the masses were again reconstructed (Figure 6.13). When comparing to the MMC before the addition, it can be seen that the mass estimates are shifted to much larger masses. The spread of the estimates also increases, decreasing the MMC ability to differentiate $H \rightarrow \tau\tau$ from the background $Z \rightarrow \tau\tau$. After the further attempt to improve the added PDFs using parametrisation of the variable ν (Section 6.3) the resulting mass reconstruction can be seen in Figure 6.14. Again it can be seen that the mass estimates remain large. The difference in the mass reconstruction is minimal when between the global weight and parametrising.



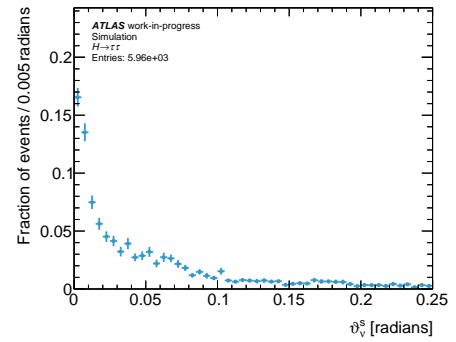
(a) $\frac{p_V^l}{p_\tau^l}$ distribution from parametrised vertex-based solutions.



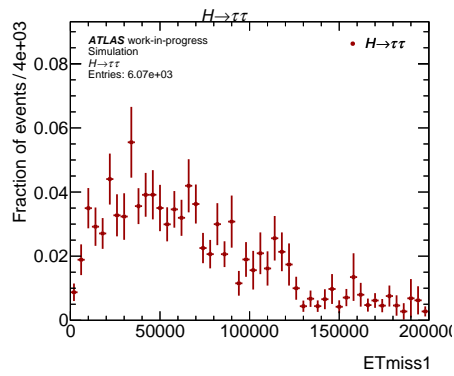
(b) $\frac{p_V^s}{p_\tau^s}$ distribution from parametrised vertex-based solutions.



(c) ϑ_V^l distribution from parametrised vertex-based solutions.



(d) ϑ_V^s distribution from parametrised vertex-based solutions.



(e) E_T^{miss} distribution from parametrised vertex-based solutions.

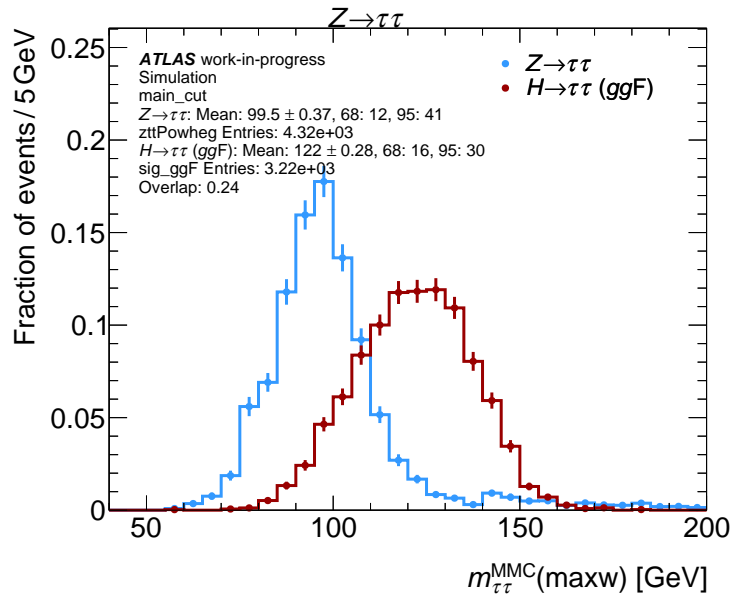


Figure 6.12: Higgs and Z boson mass estimates from the ditau mass reconstruction of double $3p0n$ events in the initial MMC.

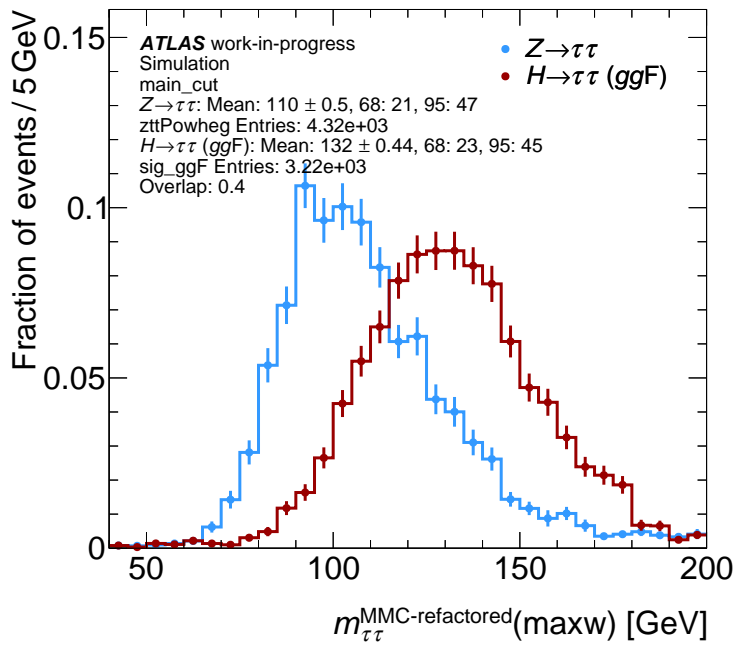


Figure 6.13: Higgs and Z boson mass estimates from the ditau mass reconstruction of double $3p0n$ events after adding truth weighted PDFs.

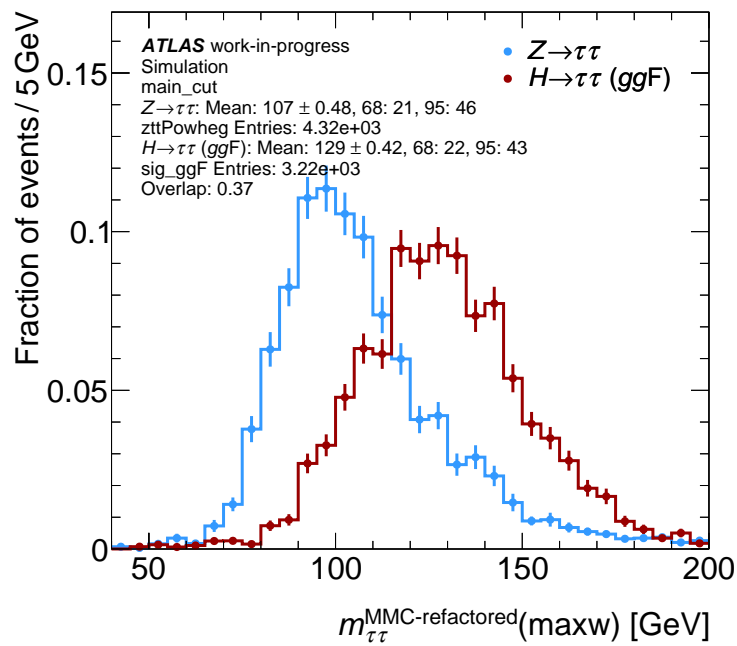


Figure 6.14: Higgs and Z boson mass estimates from the ditau mass reconstruction of double $3p0n$ events after adding parametrised PDFs.

Conclusion

To continue probing the Standard Model and to gain a deeper understanding of the fundamental mechanisms of the universe, it is important to continually improve the precision and accuracy of data analysis. The initial aim of this thesis was to include available vertex information which should help constrain the reconstruction of the full τ momentum \mathbf{P}_τ in the present algorithms for determining the Higgs mass through event kinematics reconstruction. This would have broader applications as improving the reconstruction of full τ momenta will lead to better constraints placed on multiple properties of the Higgs boson, as well as provide more experimental information on the Higgs interaction with massive fermions.

The ATLAS detector at the LHC and the reconstruction techniques for the target events have been established and improved for several years. The first realisation of the Higgs-like particle in 2012 and the subsequent methods to confirm the finding and constrain the properties of this particle are constantly being improved. One method for analysis is the MMC which is the setting for this thesis. This system for reconstructing ditau events does not yet make use of all information which is available. Namely the vertices and their associated error of the τ are yet to be included but can offer an avenue of improvement.

To this end, the viability of including this information was probed and the effect of its inclusion was evaluated. A vertex-based \mathbf{P}_τ solution was derived and checked using the truth data from simulation. The solution was able to recreate the true values to within 0.02% for the majority of events, although the solutions were slightly shifted to higher energies. This gives evidence of the possibility of a vertex-based reconstruction providing accurate constraints on the total reconstruction. The uncertainties which are present in the reconstructed vertex information however significantly effect the range of solutions (see Section 5.1). The complexity of the vertex-based solution also made the task of propagating the error for each individual event very difficult. Furthermore, the vertex-based solution is prone to returning unreal values when the reconstruction of the vertex position is off. To overcome this tendency, a Metropolis Hastings Algorithm was implemented with the assumption that the real solution was within an area defined by an ensemble resolution and also that a correct solution was usually close to the given solution (See section 5.3). This method, although effective at returning real solutions, is not directly useable as it creates large computation times (mean time per event is $\approx 950 \mu\text{s}$ compared to the current mean time of $\approx 32 \mu\text{s}$ for double $3p0n$ ditau events). Further improvements to the sensitivity of the solution (i.e. restructuring to produce less NAN-values) or to the treatment of uncertainties in the vertex reconstruction could fix this problem.

Like other solutions of the τ kinematics from visible detector tracks (i.e the \mathbf{P}_v solution inside the MMC), there is an ambiguity which arises. A separate study on determining the ability to predict the correct solution and the effect of these predictions was undertaken. The ambiguity study was performed in the context of the vertex-based reconstruction. A similar process can be repeated for other contexts of ambiguities in the τ reconstruction (for instance, non vertex-based kinematic reconstructions). Of the ambiguous solutions, the one closest to the true value was used to create difference plots for the entire set of events (See Figures 6.1(a), 6.1(b), 6.1(c), 6.1(d), and 6.1(e)). This resolution showed the optimal performance available at the current level of reconstructed solutions in the vertex-based derivation. When this resolution is comparable to the PDFs currently in the MMC it is expected that the MMC will be improved. When the resolution is far more, the current PDFs should dominate the reconstruction probability, and when the resolution is far less the event-by-event PDFs should dominate. The resulting resolutions were comparable to those in the MMC and so the initial assumption was that the MMC would be improved, or unchanged. The next step was to get the set of 2 solutions per event as close as possible to the optimal possible performance. It was determined that the correct leading solution could be predicted in 75% of events using truth information. This was first applied as a weight to the solutions in the PDF, but later it was determined that the solution using the reconstructed information required a different weight. For the reconstructed information, 83% of leading τ solutions could be predicted (see Figures 6.6(a) and 6.9(a)). A further parametrisation of the relative difference in energies of the two solutions increased the predictability. The weighted solutions created distributions which were more representative of the optimal possible reconstruction. This however did not improve the performance of the MMC. Although the technique for determining the true solution was effective in shifting the PDF variable distributions towards the more correct solutions (See Figures 6.2(a), 6.2(b), 6.2(c), 6.2(d), 6.2(e), Figures 6.4(a), 6.4(b), 6.4(c), 6.4(d), 6.4(e), Figures 6.8(a), 6.8(b), 6.8(c), 6.8(d), 6.8(e), and Figures 6.11(a), 6.11(b), 6.11(c), 6.11(d), and 6.11(e)), the event-by-event PDF inputs to the MMC were still unable to provide improvements (i.e. Figures 6.10(a), 6.10(b), 6.10(c), 6.10(d), and 6.10(e)).

In future attempts to include the vertex information, improvements can be made in finding a proper event-specific uncertainty in the PDFs. This should have the effect of dominating over the current ensemble PDFs when uncertainties are small. When uncertainties are high, however, this causes little to no effect except for increased run time. Improving the vertex reconstruction as well as reformulating the vertex-derived solution to decrease the sensitivity to errors will also have a positive impact on the solutions.

Other studies with kinematic reconstruction ambiguities can use the parametrisation techniques to give weights to possible solutions. More parametrisation variables may be considered which may increase the predictability of solutions.

Bibliography

- [1] G. Aad, T. Abajyan et al., *Observation of a new particle in the search for the Standard Model Higgs boson with the ATLAS detector at the LHC*, **Physics Letters B** **716** (2012) 1, ISSN: 0370-2693, URL: <http://www.sciencedirect.com/science/article/pii/S037026931200857X> (cit. on p. 1).
- [2] W. Kilian et al., *High-energy vector boson scattering after the Higgs boson discovery*, **Phys. Rev. D** **91** (9 2015) 096007, URL: <https://link.aps.org/doi/10.1103/PhysRevD.91.096007> (cit. on p. 1).
- [3] G. Aad et al., *Evidence for the Higgs-boson Yukawa coupling to the tau lepton with the ATLAS detector*, **Journal of High Energy Physics** **2015** (2015), ISSN: 1029-8479, URL: [http://dx.doi.org/10.1007/JHEP04\(2015\)117](http://dx.doi.org/10.1007/JHEP04(2015)117) (cit. on p. 1).
- [4] M. Huebner, *Effects of tau decay product reconstruction in a Higgs CP analysis with the ATLAS experiment*, University of Bonn, 2016, URL: <https://www.lhc-ilc.physik.uni-bonn.de/ergebnisse/dateien/t00000081.pdf?c=t&id=81> (cit. on pp. 1, 16).
- [5] D. Hohn, *Measurements of Higgs boson production in decays to two tau leptons with the ATLAS detector*, tech. rep., ATL-COM-PHYS-2019-1369, 2019 (cit. on p. 1).
- [6] M. Norlin, *Mass reconstruction techniques in di-Higgs events with τ -leptons and b -quarks in the ATLAS experiment at the LHC*, Uppsala Universitet, 2016, URL: <https://www.diva-portal.org/smash/get/diva2:1056072/FULLTEXT01.pdf> (cit. on p. 1).
- [7] A. Elagin et al., *A new mass reconstruction technique for resonances decaying to $\tau\tau$* , **Nuclear Instruments and Methods in Physics Research Section A: Accelerators, Spectrometers, Detectors and Associated Equipment** **654** (2011) 481, ISSN: 0168-9002, URL: <http://www.sciencedirect.com/science/article/pii/S0168900211014112> (cit. on pp. 1, 33).
- [8] M. Thomson, *Modern Particle Physics*, 1st ed., Cambridge University Press, 2013 (cit. on pp. 3, 7–10, 20).
- [9] D. Griffiths, *Introduction to Elementary Particles*, 2nd ed., Wiley-vch, 2008 (cit. on pp. 3, 7, 8, 16).

- [10] W. Commons, *File:Standard Model of Elementary Particles modified version.svg* — *Wikimedia Commons, the free media repository*, [Online; accessed 27-December-2020], 2020, URL: https://commons.wikimedia.org/w/index.php?title=File:Standard_Model_of_Elementary_Particles_modified_version.svg&oldid=454788240 (cit. on p. 4).
- [11] A. Pich, *The Standard Model of Electroweak Interactions*, 2004 European School of High Energy Physics, Saint Feliu de Guixols, Spain (2004), arXiv: [hep-ph/0502010](https://arxiv.org/abs/hep-ph/0502010) (cit. on pp. 4–6).
- [12] P. Particle Data Group Zyla et al., *Review of Particle Physics*, *PTEP* **2020** (2020) 083C01 (cit. on pp. 5, 10, 26).
- [13] P. Achard et al., *Measurement of the running of the electromagnetic coupling at large momentum-transfer at LEP*, *Physics Letters B* **623** (2005) 26, ISSN: 0370-2693, URL: <http://www.sciencedirect.com/science/article/pii/S0370269305010439> (cit. on pp. 5, 6).
- [14] M. Kobel, *Direct measurements of the electromagnetic coupling constant at large q^2* , (1997) (cit. on p. 6).
- [15] S. Bethke, *The 2009 World Average of α* , *The European Physical Journal C* **64** (2009) 689 (cit. on p. 8).
- [16] Nobelprize.org, *The Nobel Prize in Physics 2013*, URL: <http://www.nobelprize.org/prizes/physics//2013/> (cit. on pp. 9, 17).
- [17] M. D. Schwartz, *Quantum Field Theory and the Standard Model*, 1st ed., Cambridge University Press, 2014 (cit. on p. 9).
- [18] W. de Boer and CMS, “The Discovery of the Higgs Boson with the CMS Detector and its Implications for Supersymmetry and Cosmology”, *Time and Matter*, 2013, arXiv: [1309.0721](https://arxiv.org/abs/1309.0721) [[hep-ph](https://arxiv.org/abs/hep-ph)] (cit. on pp. 10, 12).
- [19] J. C. Baez, *Hypercharge and Weak Isospin*, 2003, URL: <https://math.ucr.edu/home/baez/qg-spring2003/hypercharge/hypercharge.pdf> (cit. on p. 9).
- [20] Xianhao, Xin, *Glashow-Weinberg-Salam Model: An Example of Electroweak Symmetry Breaking*, 2007, URL: https://guava.physics.uiuc.edu/~nigel/courses/569/Essays_Fall2007/files/Xianhao_xin.pdf (cit. on p. 10).
- [21] K. Jakobs, “Physics at the LHC – From Standard Model measurements to Searches for New Physics”, *2011 European School of High-Energy Physics*, 2014 309, arXiv: [1206.7024](https://arxiv.org/abs/1206.7024) [[hep-ex](https://arxiv.org/abs/hep-ex)] (cit. on p. 11).
- [22] M. Neubauer, *Higgs Boson Physics*, URL: https://msneubauer.github.io/projects/4_project/ (cit. on p. 12).

-
- [23] H. Maddocks, *Vertex Based Missing Mass Calculator for 3-prong Hadronically Decaying Tau Leptons in the ATLAS Detector*, Lancaster University, 2014, URL: <https://inspirehep.net/files/972e3c21cc826010a1766145ba0740ba> (cit. on p. 13).
- [24] P. Ilten, *Electroweak and Higgs Measurements Using Tau Final States with the LHCb Detector*, University College Dublin, 2013, URL: <https://arxiv.org/pdf/1401.4902.pdf> (cit. on p. 13).
- [25] F. Cooper, A. Khare and U. Sukhatme, *Supersymmetry and quantum mechanics*, *Physics Reports* **251** (1995) 267, ISSN: 0370-1573, URL: <http://www.sciencedirect.com/science/article/pii/037015739400080M> (cit. on p. 13).
- [26] G. Aad, E. Abat and A. Abbott et al., *Expected performance of the ATLAS experiment: detector, trigger and physics*, arXiv:0901.0512, CERN, 2009, URL: <https://cds.cern.ch/record/1125884> (cit. on pp. 13, 17, 24, 25).
- [27] G. Aad et al., *Identification and energy calibration of hadronically decaying tau leptons with the ATLAS experiment in pp collisions at $\sqrt{s} = 8\text{TeV}$* , *European Physical Journal C: Particles and Fields* (2014), ISSN: 1434-6044, URL: <http://ui.adsabs.harvard.edu/abs/2014arXiv1412.7086A> (cit. on p. 14).
- [28] G. Aad, B. Abbott and et al., *Reconstruction of Hadronic Decay Products of tau leptons with the ATLAS experiment*, *The European Physical Journal C* **76** (2016) 295, URL: <https://doi.org/10.1140/epjc/s10052-016-4110-0> (cit. on pp. 13, 17, 25–27).
- [29] W. Buchmüller, *Baryogenesis – 40 Years Later*, 2007, arXiv: 0710.5857 [hep-ph] (cit. on p. 14).
- [30] H. Primakoff and P. S. Rosen, *BARYON NUMBER AND LEPTON NUMBER CONSERVATION LAWS*, *Ann. Rev. Nucl. Part. Sci.* **31** (1981) 145 (cit. on pp. 14, 15).
- [31] K. S. Babu et al., *Baryon Number Violation*, 2013, arXiv: 1311.5285 [hep-ph] (cit. on p. 15).
- [32] Nobelprize.org, *The Nobel Prize in Physics 2015*, URL: <http://www.nobelprize.org/prizes/physics/2015/> (cit. on p. 15).
- [33] R. M. Fonseca, *Violation of lepton number in 3 units*, 2019, arXiv: 1903.09675 [hep-ph] (cit. on p. 15).
- [34] M. Shaposhnikov, *Baryon Asymmetry of the Universe and Neutrinos*, *Progress of Theoretical Physics* **122** (1 2009), URL: https://watermark.silverchair.com/122-1-185.pdf?token=AQECAHi208BE490oan9kkhW_Ercy7Dm3ZL_9Cf3qfKAc485ysgAAAqkwggK1BgkqhkiG9w0BBwagggKWMIIckgIBADCCAosGCSqGSIb3DQEHATAeBg1ghkgBZQM R2LT3xfSewsvdWdAgEQgIICXAGGEb0ta9gCJ310L2znUMto6tguDhHgFYVRT8uE-VEf3vAaGQhn-p7nFCm-y7BR3XTvt3Zd9zJ24T_15yRZl0h0GlB54aZfgEdWRgWy_6jESC_

- 8sIOZHT632A7P7LEDwxYBzkuG_8iffneK7DXz8zXoYKRkkgiyVeNSW9f_
 hlQoU9X97yS4I8o74wkw3KFqtPtK8YwAp400t8LfS0kwxbxXEnevhe63sCrhoJzwuhFLW0_
 I2sHb5DSBdyWYTYT6EJwbvxzT37xHqvhkC_
 PwUJShwzBgDfh9kSmS5s759YGxgeotxnM0JejiBwhN7zBuVYB8F4Bp42BNQAeS_m_
 Y6L9bpnp0txsr6TybxX668S_nzgm9zQakUbg79qetM0bsDnDsTfUxq29evva1Ud_Zd_
 qvG3PgZzJuZSKqxRnJN8Ce-
 W6v3Ys1Tv2OMWzEFOXmWNjNjvhwj87z8Jh3udZSxs6feMACFP4JbIRUVE1A6U3hmQBWj_
 snsXr-zBStfNM1-hkL2GeJ9mIo_gBYs1Hqtzt9r6_
 9UDQvddHeuZ96n81xLOM8jGZ0as00CIT1JR2uTh6fk31XRD2FE-
 5aeAAKD9EP3x6XzQtmQKi3p4Ur9E_
 u49ZA84IC0YEZY1AyEgNConVVQmwTrpTM0GDQIDc0rauMeXF6X5HBqUzzE-m3s-
 J26yWMkqYtR8S_XgtNB8YU51KirK3SsqM6rf- ipIRgJgcj_
 gCn4YBqLOMu1gRXge3gzK2hdvSRh3EGnKCD65X7gBdWH5bkF3pnkp96C2An1tOJXoA0mDrOfPzw
 (cit. on p. 15).
- [35] M. Worek, “HIGGS CP FROM $H/A^0 \rightarrow \tau\tau$ DECAY ”, 2003 (cit. on p. 16).
- [36] C. Press, *LHC Season 2 facts and figures*,
 URL: https://home.cern/sites/home.web.cern.ch/files/2018-07/factsandfigures-en_0.pdf (cit. on p. 17).
- [37] T. C. Collaboration, S. Chatrchyan and G. H. andet al., *The CMS experiment at the CERN LHC*,
Journal of Instrumentation **3** (2008) S08004,
 URL: <https://doi.org/10.1088/1748-0221/3/08/s08004> (cit. on p. 17).
- [38] G. Aad et al., *Search for a heavy particle decaying into an electron and a muon with the ATLAS detector in $\sqrt{s} = 7$ TeV pp collisions at the LHC.*,
Physical review letters **106** (2011) 251801 (cit. on p. 18).
- [39] G. Weiglein et al., *Physics interplay of the LHC and the ILC*, *Physics Reports* **426** (2006) 47,
 ISSN: 0370-1573, URL: <http://dx.doi.org/10.1016/j.physrep.2005.12.003>
 (cit. on pp. 18, 19).
- [40] T. A. Collaboration et al., *The ALICE experiment at the CERN LHC*,
Journal of Instrumentation **3** (2008) S08002,
 URL: <https://doi.org/10.1088/1748-0221/3/08/s08002> (cit. on p. 17).
- [41] T. L. Collaboration et al., *The LHCb Detector at the LHC*,
Journal of Instrumentation **3** (2008) S08005,
 URL: <https://doi.org/10.1088/1748-0221/3/08/s08005> (cit. on p. 17).
- [42] ATLAS Collaboration et al., *The ATLAS Experiment at the CERN Large Hadron Collider*,
Journal of Instrumentation **3** (2008) S08003,
 URL: <https://doi.org/10.1088/1748-0221/3/08/s08003> (cit. on pp. 19, 21–23).
- [43] A. La Rosa, *ATLAS IBL Pixel Upgrade*,
Nuclear Physics B - Proceedings Supplements **215** (2011) 147, Proceedings of the 12th Topical
 Seminar on Innovative Particle and Radiation Detectors (IPRD10), issn: 0920-5632,
 URL: <http://www.sciencedirect.com/science/article/pii/S0920563211002313>
 (cit. on p. 20).

-
- [44] A. Collaboration, *ATLAS inner detector: Technical Design Report, 1*, Technical Design Report ATLAS CERN-LHCC-97-016, CERN, 1997, URL: <https://cds.cern.ch/record/331063> (cit. on p. 20).
- [45] C. Grupen and B. Shwartz, *Particle Detectors*, 2nd ed., Cambridge University Press, 2008 (cit. on p. 22).
- [46] Y. Nakahama, *The ATLAS Trigger System: Ready for Run-2*, *Journal of Physics: Conference Series* **664** (2015) 082037, URL: <https://doi.org/10.1088/1742-6596/664/8/082037> (cit. on pp. 22, 23).
- [47] P. Jenni et al., *ATLAS high-level trigger, data-acquisition and controls: Technical Design Report*, Technical Design Report ATLAS, CERN, 2003, URL: <https://cds.cern.ch/record/616089> (cit. on p. 23).
- [48] A. Collaboration, *Photon identification in 2015 ATLAS data*, tech. rep. ATL-PHYS-PUB-2016-014, CERN, 2016, URL: <https://cds.cern.ch/record/2203125> (cit. on p. 23).
- [49] M. Aaboud et al., *Measurement of the photon identification efficiencies with the ATLAS detector using LHC Run 2 data collected in 2015 and 2016*, *The European Physical Journal C* **79** (2019), ISSN: 1434-6052, URL: <http://dx.doi.org/10.1140/epjc/s10052-019-6650-6> (cit. on p. 23).
- [50] M. Aaboud et al., *Electron reconstruction and identification in the ATLAS experiment using the 2015 and 2016 LHC proton–proton collision data at*

$$\sqrt{s} = 13$$

TeV

- , *The European Physical Journal C* **79** (2019), ISSN: 1434-6052, URL: <http://dx.doi.org/10.1140/epjc/s10052-019-7140-6> (cit. on p. 24).
- [51] N. M. Koehler and A. Collaboration, *ATLAS Muon Reconstruction Performance in LHC Run 2*, (2016) 621, ed. by V. T. Kim and D. E. Sosnov (cit. on p. 24).
- [52] G. Aad, ATLAS Collaboration et al., *Measurement of the muon reconstruction performance of the ATLAS detector using 2011 and 2012 LHC proton–proton collision data*, *Eur. Phys. J. C* **74** (2014) 3130, arXiv: 1407.3935 [hep-ex] (cit. on p. 24).
- [53] *Jet Calibration and Systematic Uncertainties for Jets Reconstructed in the ATLAS Detector at $\sqrt{s} = 13$ TeV*, tech. rep. ATL-PHYS-PUB-2015-015, CERN, 2015, URL: <http://cds.cern.ch/record/2037613> (cit. on p. 24).
- [54] M. Cacciari, G. P. Salam and G. Soyez, *The anti-ktjet clustering algorithm*, *Journal of High Energy Physics* **2008** (2008) 063, ISSN: 1029-8479, URL: <http://dx.doi.org/10.1088/1126-6708/2008/04/063> (cit. on p. 25).
- [55] ATLAS Collaboration, *Performance of the Reconstruction and Identification of Hadronic Tau Decays with ATLAS*, tech. rep. ATLAS-CONF-2011-152, CERN, 2011, URL: <https://cds.cern.ch/record/1398195> (cit. on pp. 25, 27).

- [56] G. Bagliesi, *Tau tagging at Atlas and CMS*, 2007, arXiv: [0707.0928 \[hep-ex\]](#) (cit. on p. 26).
- [57] A. Collaboration, *Constituent-level pile-up mitigation techniques in ATLAS*, tech. rep. ATLAS-CONF-2017-065, CERN, 2017, URL: <http://cds.cern.ch/record/2281055/files/ATLAS-CONF-2017-065.pdf?version=1> (cit. on p. 27).
- [58] A. Collaboration, *Performance of the Reconstruction and Identification of Hadronic Tau Decays in ATLAS with 2011 Data*, tech. rep. ATLAS-CONF-2012-142, CERN, 2012, URL: <http://cds.cern.ch/record/1485531> (cit. on pp. 27–29).
- [59] M. Aaboud et al., *Performance of missing transverse momentum reconstruction with the ATLAS detector using proton–proton collisions at*
- $$\sqrt{s} = 13 \text{ TeV}$$
- , *The European Physical Journal C* **78** (2018), ISSN: 1434-6052, URL: <http://dx.doi.org/10.1140/epjc/s10052-018-6288-9> (cit. on p. 29).
- [60] P. Berta, *ATLAS jet and missing-ET reconstruction, calibration, and performance*, *Nuclear and Particle Physics Proceedings* **273-275** (2016) 1121, 37th International Conference on High Energy Physics (ICHEP), ISSN: 2405-6014, URL: <http://www.sciencedirect.com/science/article/pii/S2405601415006653> (cit. on p. 29).
- [61] A. Buckley et al., *General-purpose event generators for LHC physics*, *Physics Reports* **504** (2011) 145, ISSN: 0370-1573, URL: <http://dx.doi.org/10.1016/j.physrep.2011.03.005> (cit. on p. 29).
- [62] S. Höche, *Introduction to parton-shower event generators*, 2015, arXiv: [1411.4085 \[hep-ph\]](#) (cit. on p. 29).
- [63] P. Nason, *A New Method for Combining NLO QCD with Shower Monte Carlo Algorithms*, *Journal of High Energy Physics* **2004** (2004) 040, URL: <https://doi.org/10.1088/1126-6708/2004/11/040> (cit. on p. 30).
- [64] S. Frixione, P. Nason and C. Oleari, *Matching NLO QCD computations with parton shower simulations: the POWHEG method*, *Journal of High Energy Physics* **2007** (2007) 070, URL: <https://doi.org/10.1088/1126-6708/2007/11/070> (cit. on p. 30).
- [65] T. Sjöstrand, S. Mrenna and P. Skands, *A brief introduction to PYTHIA 8.1*, *Computer Physics Communications* **178** (2008) 852, ISSN: 0010-4655, URL: <http://www.sciencedirect.com/science/article/pii/S0010465508000441> (cit. on p. 30).
- [66] S. Alioli et al., *A general framework for implementing NLO calculations in shower Monte Carlo programs: the POWHEG BOX*, *Journal of High Energy Physics* (2010), ISSN: 1029-8479 (cit. on p. 30).
- [67] C. M. Grinstead and J. L. Snell, *Introduction to Probability*, 2nd ed., American Mathematical Society (cit. on p. 31).

-
- [68] D. van Ravenzwaaij, P. Cassey and S. Brown,
A simple introduction to Markov Chain Monte–Carlo sampling,
Psychon Bull Rev **25** (2018) 143 (cit. on p. 32).
- [69] C. P. Robert, *The Metropolis-Hastings algorithm*, 2016, arXiv: 1504.01896 [stat.CO]
(cit. on p. 32).
- [70] M. Pitt,
Search for the Standard Model Higgs boson in the $H \rightarrow \tau\tau$ channel with the ATLAS detector,
tech. rep. ATL-PHYS-PROC-2013-141, CERN, 2013,
URL: <http://cds.cern.ch/record/1554090> (cit. on p. 33).
- [71] S. Pranko, *Mass Reconstruction With MMC*, 2012,
URL: https://indico.desy.de/event/7444/contributions/82582/attachments/55208/67272/MMC_workshop_Bonn_031512.pdf (cit. on p. 34).
- [72] A. Collaboration,
“Experiment Briefing: Keeping the ATLAS Inner Detector in perfect alignment”, 2020,
URL: <https://cds.cern.ch/record/2723878> (cit. on p. 39).

Useful Information

A.1 Notation

In this section, a brief introduction to the notation used in Chapters 5 and 6 is given. Momentum 3-vectors are written as \mathbf{p}_i^j where $i \in (\tau, \nu)$ corresponding the particles which they represent. $j \in (l, s)$ represents the leading and subleading τ s respectively. The components of the 3-vector are

$$\mathbf{p}_i^j = (p_{i_1}^j, p_{i_2}^j, p_{i_3}^j) \quad (\text{A.1})$$

where $(1, 2, 3) = (x, y, z)$. So as an example, $p_{\nu_2}^s$ corresponds to the y -component of the momentum of the ν associated to the subleading τ . Magnitudes of 3-vectors are written as

$$p_i^j = \|\mathbf{p}_i^j\| = \sqrt{\sum_{k \in (1,2,3)} (p_{i_k}^j)^2}. \quad (\text{A.2})$$

The 4-momentum is written similarly as

$$\mathbf{P}_i^j = (P_{i_0}^j, P_{i_1}^j, P_{i_2}^j, P_{i_3}^j). \quad (\text{A.3})$$

where 0 corresponds to the associated Energy. When 3-momentum or 4-momentum vectors are written without the j superscript, then the mention is meant to be applied to both leading and subleading τ s.

A.2 Vertex based \mathbf{P}_τ solution

The solution for the \mathbf{P}_τ is long and it is difficult to see the structure when written completely. Therefore, several variables are defined which make the solution easier to visualize. The τ flight distance is \mathbf{R} is

$$\mathbf{R} = \begin{pmatrix} r_1 \\ r_2 \\ r_3 \end{pmatrix} = \begin{pmatrix} v_x^{sec} - v_x^{prim} \\ v_y^{sec} - v_y^{prim} \\ v_z^{sec} - v_z^{prim} \end{pmatrix} \quad (\text{A.4})$$

where $v_{(x,y,z)}$ represents the x,y,z positions of the secondary (*sec*) and primary (*prim*) vertices. The newly defined variables are

$$a = -m_\tau^2 - p_{vis_0}^2 + p_{vis_1}^2 + p_{vis_2}^2 + p_{vis_3}^2 = -m_\tau^2 - \mathbf{P}_{vis}^2 = -(m_\tau^2 + m_{vis}^2) \quad (\text{A.5})$$

$$A = ar_1 \quad (\text{A.6})$$

$$B = 4A(p_{vis_1}r_1 + p_{vis_2}r_2 + p_{vis_3}r_3) = 4A(\mathbf{p}_{vis} \cdot \mathbf{R}) \quad (\text{A.7})$$

$$D = A^2 - 4m_\tau^2 p_{vis_0}^2 r_1^2 \quad (\text{A.8})$$

$$E = 4(-p_{vis_0}^2)(r_1^2 + r_2^2 + r_3^2) + (r_1 p_{vis_1} + r_2 p_{vis_2} + r_3 p_{vis_3})^2 = 4(-p_{vis_0}^2)(\mathbf{R}^2) + (\mathbf{R} \cdot \mathbf{p}_{vis})^2 \quad (\text{A.9})$$

In terms of these new variables, the \mathbf{P}_τ solutions become

$$p_{\tau_0} = -\frac{A - \frac{p_{vis_1}r_1(B \pm \sqrt{(-B)^2 - 4DE})}{E} - \frac{p_{vis_2}r_2(B \pm \sqrt{(-B)^2 - 4DE})}{E} - \frac{p_{vis_3}r_3(B \pm \sqrt{(-B)^2 - 4DE})}{E}}{2p_{vis_0}r_1} \quad (\text{A.10})$$

$$p_{\tau_1} = \frac{B \pm \sqrt{(-B)^2 - 4DE}}{2E} \quad (\text{A.11})$$

$$p_{\tau_2} = r_2 \frac{p_{\tau_1}}{r_1} \quad (\text{A.12})$$

$$p_{\tau_3} = r_3 \frac{p_{\tau_1}}{r_1} \quad (\text{A.13})$$

Here one can see the term which produces unuseable values (NAN values). It is the term which appears four times underneath the square root

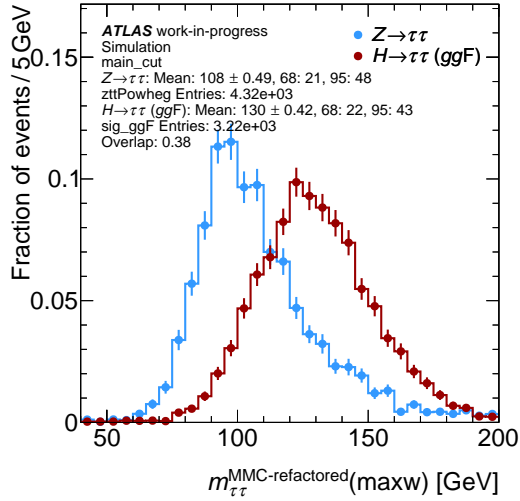
$$\text{NAN term} = B^2 - 4DE \quad (\text{A.14})$$

Every successful iteration of the MH algorithm which is used to determine useable solutions from unuseable ones, updates \mathbf{R} . Components of \mathbf{R} appear in every newly defined term, and therefore every step from the initial positions changes each variable.

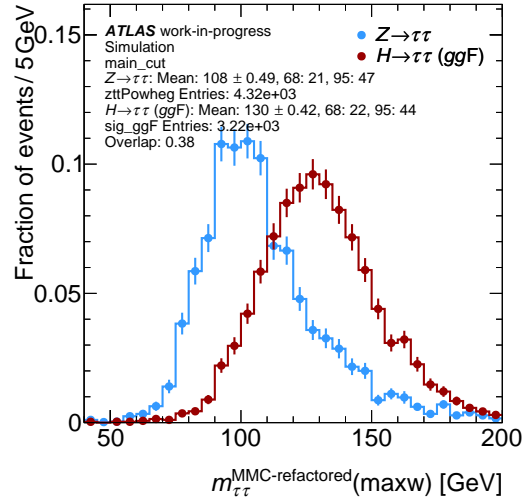
A.3 MH scan for optimization before solution parametrisation

The following plots show the ditau mass reconstruction for different conditions in the MH algorithm. These are done with weighted solutions according to the truth-determined prediction bias: 75% and 25% weights for the low and high energy leading τ solution respectively and 56% and 44% for the subleading τ . The number of seeds which started the MH algorithm for each event is varied between 50 and 100. The number of max iterations the MH could perform was varied between 10^6 and 10^8 . Each set of graphs represents an increasing number of seeds while the a,b, and c component of each graph corresponds to an increase in MH iterations.

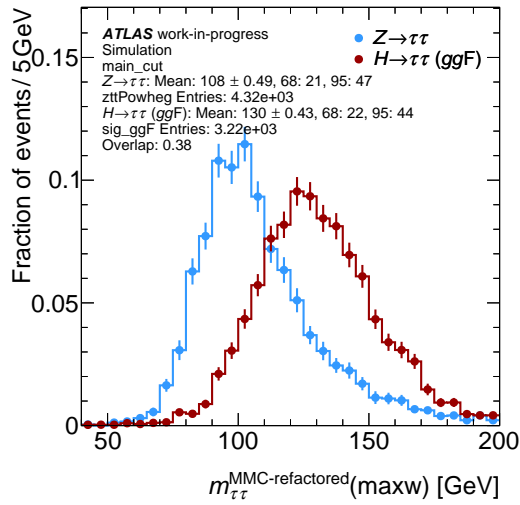
A.3 MH scan for optimization before solution parametrisation



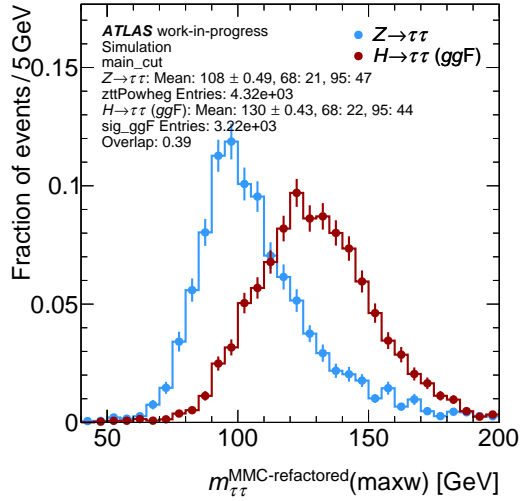
(a) Reconstructed ditau mass for 50 seeds and 10^6 iterations in the MH per event.



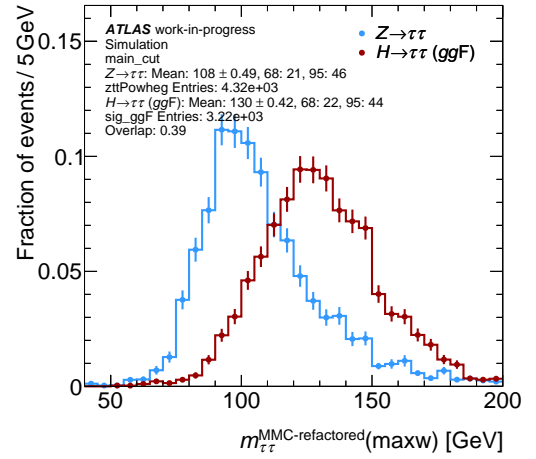
(b) Reconstructed ditau mass for 50 seeds and 10^7 iterations in the MH per event.



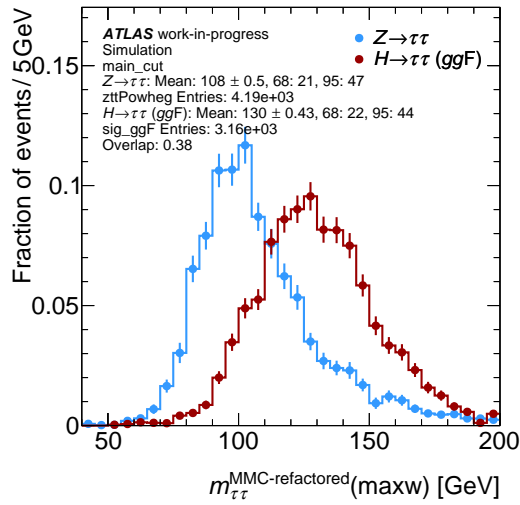
(c) Reconstructed ditau mass for 50 seeds and 10^8 iterations in the MH per event.



(a) Reconstructed ditau mass for 75 seeds and 10^6 iterations in the MH per event.

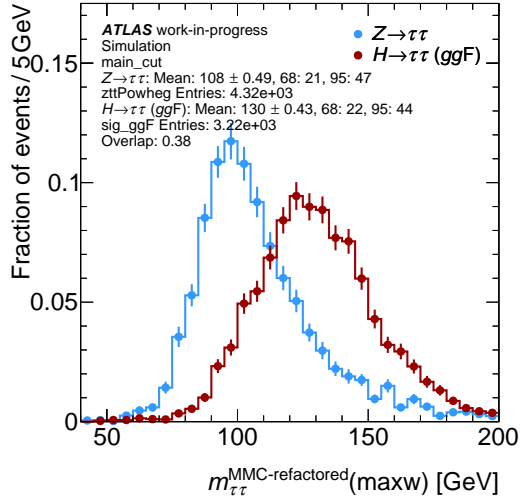


(b) Reconstructed ditau mass for 75 seeds and 10^7 iterations in the MH per event.

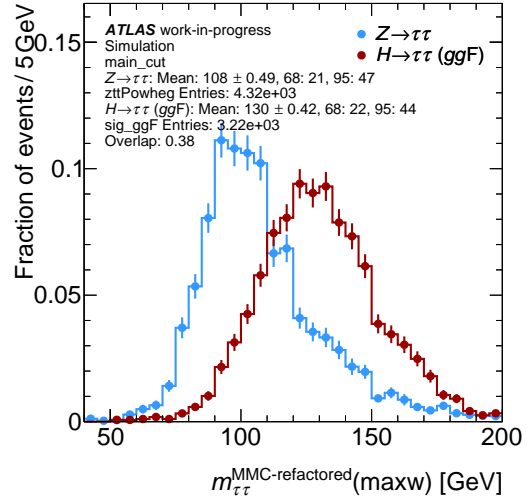


(c) Reconstructed ditau mass for 75 seeds and 10^8 iterations in the MH per event.

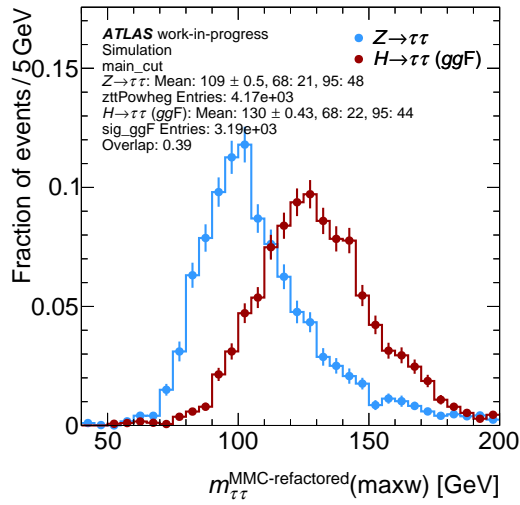
A.3 MH scan for optimization before solution parametrisation



(a) Reconstructed ditau mass for 100 seeds and 10^6 iterations in the MH per event.



(b) Reconstructed ditau mass for 100 seeds and 10^7 iterations in the MH per event.



(c) Reconstructed ditau mass for 100 seeds and 10^8 iterations in the MH per event.

A.4 Tables for solution parametrisation for each choice of MH variables

The following tables are given to show the parameterisation defined in Section 6.3. The tables come in pairs for the leading and subleading τ s respectively. They are categorised by the number of seeds ranging from 50 – 100 and the number of max iterations in the MH from 10^6 to 10^8

Distribution of Low Energy Bias in quantiles of ν

range of ν	Low Solution Bias	Number of Events
0.000 - 0.300	70%	516
0.300 - 0.469	74%	522
0.469 - 0.642	82%	445
0.642 - 0.824	85%	400
0.824 - 1.018	88%	359
1.018 - 1.246	92%	317
1.246 - 1.564	92%	258
1.564 - 2.101	94%	173
2.101 - 3.075	98%	76
3.075 - inf	100%	12

(a) Distribution of low energy solution bias in quantiles of ν for the leading τ for 50 seeds and 10^6 MH iterations

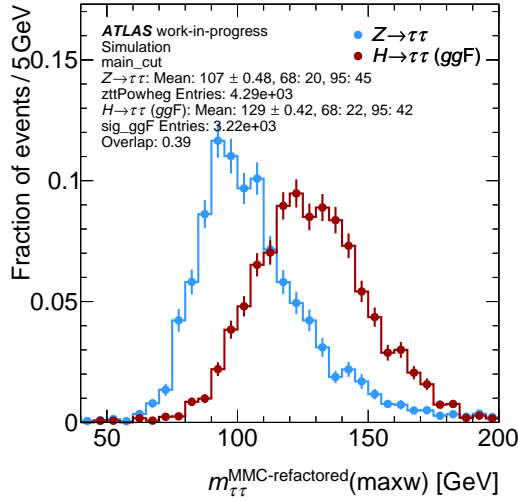
Distribution of Low Energy Bias in quantiles of ν

range of ν	Low Solution Bias	Number of Events
0.000 - 0.031	68%	136
0.031 - 0.062	63%	104
0.062 - 0.093	48%	90
0.093 - 0.216	58%	373
0.216 - 0.396	63%	438
0.396 - 0.630	67%	418
0.630 - 0.923	73%	411
0.923 - 1.399	82%	417
1.399 - 2.256	91%	363
2.256 - inf	92%	271

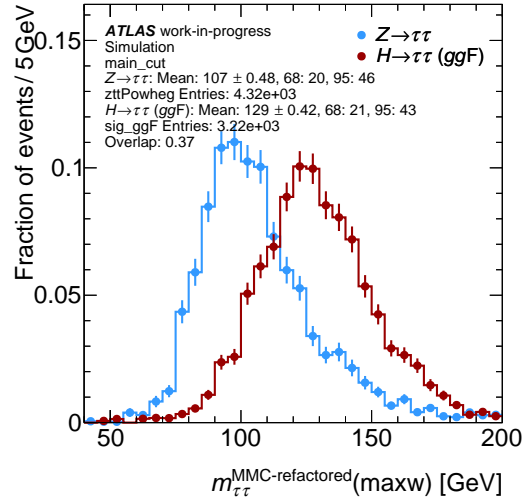
(b) Distribution of low energy solution bias in quantiles of ν for the subleading τ for 50 seeds and 10^6 MH iterations.

A.5 MH scan for optimization after solution parametrisation

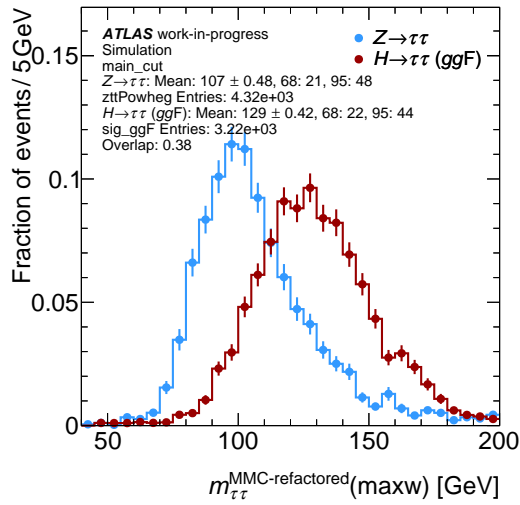
The graphs here are analogous to the ones shown in Appendix A.3. The solutions are instead weighted based on the parameterisation given in Appendix A.4.



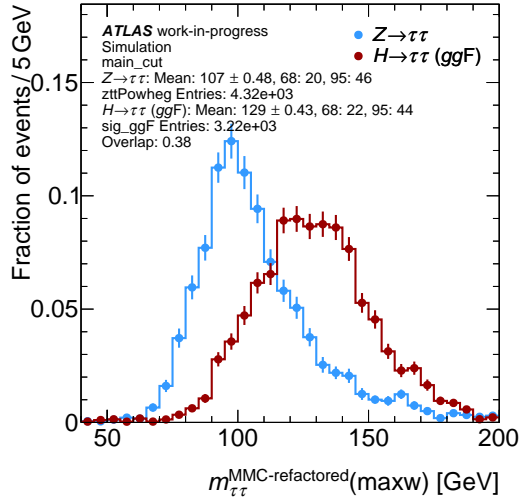
(a) Reconstructed ditau mass for 50 seeds and 10^6 iterations in the MH per event.



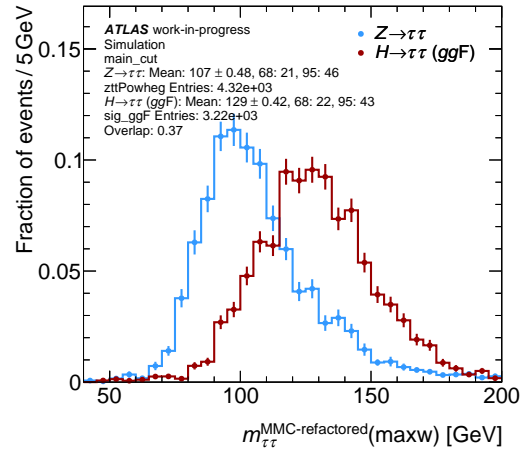
(b) Reconstructed ditau mass for 50 seeds and 10^7 iterations in the MH per event.



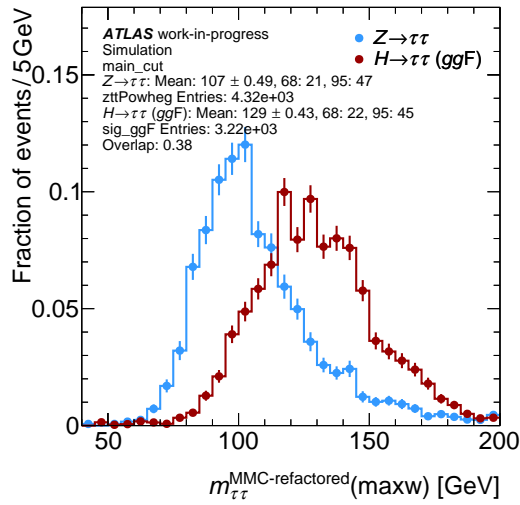
(c) Reconstructed ditau mass for 50 seeds and 10^8 iterations in the MH per event.



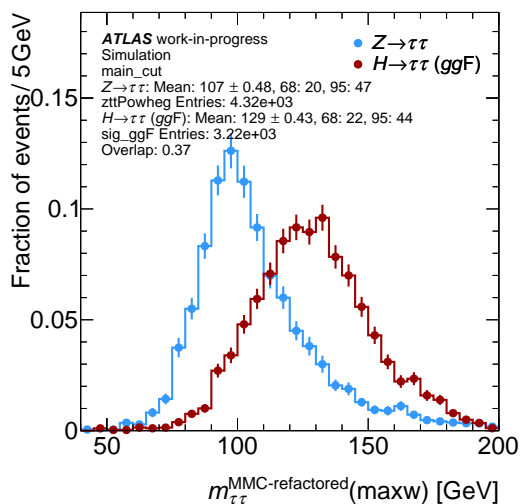
(a) Reconstructed ditau mass for 75 seeds and 10^6 iterations in the MH per event.



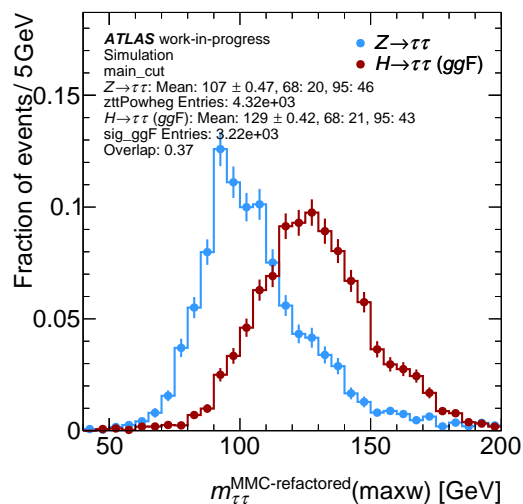
(b) Reconstructed ditau mass for 75 seeds and 10^7 iterations in the MH per event.



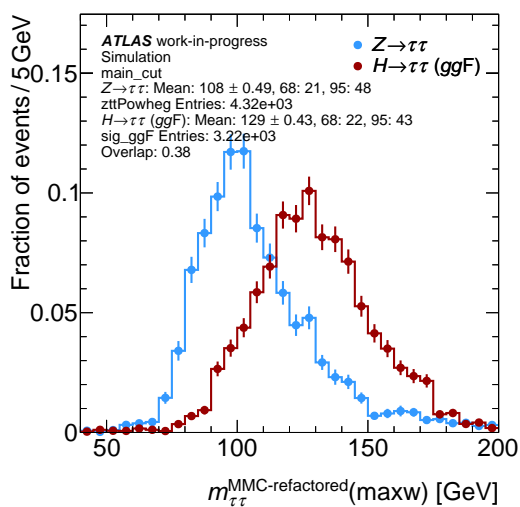
(c) Reconstructed ditau mass for 75 seeds and 10^8 iterations in the MH per event.



(a) Reconstructed ditau mass for 100 seeds and 10^6 iterations in the MH per event.



(b) Reconstructed ditau mass for 100 seeds and 10^7 iterations in the MH per event.



(c) Reconstructed ditau mass for 100 seeds and 10^8 iterations in the MH per event.

Distribution of Low Energy Bias in quantiles of ν

range of ν	Low Solution Bias	Number of Events
0.000 - 0.294	70%	508
0.294 - 0.469	78%	521
0.469 - 0.637	80%	460
0.637 - 0.812	84%	405
0.812 - 1.007	90%	378
1.007 - 1.239	90%	309
1.239 - 1.559	93%	256
1.559 - 2.088	95%	187
2.088 - 3.080	98%	61
3.080 - inf	100%	17

(a) Distribution of low energy solution bias in quantiles of ν for the leading τ for 50 seeds and 10^7 MH iterations.

Distribution of Low Energy Bias in quantiles of ν

range of ν	Low Solution Bias	Number of Events
0.000 - 0.031	71%	135
0.031 - 0.063	61%	90
0.063 - 0.095	47%	108
0.095 - 0.225	59%	383
0.225 - 0.404	63%	450
0.404 - 0.628	70%	411
0.628 - 0.927	75%	410
0.927 - 1.390	77%	395
1.390 - 2.250	90%	378
2.250 - inf	94%	280

(b) Distribution of low energy solution bias in quantiles of ν for the subleading τ for 50 seeds and 10^7 MH iterations.

Distribution of Low Energy Bias in quantiles of ν

range of ν	Low Solution Bias	Number of Events
0.000 - 0.290	70%	496
0.290 - 0.457	78%	515
0.457 - 0.628	80%	455
0.628 - 0.808	85%	413
0.808 - 1.000	88%	384
1.000 - 1.230	90%	336
1.230 - 1.550	91%	338
1.550 - 2.080	95%	255
2.080 - 3.050	95%	75
3.050 - inf	100%	13

(a) Distribution of low energy solution bias in quantiles of ν for the leading τ for 50 seeds and 10^8 MH iterations.

Distribution of Low Energy Bias in quantiles of ν

range of ν	Low Solution Bias	Number of Events
0.000 - 0.032	66%	147
0.032 - 0.064	62%	93
0.064 - 0.096	56%	79
0.096 - 0.220	58%	387
0.220 - 0.404	62%	464
0.402 - 0.628	66%	428
0.628 - 0.927	76%	395
0.927 - 1.388	80%	399
1.388 - 2.679	88%	380
2.679 - inf	94%	286

(b) Distribution of low energy solution bias in quantiles of ν for the subleading τ for 50 seeds and 10^8 MH iterations.

Distribution of Low Energy Bias in quantiles of ν

range of ν	Low Solution Bias	Number of Events
0.000 - 0.302	70%	575
0.302 - 0.469	75%	524
0.469 - 0.647	80%	454
0.647 - 0.824	84%	382
0.824 - 1.015	87%	369
1.015 - 1.235	93%	374
1.235 - 1.565	94%	263
1.565 - 2.565	95%	185
2.128 - 3.080	98%	62
3.080 - inf	100%	15

(a) Distribution of low energy solution bias in quantiles of ν for the leading τ for 75 seeds and 10^6 MH iterations.

Distribution of Low Energy Bias in quantiles of ν

range of ν	Low Solution Bias	Number of Events
0.000 - 0.031	66%	147
0.031 - 0.062	62%	93
0.062 - 0.094	56%	79
0.094 - 0.216	58%	381
0.216 - 0.395	62%	464
0.395 - 0.620	66%	428
0.620 - 0.917	76%	395
0.917 - 1.385	80%	399
1.385 - 2.239	88%	380
2.239 - inf	94%	286

(b) Distribution of low energy solution bias in quantiles of ν for the subleading τ for 75 seeds and 10^6 MH iterations.

Distribution of Low Energy Bias in quantiles of ν

range of ν	Low Solution Bias	Number of Events
0.000 - 0.288	70%	523
0.288 - 0.465	77%	508
0.465 - 0.636	79%	492
0.636 - 0.813	84%	387
0.813 - 1.014	89%	376
1.014 - 1.238	91%	322
1.238 - 1.558	93%	238
1.558 - 2.107	95%	179
2.107 - 3.090	100%	57
3.090 - inf	100%	17

(a) Distribution of low energy solution bias in quantiles of ν for the leading τ for 75 seeds and 10^7 MH iterations.

Distribution of Low Energy Bias in quantiles of ν

range of ν	Low Solution Bias	Number of Events
0.000 - 0.032	71%	139
0.032 - 0.063	56%	95
0.063 - 0.096	55%	98
0.096 - 0.232	56%	377
0.232 - 0.405	64%	458
0.405 - 0.622	68%	400
0.622 - 0.917	75%	404
0.917 - 1.377	78%	412
1.377 - 2.232	88%	375
2.232 - inf	94%	283

(b) Distribution of low energy solution bias in quantiles of ν for the subleading τ for 75 seeds and 10^7 MH iterations.

Distribution of Low Energy Bias in quantiles of ν

range of ν	Low Solution Bias	Number of Events
0.000 - 0.284	69%	490
0.284 - 0.451	79%	509
0.451 - 0.626	80%	464
0.626 - 0.803	82%	417
0.803 - 1.007	85%	383
1.007 - 1.234	90%	325
1.234 - 1.558	93%	253
1.558 - 2.116	94%	182
2.116 - 3.090	98%	70
3.090 - inf	100%	16

(a) Distribution of low energy solution bias in quantiles of ν for the leading τ for 75 seeds and 10^8 MH iterations.

Distribution of Low Energy Bias in quantiles of ν

range of ν	Low Solution Bias	Number of Events
0.000 - 0.031	71%	136
0.031 - 0.063	58%	97
0.063 - 0.095	53%	86
0.095 - 0.224	57%	382
0.224 - 0.406	65%	476
0.406 - 0.626	65%	411
0.626 - 0.923	74%	406
0.923 - 1.404	81%	391
1.404 - 2.266	89%	381
2.266 - inf	95%	282

(b) Distribution of low energy solution bias in quantiles of ν for the subleading τ for 75 seeds and 10^8 MH iterations.

Distribution of Low Energy Bias in quantiles of ν

range of ν	Low Solution Bias	Number of Events
0.000 - 0.290	70%	493
0.290 - 0.463	76%	523
0.463 - 0.637	79%	474
0.637 - 0.821	82%	412
0.821 - 1.009	85%	363
1.009 - 1.234	92%	294
1.234 - 1.569	93%	272
1.569 - 2.130	96%	180
2.130 - 3.110	99%	58
3.110 - inf	100%	18

(a) Distribution of low energy solution bias in quantiles of ν for the leading τ for 100 seeds and 10^6 MH iterations.

Distribution of Low Energy Bias in quantiles of ν

range of ν	Low Solution Bias	Number of Events
0.000 - 0.031	72%	127
0.031 - 0.062	62%	98
0.062 - 0.094	55%	100
0.094 - 0.213	54%	353
0.213 - 0.395	64%	461
0.395 - 0.621	68%	438
0.621 - 0.927	72%	408
0.927 - 1.393	80%	417
1.393 - 2.227	93%	345
2.227 - inf	92%	293

(b) Distribution of low energy solution bias in quantiles of ν for the subleading τ for 100 seeds and 10^6 MH iterations.

Distribution of Low Energy Bias in quantiles of ν

range of ν	Low Solution Bias	Number of Events
0.000 - 0.285	70%	493
0.285 - 0.457	77%	523
0.457 - 0.629	79%	474
0.629 - 0.806	83%	412
0.806 - 1.003	85%	363
1.003 - 1.222	92%	294
1.222 - 1.550	93%	272
1.550 - 2.101	96%	181
2.101 - 3.114	98%	58
3.114 - inf	100%	18

(a) Distribution of low energy solution bias in quantiles of ν for the leading τ for 100 seeds and 10^7 MH iterations.

Distribution of Low Energy Bias in quantiles of ν

range of ν	Low Solution Bias	Number of Events
0.000 - 0.031	72%	127
0.031 - 0.063	62%	94
0.063 - 0.095	54%	100
0.095 - 0.227	54%	353
0.227 - 0.402	64%	461
0.402 - 0.626	77%	438
0.626 - 0.924	72%	408
0.924 - 1.383	80%	417
1.383 - 2.249	93%	345
2.249 - inf	92%	280

(b) Distribution of low energy solution bias in quantiles of ν for the subleading τ for 100 seeds and 10^7 MH iterations.

Distribution of Low Energy Bias in quantiles of ν

range of ν	Low Solution Bias	Number of Events
0.000 - 0.284	69%	493
0.284 - 0.452	79%	484
0.452 - 0.626	80%	471
0.626 - 0.803	83%	444
0.803 - 1.008	83%	371
1.008 - 1.239	89%	311
1.239 - 1.567	92%	265
1.567 - 2.116	96%	192
2.116 - 3.108	97%	66
3.108 - inf	100%	15

(a) Distribution of low energy solution bias in quantiles of ν for the leading τ for 100 seeds and 10^8 MH iterations.

Distribution of Low Energy Bias in quantiles of ν

range of ν	Low Solution Bias	Number of Events
0.000 - 0.031	68%	131
0.031 - 0.063	59%	111
0.063 - 0.095	56%	86
0.095 - 0.225	56%	378
0.225 - 0.405	64%	465
0.405 - 0.631	65%	429
0.631 - 0.925	76%	402
0.925 - 1.391	82%	385
1.391 - 2.250	88%	373
2.250 - inf	95%	290

(b) Distribution of low energy solution bias in quantiles of ν for the subleading τ for 100 seeds and 10^8 MH iterations.

Distribution of Low Energy Bias in quantiles of ν

range of ν	Low Solution Bias	Number of Events
0.000 - 0.294	70%	508
0.294 - 0.469	78%	521
0.469 - 0.637	80%	460
0.637 - 0.812	84%	405
0.812 - 1.007	90%	378
1.007 - 1.239	90%	309
1.239 - 1.559	93%	256
1.559 - 2.088	95%	187
2.088 - 3.080	98%	61
3.080 - inf	100%	17

(a) Distribution of low energy solution bias in quantiles of ν for the leading τ .

Distribution of Low Energy Bias in quantiles of ν

range of ν	Low Solution Bias	Number of Events
0.000 - 0.031	71%	135
0.031 - 0.063	61%	90
0.063 - 0.095	47%	108
0.095 - 0.225	59%	383
0.225 - 0.404	63%	450
0.404 - 0.628	70%	411
0.628 - 0.927	75%	410
0.927 - 1.390	77%	395
1.390 - 2.250	90%	378
2.250 - inf	94%	94

(b) Distribution of low energy solution bias in quantiles of ν for the subleading τ .

List of Figures

2.1	Graphical representation of the Standard Model	4
2.2	Plot of the QED coupling constant over a range of momentum transfers	5
2.3	Bhabha Scattering	6
2.4	plot of the QCD coupling over a range of momentum transfer	8
2.5	Hadronisation	8
2.6	Higgs Potential	10
2.7	Higgs Potential	11
2.8	Higgs Potential	12
2.9	Higgs Branching Ratios	12
2.10	Lepton Decay	14
3.1	Tau Jet	18
3.2	Production Cross Sections	18
3.3	ATLAS Detector	19
3.4	ATLAS Inner Detector	21
3.5	ATLAS Calorimeter	21
3.6	ATLAS Muon Detector	23
3.7	Tau Jet	26
3.8	Decay Mode Efficiency Matrix	27
3.9	τ track selection efficiency	28
3.10	f_{JVF}	28
4.1	MCMC modeling	32
5.1	3p0n Selection	38
5.2	Primary Vertex Track Multiplicity	38
5.4	Decay distance in the Lab frame.	40
5.7	Number of Useable Solutions	43
5.10	Momentum Matching	45
5.11	Number of Useable Solutions after cuts	46
5.13	Metropolis Hastings Flow Chart	48
5.15	Higgs and Z boson mass estimates from the τ reconstruction after truth weighted PDFs	53
6.12	Higgs and Z boson mass estimates from the τ reconstruction in the initial MMC	69
6.13	Higgs and Z boson mass estimates from the τ reconstruction after truth weighted PDFs	69
6.14	Higgs and Z boson mass estimates from the τ reconstruction after parametrisation.	70

List of Tables

6.1	Distribution of low energy solution bias in quantiles of ν for the leading τ	65
6.2	Distribution of low energy solution bias in quantiles of ν for the subleading τ	67